

AD-A194 768

THE ACOUSTIC FIELD SCATTERED FROM SOME APPROXIMATE  
PRESSURE RELEASE MATERIALS COATING A FINITE CYLINDER

A THESIS

Presented to

The Faculty of the George W. Woodruff

School of Mechanical Engineering

Georgia Institute of Technology

by

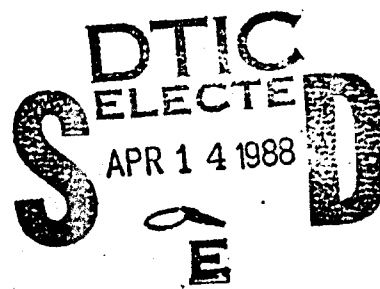
Gary W. Caille

In Partial Fulfillment

of the Requirements for the Degree

Doctor of Philosophy

March 1988



This document has been approved  
for public release and sale; the  
distribution is unlimited.

88 4 13 037

THE ACOUSTIC FIELD SCATTERED FROM SOME APPROXIMATE  
PRESSURE RELEASE MATERIALS COATING A FINITE CYLINDER

A THESIS

Presented to

The Faculty of the George W. Woodruff

School of Mechanical Engineering

Georgia Institute of Technology

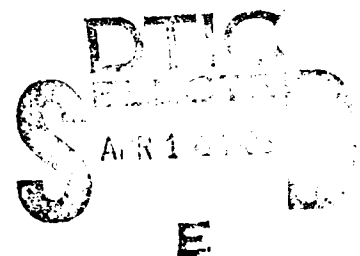
*N00228-85-B-3247*

by

Gary W. Caille

In Partial Fulfillment  
of the Requirements for the Degree  
Doctor of Philosophy

March 1988



### DEDICATION

*This thesis is dedicated to my wife, Susan, my daughter, Stephanie, and my son, Kevin.*

Accession For	
NTIS	<input checked="" type="checkbox"/>
DTIC TAB	<input type="checkbox"/>
Unannounced	<input type="checkbox"/>
Justification	<input type="checkbox"/>
By	
Dist	
Avail	
Dist	
A-1	



## ACKNOWLEDGMENTS

The author wishes to sincerely thank his advisor, Dr. Peter H. Rogers, and Dr. Jacek Jarzynski for their enthusiastic support, patient guidance, technical assistance and most importantly, their friendship, throughout the course of this research project. Thanks are also extended to other members of the thesis advisory committee: Drs. George M. Rentzepis, Warren C. Strahle, and Winston K. Pendleton for their constructive criticisms and helpful suggestions which strengthened this work.

The author would like to express his appreciation to the United States Navy for allowing him to pursue this work and to Dr. Raymond M. Fitzgerald, Ocean Acoustics Program Manager for the Office of Naval Research, for support provided under program 1125OA.

The author is especially indebted to his wife, Susan, for the support she has given and the sacrifices she has made to allow him to pursue this research. The author also wishes to thank his mother, father, sister and his wife's mother for their encouragement and support during this project.

## TABLE OF CONTENTS

DEDICATION	ii
ACKNOWLEDGEMENTS	iii
TABLE OF CONTENTS	iv
LIST OF TABLES	vii
LIST OF FIGURES	viii
LIST OF SYMBOLS	xii
SUMMARY	xiv
CHAPTER I: Introduction	1
Background Review	4
Scattering From the Infinite Cylinder and Cylindrical Shell	4
Numerical Methods	19
Determination of Dynamic Viscoelastic Moduli	33
CHAPTER II: Experimental Procedures	40
Determination of Material Viscoelastic Constants	40
Complex Young's Modulus	41
Plane Wave Modulus Determination	46

Scattering Experiments	51
Infinite Cylinder Experiment	51
Finite Cylinder Experiment	54
CHAPTER III: Experimental Results and Discussion	59
Viscoelastic Moduli Determination	59
Scattering From the Simulated Infinite Cylinder	82
Finite Shell with End On Incident Signal	99
Finite Shell with Normal (Side) Incident Signal	106
CHAPTER IV: Conclusions and Recommendations	116
APPENDIX A: Derivation of the Scattered Field and Surface	
Velocity From an Infinite Pressure Release Cylinder	
for an Incident Plane Wave	121
Determination of the Low Frequency Limit	130
Determination of the High Frequency Limit or	
Specular Reflection	131
APPENDIX B: Pressure Release Sphere	134
APPENDIX C: Modification of the Naval Ocean Systems Center	
(NOSC) CHIEF Program	139
APPENDIX D: Scattering From the Coated Infinite Cylinder	152
Scattering From an Infinite Elastic Cylinder	
With Arbitrary Incidence	152

Scattering From the Two Layer Cylinder With	
Normal Incidence	162
Elastic Shell Derivation	172
APPENDIX E: The Treatment of Multiple Reflections	
in the Panel for Plane Wave Modulus Experiment	177
BIBLIOGRAPHY	183
VITA	193

**LIST OF TABLES**

Table 3-1 Density of Materials	60
Table C-1 Comparison of CHIEF Results for Pressure Release Sphere	146
Table C-2 Comparison of CHIEF Program With SHIP Program	149



**LIST OF FIGURES**

Figure 1-1 Circumferential Wave Illustration	8
Figure 1-2 General Scattering Geometry for Numerical Methods	20
Figure 2-1 Experimental Apparatus for Young's Modulus Measurement	42
Figure 2-2 Experimental Apparatus for Plane Wave Modulus Measurement	47
Figure 2-3 F-33 Beam Spreading at 15 kHz for Panel Measurement	49
Figure 2-4 Experimental Setup for Infinite Shell Measurements	52
Figure 2-5 Finite Cylinder Experimental Setup for Axial Incidence	56
Figure 2-6 Finite Cylinder Experimental Setup for Normal Incidence	57
Figure 3-1 Neoprene Extensional Speed versus Frequency	62
Figure 3-2 Neoprene Extensional Attenuation versus Frequency	63
Figure 3-3 Neoprene Plane Wave Speed versus Frequency	64
Figure 3-4 Neoprene Plane Wave Attenuation versus Frequency	65
Figure 3-5 Nitrile Extensional Speed versus Frequency	66
Figure 3-6 Nitrile Extensional Attenuation versus Frequency	67
Figure 3-7 Nitrile Plane Wave Speed versus Frequency	68
Figure 3-8 Nitrile Plane Wave Attenuation versus Frequency	69
Figure 3-9 Corprene Extensional Speed versus Frequency	71
Figure 3-10 Corprene Extensional Attenuation versus Frequency	72

Figure 3-11 Corprene Plane Wave Speed versus Frequency	73
Figure 3-12 Corprene Plane Wave Attenuation versus Frequency	74
Figure 3-13 Cork-Nitrile Extensional Speed versus Frequency	77
Figure 3-14 Cork-Nitrile Extensional Attenuation versus Frequency	78
Figure 3-15 Cork-Nitrile Plane Wave Speed versus Frequency	79
Figure 3-16 Cork-Nitrile Plane Wave Attenuation versus Frequency	80
Figure 3-17 Uncoated Thin Shell Backscatter Form Function ( $b/a = .97$ )	83
Figure 3-18 1/16" Corprene Coated Thin Shell Backscatter Form Function ( $b/a = .97$ ) (Solid Line - Theory, Dots - Experimental Data)	86
Figure 3-19 1/16" Corprene Coated Thin Shell Theoretical Backscatter Form Function( $b/a = .97$ ) (Solid Line - Poisson's Ratio = 0., Dashes - Poisson's Ratio = .4)	87
Figure 3-20 5/16" Corprene Coated Thin Shell Backscatter Form Function( $b/a = .97$ ) (Solid Line - Theory, Dots - Experimental Data)	89
Figure 3-21 Theoretical Backscatter Form Function for Four Thicknesses of Corprene	91
Figure 3-22 1/4" Nitrile Coated Thin Shell Backscatter Form Function ( $b/a = .97$ ) (Solid Line - Theory, Dots - Experimental Data)	93
Figure 3-23 Theoretical Backscatter Form Function for Two Thicknesses of Nitrile and Pressure Release Cylinder	95
Figure 3-24 Uncoated Thin Shell Backscatter Waveform (40kHz Center Frequency)	96
Figure 3-25 Nitrile Coated Thin Shell Backscatter Waveform (40kHz Center Frequency)	97

Figure 3-26 Theoretical Backscatter Form Function for 0.25 inches of Nitrile Coating on Thin Shell and Pressure Release Cylinder	98
Figure 3-27 Scattered Signal from Uncoated Thick Finite Shell ( $b/a = .9$ ) for Axial Incidence (60 kHz Center Frequency)	100
Figure 3-28 Scattered Signal from Thick Finite Shell ( $b/a = .9$ ) Coated with 0.25 inches of Neoprene for Axial Incidence (60 kHz Center Frequency)	101
Figure 3-29 Normalized Scattered Pressure Versus $ka$ for Thick Finite Shell ( $b/a = .9$ ) with Axial Incidence (Solid Line is Shell Coated with 0.25 inches of Neoprene, Dotted Line is Uncoated Shell)	102
Figure 3-30 Scattered Signal from Uncoated Thick Finite Shell ( $b/a = .9$ ) for Axial Incidence (45 kHz Center Frequency)	104
Figure 3-31 Normalized Scattered Pressure Versus $ka$ for Thick Finite Shell ( $b/a = .9$ ) with Axial Incidence and SHIP Output for Pressure Release Finite Cylinder (Solid Line is Shell Coated with 0.25 inches of Neoprene, Dashed Line is SHIP)	105
Figure 3-32 Scattered Signal from Uncoated Thick Finite Shell ( $b/a = .9$ ) for Normal Incidence (40 kHz Center Frequency)	107
Figure 3-33 Scattered Signal from Thick Finite Shell ( $b/a = .9$ ) Coated with 0.25 inches of Neoprene for Normal Incidence (40 kHz Center Frequency)	108
Figure 3-34 Scattered Signal from Uncoated Thick Finite Shell ( $b/a = .9$ ) for Normal Incidence (20 kHz Center Frequency)	110
Figure 3-35 Scattered Signal from Thick Finite Shell ( $b/a = .9$ ) Coated with 0.25 inches of Neoprene for Normal Incidence (20 kHz Center Frequency)	112

Figure 3-36 Normalized Scattered Pressure Versus $ka$ for Thick Finite Shell ( $b/a = .9$ ) with Normal Incidence (Solid Line is Shell Coated with 0.25 inches of Neoprene, Dotted Line is Uncoated Shell)	113
Figure 3-37 Normalized Scattered Pressure Versus $ka$ for Thick Finite Shell ( $b/a = .9$ ) with Normal Incidence and CHIEF Output for Pressure Release Finite Cylinder (Solid Line is Shell Coated with 0.25 inches of Neoprene, Dashed Line is CHIEF)	114
Figure A-1 Geometry for Infinite Pressure Release Cylinder	122
Figure A-2 Geometry for Infinite Pressure Release Cylinder With Normal Incidence	133
Figure B-1 Geometry for Pressure Release Sphere	135
Figure C-1 Scattering Geometry and Subdivision Scheme for Pressure Release Sphere	145
Figure C-2 Scattering Geometry and Subdivision Scheme for Pressure Release Finite Cylinder	148
Figure D-1 Scattering Geometry for Infinite Cylindrical Shell	153
Figure D-2 Scattering Geometry for the Layered Cylindrical Shell	163
Figure E-1 Multiple Internal Reflection in a One-Dimensional Panel	178

## LIST OF SYMBOLS

$a$	radius of scatterer
$\alpha$	attenuation
B&K	BrueI and Kjaer
$c, c_w$	wave propagation speed in fluid (water)
$C_p^F$	Franz wave speed
$C_R$	Rayleigh wave speed
$C_L, C_d$	longitudinal or dilatational wave speed
$C_T, C_s$	transverse or shear wave speed
CHIEF	Combine Helmholtz Integral Equation Formulation
$E$	complex Young's modulus
$f$	frequency
$f_\infty$	form function
FFT	Fast Fourier Transform
$g(x,y)$	free space Green's function
$G, \mu$	complex shear modulus
$h$	wall thickness of shell
$k$	wave number
$ka$	nondimensional wave number

$k_s$	shear wave number
$k_d$	longitudinal or dilatational wave number
$\lambda$	first Lamé constant
$M$	plane wave modulus
$\nu$	Poisson's ratio
$\omega$	circular frequency
$P, p$	pressure
$P_m(x)$	Legendre polynomial of order $m$
$\phi$	phase, spherical coordinate
$\rho$	material density
SHIP	Simplified Helmholtz Integral Program
$t$	time
$U$	displacement vector
USRD	Underwater Sound Reference Detachment
$V$	velocity

## SUMMARY

The objective was to determine if a pressure release boundary condition can be achieved by coating an elastic shell with a visco-elastic material. One necessary condition is that the coating must acoustically decouple the shell from the scattering problem. Two closed cell rubbers and two cork-rubber composites (nitrile and neoprene based) were investigated. The dynamic viscoelastic constants of the materials were determined by wave propagation techniques. The far field scattering form functions for an infinite cylindrical shell coated with the viscoelastic material were calculated using the complete elastic equations of motion. The form functions were experimentally measured for the different materials at different thicknesses as verification of the theory. A thick finite right cylindrical shell was coated with .25 inches of closed cell neoprene and the normalized scattered pressure measured. The pressure release normalized scattered pressure was determined for the end on incident plane wave case using the acoustic radiation Simplified Helmholtz Integral Program (SHIP). The pressure release normalized scattered pressure was determined for the side incident case using a modified Combined Helmholtz Integral Equation Formulation (CHIEF) radiation program.

The material property measurements showed the closed cell rubbers have longitudinal wave propagation speeds of approximately 150 m/sec and attenuations of 30 dB/cm. The cork-rubber composites have longitudinal wave speeds of approximately 300 m/sec and attenuations of 7 dB/cm.

The scattering measurements demonstrated that a thin shell (inner radius to outer radius ratio of .97) could be made to scatter in a pressure release manner with a .25 inches of nitrile. The rubber-cork composites could not produce the pressure release effect for nondimensionalized wave number (product of the wave number and the radius of the cylinder) values less than 4 with reasonable thicknesses. The coated finite thick shell, with side incidence, scattered within 1 dB of the pressure release theory and completely eliminated the first antisymmetric Lamb mode circumferential wave. For the end on case, the coating significantly reduced the resonance effects and eliminated the scattered signal from the back end of the shell.



## CHAPTER I

### Introduction

Acoustic scattering from objects has been studied extensively since the days of Lord Rayleigh. The most recent advances, which involve extensions of the basic theory to more arbitrary shapes and mixed boundary conditions, can be directly attributed to improved numerical techniques and the digital computer. There are two fundamental, degenerate boundary conditions which may occur on the surface of the scatterer. The first is the rigid surface or Neumann boundary condition where the normal acoustic velocity of the surface is zero (i.e. the density and sound speed of the scatterer  $\rightarrow \infty$ ). The second is the pressure release surface or Dirichlet boundary condition where the acoustic pressure is zero on the surface (i.e. the density and sound speed of the scatterer  $\rightarrow 0$ ). Reductions to these two degenerate conditions are traditionally made when the specific acoustic impedance of the scatterer is significantly greater than (for the rigid case) or less than (for the pressure release case) the specific acoustic impedance of the surrounding medium.

The rigid body case (Neumann condition) and the pressure release case (Dirichlet condition) have been extensively researched analytically for simple shapes<sup>1</sup>. The rigid body has also been the subject of extensive experimental inves-

tigation. Since a perfectly rigid body does not really exist, this condition may be considered a limiting form of the more precise problem of scattering from elastic objects where the degree of elasticity is specified or to be determined. Elastic body scattering is a current major research area and the review papers by Uberall<sup>2,3</sup> and Nigul<sup>4</sup> contain nearly one hundred references on this subject.

The pressure release surface (Dirichlet condition) has not received the experimental attention of the rigid body case for two reasons:

1. This condition is not observed in air.
2. Until recently materials such as closed-cell rubbers and corprene which approximate a pressure release surface in water have not been commercially available.

The use of the closed-cell rubber as a decoupling material has provided a practical application. Since the pressure release material is not structurally suitable as the scattering body itself, it will be considered as a surface coating. The rigorous theoretical approach to the coated scatterer is to apply the exact elasticity equations to the structural material (with or without absorption) and to apply the exact viscoelastic equations to the coating. The scattering problem is then solved as a boundary value problem. If the coating were truly a pressure release material, the elastic behavior of the structure could be neglected. This decoupling of the underlying elastic structure from the fluid allows the scattered field to be determined by treating the body as an impedance surface (using only the boundary conditions at the exterior surface) and solving the exterior field problem using well

documented techniques.

This thesis investigates the pressure release surface condition in detail. The procedure to be followed is that suggested by Neubauer<sup>5</sup>. The backscattered pressure field for a pressure release, finite cylinder is determined using the modified Naval Ocean Systems Center (NOSC) CHIEF program for side incidence (or normal incidence) at low frequency and the Naval Research Laboratory (NRL) SHIP program for end on (axial) incidence. The backscattered pressure of a coated finite cylinder is measured and compared with the theoretical pressure release results. The theoretical prediction of the backscattered pressure for an infinite coated cylinder using the experimentally determined material constants is used for comparison with measurements on experimental models. Finite cylinder data has compared well with infinite cylinder calculations when long cylinder are used and the ends are either outside the main lobe of a piston type projector or the length of the cylinder is greater than the length of the first Fresnel zone, i.e. farfield of the cylinder, using a point source<sup>6</sup>. The overall objective is to determine to what extent the pressure release condition can be approached, (i.e. for what frequency range and for what thickness of coating material), with some commercially available materials. Finally, the significant question of when the scattering field can be determined treating the surface as a simple pressure release boundary or

the more complex elastic-viscoelastic solution must be use in order to achieve the required accuracy is answered.

### Background Review

#### Scattering From the Infinite Cylinder and Cylindrical Shell

The first solutions to plane wave scattering by an infinite cylinder were developed by Lord Rayleigh<sup>7</sup>. He considered both rigid, immovable and nonrigid cylinders with diameters small compared to the acoustic wavelength in the fluid ( $ka < 1$  where  $k = \omega/c$ ,  $a$  is the radius of the cylinder,  $\omega$  is the angular frequency, and  $c$  is the speed of sound in the fluid). Rayleigh also outlined a method of solution for larger diameter cylinders and spheres using an infinite series of cylindrical and spherical harmonics, respectively, which has become known as the Rayleigh series. The solution method using the Rayleigh series is called the normal mode solution method. Morse<sup>8</sup> demonstrates the normal mode solution method for  $ka$  values up to 2.5. In 1951 Faran<sup>9</sup> published a classical paper on the exact solutions to scattering of plane waves from an infinite, homogeneous, isotropic cylinder capable of supporting both shear and compressional waves. His method of solution was to solve the elastic equations of motion developed by Love<sup>10</sup>. The three dimensional equation of motion in vector form is

$$(\lambda + 2\mu)\nabla(\nabla \cdot \mathbf{U}) - \mu\nabla \times (\nabla \times \mathbf{U}) = \rho_1 \frac{\partial^2 \mathbf{U}}{\partial t^2} \quad (1-1)$$

where  $\mathbf{U}$  is the displacement,  $\lambda$  and  $\mu$  are Lamé constants ( $\mu$  is the shear modulus and  $\lambda + 2\mu$  is the plane wave or longitudinal modulus) and  $t$  is the time. Using the Helmholtz theorem the displacement is written as the sum of a vector potential and a scalar potential.

$$\mathbf{U} = -\nabla\psi + \nabla \times \mathbf{A} \quad (1-2)$$

Faran experimentally showed that the rigid, immovable cylinder was a valid approximation provided: 1. the frequency was less than that of the first normal mode of free vibration of the cylinder and 2. the density of the scatterer is significantly greater than the density of the surrounding fluid. As the density difference between the scatterer and the fluid becomes smaller, the rigid, immovable approximation should be replaced by the rigid but movable case, and eventually by the totally elastic case as the density difference decreases further. He was also the first to experimentally observe resonances or large amplitude changes in the scattered field when the incident frequency approaches the characteristic frequencies of the scatterer.

Normal mode calculations were soon applied to higher  $ka$  values with excellent experimental confirmation for elastic spheres and spherical shells<sup>11-16</sup>. Hickling<sup>11</sup> was the first to utilize the digital computer for  $ka$  values less than 20

and found convergence of the harmonic series to be extremely slow as  $ka$  increased. He also formulated the result in terms of a far field form function,  $f_{\infty}$ , which normalizes the scattered pressure,  $P_s(\theta)$ , to the incident pressure,  $P_0$ , radius of the scatterer,  $a$ , and the distance to the field point from the acoustical center of the scatterer,  $R$  in such a manner so as to be equal to 1.0 for the rigid body case. The cylindrical far field form function is

$$f_{\infty} = \sqrt{\frac{2R}{a}} \frac{P_s(\theta)}{P_0} \quad (1-2)$$

Neubauer et al.<sup>15</sup> demonstrated the first quantitative agreement between normal mode theory and experimental results for solid elastic spheres. Dragonette et al.<sup>16</sup> demonstrated that good quantitative results could be obtained using short broadband pulses and analyzing the frequency content of the scattered signal. Experimental verification of the normal mode solution method for the infinite cylinder (using a finite cylinder) was obtained by Dardy et al.<sup>17</sup>.

Due to differences in the scattered fields, it is necessary to differentiate between scattering from cylindrical shells and scattering from solid cylinders. Barnard<sup>18</sup> observed numerous periodic echoes for an incident pulse on solid and hollow brass cylinder which suggests additional wave contributions besides the purely specular reflection. The hollow cylinder (shell) was also observed to scatter differently than the solid cylinder. Subsequent authors<sup>19,20,21</sup> proposed the exis-

tence of two types of circumferential waves for the solid cylinder. The two types of waves are: 1. Franz waves which are analogous to the geometrically diffracted circumferential waves discovered by Franz<sup>22</sup> while investigating diffraction of electromagnetic waves by perfectly conducting spheres and cylinders. 2. Rayleigh type (or R type) waves which are surface waves which depend on the elastic properties of the scatterer. Neubauer<sup>23</sup> gives an excellent review of the literature and theory of circumferential waves which is briefly summarized below.

The two wave types generated by the solid cylinder resulted from the observation that one wave, the Franz wave or geometrical wave, had a wave speed below the propagation speed of the fluid and the other wave, Rayleigh type waves, had a wave speed significantly above the sound speed of the fluid medium. Neubauer<sup>24</sup> and Harbolt and Steinberg<sup>25</sup> experimentally verified the presence of the geometrical or Franz waves. Theoretical evidence for the Rayleigh type waves was developed by Grace and Goodman<sup>26</sup> with experimental verification by Bunney et al.<sup>27</sup> and Neubauer<sup>28</sup>. Figure 1-1 illustrates the the specular reflection (backscattered) contacting the cylinder at point A and returning. Also illustrated are two Franz waves originating at points B and C and traveling in the fluid around the back of the cylinder. The Rayleigh type waves travel paths similar to the Franz waves but exist in the solid cylinder not in the fluid.

Although the normal mode solution method leads to the correct scattered pressure verses frequency result, the series converges very slowly and becomes computationally impractical for  $ka$  values greater than 20. Another drawback of

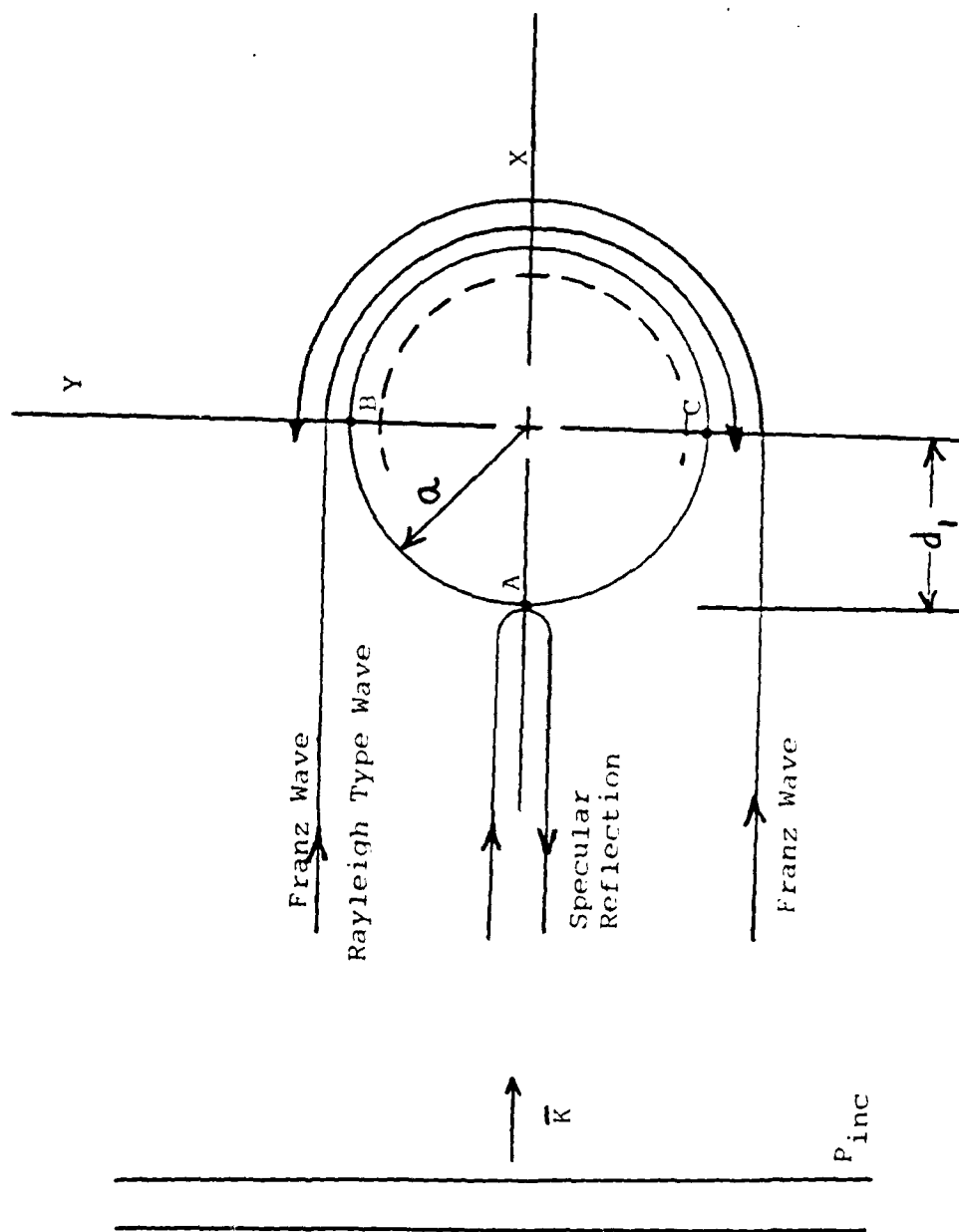


Figure 1-1 Circumferential Wave Illustration



this method is that it does not easily isolate the individual mechanisms, i.e. the specular and circumferential waves, contributing to the scattered pressure field. Uberall et al.<sup>29</sup> has demonstrated the relationship between circumferential or creeping waves and the normal modes, but unfortunately the relationship is not straight forward. The current method to extract the individual wave type contributions is the Sommerfeld-Watson transformation of the normal mode series. This transform maps the normal mode series into the complex plane in the form of a contour integral. Two groups of poles are observed which yield the two types of circumferential waves. The Sommerfeld-Watson transformation has been extensively used. It converges rapidly and its results agree well with experiment<sup>30,31,32</sup>.

Some insight into the two types of creeping waves may be garnered from consideration of wave propagation along an infinite plane interface between two different isotropic media. (Uberall<sup>2</sup> contains an indepth review of circumferential wave.) If one of the media is a vacuum and the other an elastic solid, Rayleigh<sup>33</sup> showed that an inhomogeneous surface wave results which exponentially decays normal to the surface and propagates along the surface. This wave, the classical Rayleigh wave, is a combination compressive-shear type wave which propagates with a unique velocity,  $C_R$ , along the surface. The Rayleigh wave speed varies from 0.86 to 0.96 of the shear wave speed in the elastic media as Poisson's ratio varies from 0 to .5. No waves exist in the vacuum. Love<sup>34</sup> and Stoneley<sup>35</sup> extended the analysis to liquid-solid and solid-solid interfaces. The surface waves

generated in these situations are often called generalized Rayleigh waves. Generalized Rayleigh waves differ from the ideal Rayleigh wave in that the generalized Rayleigh wave exist in both media and are exponentially damped in the direction of propagation (nonpropagating waves). The generalized Rayleigh wave also decays exponentially in the normal direction from the surface in both media. The existence of the wave in the second media results from the seepage of energy from the first media which causes the wave to be nonpropagating along the surface. (The seepage of energy has resulted in the generalized Rayleigh wave being referred to as the Leaky Rayleigh wave.) In addition for the generalized Rayleigh waves, new modes of the surface wave exist. The dispersion equation is

$$4 \left( \frac{C_T}{C} \right) \left[ 1 - \frac{C_T^2}{C^2} \right]^{\frac{1}{2}} \left[ \frac{C_T^2}{C_L^2} - \frac{C_T^2}{C^2} \right]^{\frac{1}{2}} + \left[ 1 - 2 \frac{C_T^2}{C^2} \right]^2 =$$

$$- \frac{\rho_F}{\rho_S} \left( \frac{\frac{1}{C_L^2} - \frac{1}{C^2}}{\frac{1}{C_F^2} - \frac{1}{C^2}} \right) \quad (1-4)$$

where  $C_L$  is the longitudinal wave speed,  $C_T$  is the transverse wave speed and  $\rho_S$  is the density of the elastic solid,  $C_F$  is the propagation speed and  $\rho_F$  is the density of the liquid (fluid) and  $C$  is the generalized Rayleigh wave speed to be determined. Equation (1-4) has one real root and the remaining roots are complex. As  $\rho_F \rightarrow 0$ ,

there is one complex root whose real part approaches the Rayleigh wave speed,  $C_R$ . (The fact that the roots are complex implies that the wave is attenuating in the propagation direction.) The real root indicates a propagating surface wave which travels mainly in the liquid. The wave is still attenuating normal to the surface. The phase speed of the propagating surface wave is less than the propagation speed of the liquid (see Viktorov<sup>36</sup> for detailed derivation of the roots of equation (1-4)). This wave is generally referred to as the Stoneley wave. Uberall, et al.<sup>30</sup> demonstrates the Watson-Sommerfield transform for the pressure release cylinder in a fluid. The transform yields poles which correspond to the propagation phase speeds less than the propagation speed of the fluid. These poles represent the different modes of the geometric or Franz waves. Uberall, et al. also shows that the first Franz wave for the pressure release cylinder is significantly more attenuated than the corresponding first Franz wave of the rigid cylinder. This attenuation explains why the pressure release backscatter form function does not show the classical form function structure associated with the infinite rigid cylinder. The analogy is that the superposition of the Franz modes result in the unique flat plate Stoneley wave. The attenuation of the Franz wave is a curvature effect caused by the tangential radiation of energy into the fluid for each mode. Neubauer<sup>23</sup> demonstrates the Watson-Sommerfield transform for a solid aluminum cylinder. The transform produces two sets of poles referred to as Franz type and R type (Rayleigh type) poles. The R type poles result in dispersive wave propagating at phase speeds greater than the propagation speed of the fluid. Frisk

and Uberall<sup>37</sup> related the first R type pole,  $R_1$ , to the generalized Rayleigh wave since its phase speed approaches the Rayleigh wave speed,  $C_R$ , as  $ka \rightarrow \infty$ . The other R type poles are called "whispering gallery" waves and become lateral waves as  $ka \rightarrow \infty$ .

As stated above, the R-type waves are not present for the pressure release and rigid cases. When an incident pulse is used, Neubauer<sup>23</sup> shows the Franz wave and the specular reflection can be time separated with

$$\Delta t = \frac{2a}{C_w} + \frac{\pi a}{C_p^F} \quad (1-5)$$

where  $C_p^F$  is the phase speed of the Franz wave and  $C_w$  is the propagation speed of the water. As illustrated in figure 1-1, the first term of equation (1-5) corresponds to time to travel twice the distance  $d_1$  in the fluid and the second term of equation (1-5) is the time to travel half of the circumference of the cylinder at the phase speed of the Franz wave. Due to attenuation, only the first Franz wave is of significance (see Neubauer<sup>24</sup>). It is also possible to recover the Franz wave by decomposing the scattered pulse into a specular reflection and a creeping wave using the assumption that the specular reflection has the same frequency content as the incident pulse. This technique is illustrated by Rudgers<sup>38</sup> for a rigid sphere.

Another possible contributor to the scattered field is multiple internal reflections of the shear wave. Neubauer and Dragonette<sup>39</sup> demonstrated the significance of these multiple reflections. Brill and Uberall<sup>40</sup> also provided

theoretical support for the shear wave reflections.

In order to understand the scattered field of the cylindrical shell, the relation between the circumferential waves in the shell and the scattering form function must be developed. From the form function versus  $ka$  graph for the cylindrical shell, three well defined background regions are apparent. In region 1 or soft background region (small  $ka$  values), the specular reflection is inverted relative to the incident signal and the resonances appear as dips (decreases) in the form function on the form function versus  $ka$  graph. The second region or transition region occurs when the resonances appear as both dips and peaks on the form function versus  $ka$  graph. In the third or rigid background region, the specular reflection is in phase with the incident signal and the resonances appear as peaks on the form function versus  $ka$  graph. For the shell, Neubauer<sup>23</sup> states that the Franz waves do not measurably affect the form function. The R type waves are not present since they require a semi-infinite medium (e.g. the thickness of the shell is usually less than a wavelength and can not support the R type waves). Horton, et al.<sup>41</sup> made the first attempt to relate motion of the shell to plate theory. Diercks, et al.<sup>19</sup>, established the existence of two groups of circumferential waves in shells with different group velocities. They were referred to as longitudinal and flexural waves where the group speed of the longitudinal waves is greater than the group speed of the flexural waves. Some confusion existed due to the variation in speeds that were obtained for the fast (longitudinal) circumferential waves. Herrmann and Mirsky<sup>42</sup> determined that shell analysis can be divided into two methods. For

very thin shells, the motion is dominated by membrane and curvature effect, therefore membrane theory is used. For thicker shells, the motion is dominated by flexural, rotatory inertia, and shear-deformation effects, therefore plate theories are used. For wavelengths less than  $\Lambda_t$ , the membrane theory is used.

$$\Lambda_t^2 = R h \frac{2\pi^2}{\sqrt{3(1 - \nu^2)^2}} \quad (1-6)$$

where  $R$  is the mean radius,  $h$  is the shell thickness and  $\nu$  is poisson's ratio. For the experiments to be conducted in this investigation, the shell is of sufficient thickness to require plate theories. The two circumferential groups of waves observed by Diercks, et al.<sup>19</sup> correspond to symmetric Lamb modes (longitudinal) and antisymmetric Lamb modes for infinite plates (where symmetry is defined relative to the axis located in the center of the plate, parallel to the surface). In order for either of the modes to be excited, the phase speed of the mode must be greater than the propagation speed of the fluid (water). The angle at which the mode is excited is determined from

$$\sin(\theta_i) = \frac{c_{\text{water}}}{v_p} \quad \text{where } v_p \text{ is the phase speed of the mode.}$$

It is possible to generate the first symmetric mode for all frequency thickness ( $fh =$  shell thickness  $\times$  frequency) values in water. For a complete analysis, including dispersion curves, of mode generation in steel (ratio of longitudinal to shear speeds

equal to 1.8), see Grigsby and Tajchman<sup>43</sup>. Viktorov<sup>36</sup> shows the first symmetric Lamb mode phase,  $V_{s,p}$ , and group,  $V_{s,g}$ , speeds vary from

$$V_{s(p.g)} = \sqrt{\frac{E}{\rho(1 - \nu^2)}} \quad (1-7)$$

to the Rayleigh wave speed,  $C_R$ , as  $fh$  varies from 0 to  $\infty$ . The first antisymmetric mode phase speed,  $V_{a,p}$ , varies as

$$V_{a,p} = \sqrt[4]{\frac{E}{3\rho(1 - \nu^2)}} \sqrt{\frac{\omega h}{2}} \quad (1-8)$$

(approaches 0 as  $fh \rightarrow \infty$ ) and approaches the Rayleigh wave speed,  $C_R$ , as  $fh \rightarrow \infty$ . The first antisymmetric mode group speed is equal to twice  $V_{a,p}$  and also approaches the Rayleigh wave speed,  $C_R$ , as  $fh \rightarrow \infty$ . As the frequency thickness increases, additional modes of the symmetric and antisymmetric Lamb waves become excited. The cutoff frequencies of the symmetric modes are given by the plate thickness corresponding to one half wavelength intervals of the longitudinal wave and whole wavelength intervals of the transverse wave. The cutoff frequencies of the antisymmetric modes are given by the plate thickness corresponding to one half wavelength intervals of the transverse wave and whole wavelength intervals of the longitudinal wave. The higher modes approach the transverse wave speed of the material as the frequency thickness tends to infinity. Viktorov<sup>36</sup> states the

asymptotic forms of the phase speed for the symmetric and antisymmetric modes of order  $n$  as

$$v_{s,p} = c_T \left( 1 + \frac{2 \pi^2 n^2}{D^2} \right) \quad (1-9)$$

$$v_{a,p} = c_T \left( 1 + \frac{(2n - 1)^2 \pi^2}{8D^2} \right)$$

where  $D = (\omega h)/(2c_T)$ .

The significant observations (discussed in Neubauer<sup>23</sup>) from the plate theory predictions are:

1. for thin shells, the first symmetric Lamb mode dominates in the low  $ka$  region and will cause significant dips in the form function verses  $ka$  graph at intervals of  $\Delta ka = 3.7$ . These dips result from the addition of the specular reflection, which is 180 degrees out of phase from the incident signal, and the first symmetric mode circumferential wave (at the frequency where the wavelength of the circumferential wave corresponds to an integer multiple of the circumference of the cylinder), which is in phase with the incident signal, producing a cancelling effect in the overall scattered signal. As the shell thickness increases, the dips become less pronounced and additional symmetric modes may become excited. The excitation of additional modes explains the early confusion in the literature involving the phase speed of the fast circumferential waves.



2. the first antisymmetric mode is usually not excited in thin shells until larger  $ka$  values (for aluminum and an inner to outer radius ratio of .98, the first antisymmetric mode is not excited until a  $ka$  of approximately 55). As the shell thickness increases, the frequency required for excitation of the first antisymmetric mode decreases (same  $fh$  value). (Neubauer shows that for an aluminum shell with an inner to outer radius of .9, the antisymmetric mode is observed at a  $ka = 10$ .) The antisymmetric mode circumferential waves cause resonance peaks in the form function versus  $ka$  graph. The peaks occur because the shell is scattering in a rigid manner since the specular reflection is in phase with the incident signal and the antisymmetric wave, which is an elastic wave, is also in phase with the incident signal. When the wavelength of the antisymmetric mode is the correct value to allow exact phase matching, the antisymmetric mode circumferential wave and the specular reflection add to cause a resonance peak.

An alternate method of determining the scattered field is to assume a series solution in form of inverse integer powers of  $ka$ . This method, called the Luneberg-Kline method<sup>44</sup>, is adapted from optical theory. The scattered pressure is

$$p_s(r) = \exp(ik\psi) \sum_{n=0}^{\infty} \frac{v_n(r)}{(k^2 - k_0^2)^n} \quad (1-10)$$

Since only integer powers are considered, the circumferential waves are neglected.

Due to the difficulty in determining  $V_n(r)$ , only the first two terms are retained, i.e.  $n=2$ . Keller et al.<sup>45</sup> applies this method to the pressure release, rigid and impedance boundary conditions. George and Uberall<sup>46</sup> compare the Luneberg-Kline method with the Kirchhoff method for complex impedance surfaces and concluded that the Luneberg-Kline method gives a more accurate measure of the scattered field.

In the previous references with the exception of the approximate methods, absorption by the scatterer has been neglected. Schuetz and Neubauer<sup>47</sup> demonstrated that there is significant error in the scattered field if absorption is neglected. Scattering of sound from sound absorbing surfaces has been investigated experimentally<sup>48-52</sup> and theoretically by using approximate shell theories<sup>53</sup>, by assigning a complex impedance boundary condition on the surface of the scatterer<sup>54-56</sup> and through the assignment of a viscosity throughout the body of the scatterer<sup>57,58</sup>. Since the scatterer to be studied is not homogeneous in the radial direction, i.e. layered, the approach by Gaunard<sup>57</sup> and Flax et al.<sup>58</sup> is most accurate. This approach solves the exact elasticity equation for the elastic cylinder coupled with the exact viscoelastic equation (plane strain case) for the absorptive layer. Gaunard<sup>59</sup> also solves the layer problem using the Sommerfeld-Watson transform method. The overall result is that the scatterer demonstrates both pressure release and rigid-like behaviors at different  $ka$  values. After these characteristic behaviors, resonance effects are observed. Gaunard's<sup>57</sup> material properties do not correspond to any known materials, so there can be no experi-

mental verification of his results. Flax and Nuebauer<sup>58</sup> solved the same problem as Gaunard with a lucite coating but, again, there is no experimental verification.

### Numerical Methods

There are a number of methods which can be used to determine the acoustic field scattered from a surface. It is often convenient to reformulate the scattered problem as a radiation problem. Chertock<sup>60</sup> proved this can be done with no loss of generality. Since most of these methods have been derived for the radiation problem, i.e. a vibrating surface in an infinite medium, this literature review will be based on this reformulation.

The radiation problem is conventionally posed as follows (see figure 1-2). An arbitrarily shaped finite object with a total surface area  $S$ , is contained in an infinite, ideal, homogeneous fluid. The density of the fluid,  $\rho$ , and the speed of sound,  $c$ , in the fluid are known. The region outside the surface is designated  $R_0$  and the interior region is designated  $R_i$ . An arbitrary point in  $R_0$  is designated  $x$  and an arbitrary point in  $R_i$  is designated  $x_i$ . Points on the surface  $S$  are designated  $x_s$ . The positive unit normal vector  $n_\xi$  is directed from a point on  $S$  into  $R_0$ . Only the steady state condition will be considered which implies the pressure and velocity are harmonic functions. The harmonic time dependence will be suppressed in this review. The boundary value problem requires that the pressure,  $p(x)$ , satisfy the Helmholtz equation for all  $x$  in  $R_0$ .

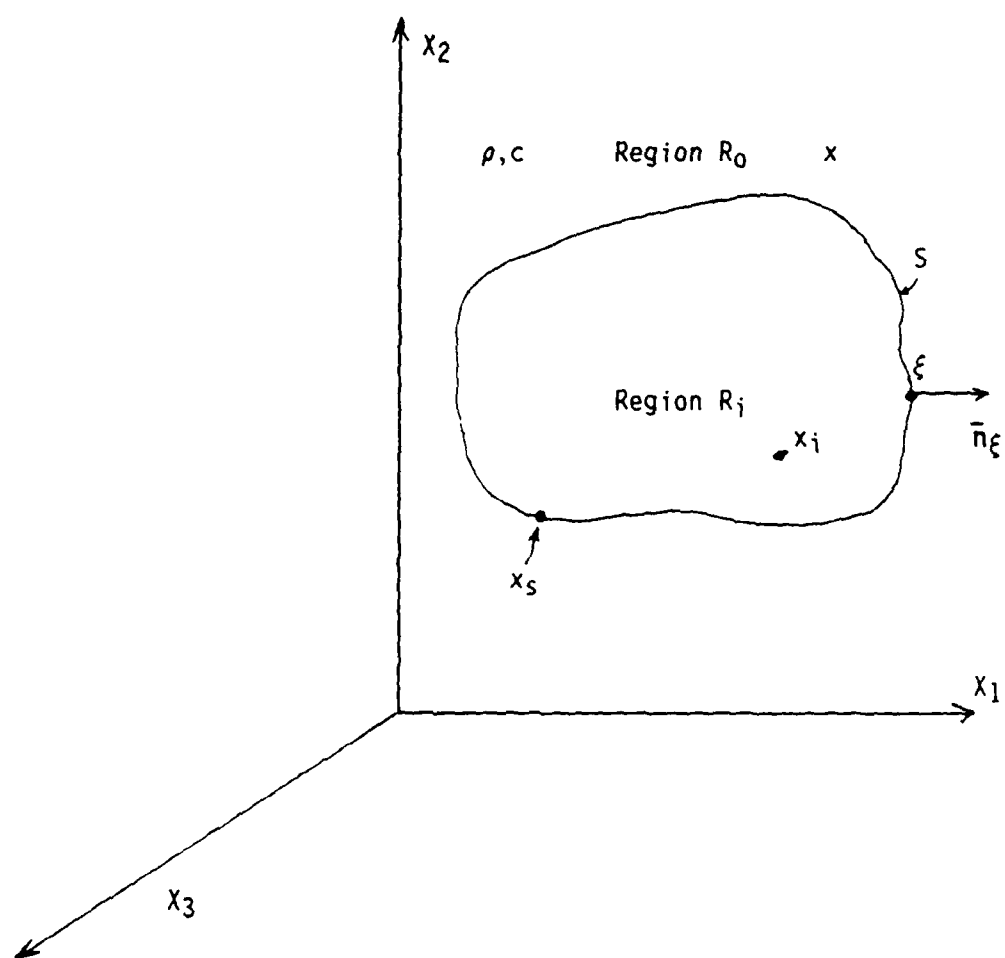


Figure 1-2 General scattering Geometry for Numerical Methods

$$(\nabla^2 + k^2)p(x) = 0 \quad (1-11)$$

The surface boundary condition is obtained from the normal component of Euler's equation

$$\frac{\partial p}{\partial n} = n \cdot (\nabla p(x))_{x=x_s} = -i\omega\rho V(x_s). \quad (1-12)$$

The pressure is also required to satisfy the Sommerfield radiation condition at infinity

$$\lim_{r \rightarrow \infty} r \left[ \frac{\partial p(x)}{\partial r} - ikp(x) \right] = 0. \quad (1-13)$$

The most straightforward method is to solve the wave equation directly using the classical method of separation of variables. This method, however, can be used only when the vibrating surface conforms to a separable coordinate system. (See Morse and Feshbach<sup>61</sup> for examples.) The normal mode method (Rayleigh series) for scattering works for those special cases when separable coordinate systems are usable for the radiation problem. A disadvantage of the normal mode method is that the calculation of the solution functions is not trivial nor always straightforward. Approximate solutions to the wave equation have been developed but these are extremely situation dependent with little generalization.

Due to the difficulty is solving the wave equation directly, alternate integral methods have been developed. During the 1960's four integral equation methods came into prominence. The first is the simple source formulation which has its origins in classical potential theory. The basic premise is that the pressure (potential) field can be represented by the integral over the surface of a simple source density function,  $\sigma(x_s)$ , times the free space Green's function. It is assumed that  $\sigma(x_s)$  is originally unknown.

$$p(x) = -i\omega\rho \iint_S \sigma(x_s) \frac{e^{ikr}}{r} dS(x_s) \quad (1-14)$$

The integrand of the above integral is singular as  $x$  approaches the surface but Kellogg<sup>62</sup> showed that the limit of the integral does exist and is continuous. The normal derivative of the integral is not continuous at the surface and must be accounted for. If the surface boundary condition is applied to an arbitrary point  $x_s$  on the surface, equation (9) becomes

$$v(x_s) = 2\pi\sigma(x_s) + \iint_S \sigma(x_s) \frac{\partial}{\partial n} \left( \frac{e^{i\omega r}}{r} \right) dS(x_s) \quad (1-15)$$

where the integral is an improper integral. Chen and Schweikert<sup>63</sup> demonstrated a method of subdividing the surface into  $N$  triangular elements and assuming  $\sigma(x_s)$  is constant over the each element. This formulation allows the integral to be written

in terms of  $N$  linear algebraic equations. Chen and Schweikert and Baron et al.<sup>64</sup> work several examples of this method for vibration of the acoustic medium and for vibration of elastic solids and shells in contact with the medium.

The remaining three methods are based on the Helmholtz Integral Method (HIM). The Helmholtz Integral determines the pressure at an external field point,  $x$ , in terms of the surface pressure,  $p(x_s)$ , and the normal surface velocity,  $v(x_s)$ .

$$4\pi p(x) = \iint_S \left[ p(x_s) \frac{\partial}{\partial n(x_s)} g(x, x_s) - i\omega\rho v(x_s) g(x, x_s) \right] dS(x_s)$$

$$\text{where} \quad g(x, x_s) = \frac{e^{ikr(x, x_s)}}{r(x, x_s)} \quad (1-16)$$

The normal surface velocity and surface pressure are related by two integral equations called the Surface Helmholtz Integral Equation (SHIE) and the Interior Helmholtz Integral Equation (IHIE). A complete discussion of the HIM may be found in Baker and Copson<sup>65</sup>. Chertock<sup>66</sup> points out a low and high frequency approximate relation between the surface pressure and surface velocity. In the low frequency limit the in phase component of the surface pressure is considered negligible and

$$p(x_s) = i\omega v(x_s) m(x_s) \quad (1-17)$$

where  $i\omega v(x_s)$  is the local acceleration and  $m(x_s)$  is the entrained mass per unit area. For low frequencies,  $m(x_s)$  varies slowly and is calculated from incompressible flow theory. For the high frequency case, the surface is approximated as a sphere of radius  $a$ , where  $a$  is the local mean radius of curvature of the surface.

$$p(x_s) = \rho c v(x_s) \left[ 1 - \frac{1}{ka} \right] \quad (1-18)$$

This approximation is usually valid for  $ka \gg 1$ . A derivation and additional restrictions for this approximation can be found in Morse<sup>67</sup>.

In the 1930's Kupradze<sup>68</sup> developed what has become known as the Surface Helmholtz Integral Equation. To develop this equation, the point  $x$  in  $R_0$  is allowed to approach the surface  $S$ . The results in the following two dimensional inhomogeneous Fredholm equation of the second kind

$$p(x_s) = 2 \iint_S \left[ p(x_s) \frac{\partial}{\partial n(x_s)} g(x, x_s) - i\omega \rho v(x_s) g(x, x_s) \right] dS(x_s)$$

where

$$g(x, x_s) = \frac{e^{ikr(x, x_s)}}{r(x, x_s)} \quad (1-19)$$

The actual method of solution, i.e. Surface Helmholtz Integral Equation Method



(SHIEM), is to solve the surface Helmholtz integral equation for the surface pressure given the surface velocity. Then utilizing the surface pressure and surface velocity, the HI is solved for the field pressure. Chertock demonstrates a method of solution for surfaces of revolution and reduces equation (1-19) to one-dimensional form. Banaugh and Goldsmith<sup>69</sup> describe a related approach for two-dimensional problems.

The third method pioneered by Copley<sup>70</sup> has become known as the Interior Helmholtz Integral Equation Method (IHIEM). It is developed by defining the pressure interior to the surface, region  $R_i$ , as zero for all  $x_i$  resulting in

$$0 = \iint_S \left[ p(x_s) \frac{\partial}{\partial n(x_s)} g(x_i, x_s) - i\omega\rho v(x_s) g(x_i, x_s) \right] dS(x_s) \quad (1-20)$$

This equation, the interior Helmholtz integral equation, defines an acoustic relation between the surface pressure and the normal surface velocity which then allows usage of the exterior Helmholtz Integral (HI) to determine the exterior field pressure.

The three previous methods have significant difficulties which are described in detail by Schenck<sup>71</sup>. In summary, the simple source formulation does not always exist and the surface Helmholtz Integral equation (SHIE) does not have unique solutions at or near certain characteristics frequencies or wave numbers (these are eigenvalues of the interior Dirichlet or Neumann problem). Schenck determines

additional compatibility relations which must be satisfied for the SHIE to yield a unique solution for all frequencies. The Interior Helmholtz Integral Equation Method, IHIE, is unique in principle but exhibits numerical computational problems.

To facilitate usage of the first two methods, knowledge of the characteristic frequencies is required so they can be avoided. This requires solving the interior eigenvalue problem first. Since numerical approximations are involved in discretizing the integrals, a range of values for each characteristic frequency is required. The numerical approximation effect becomes increasingly more important at higher frequencies due to a reduction in the interval between the characteristic wave number associated with the higher frequencies. The overall result is that these methods are not generally satisfactory without additional modifications or knowledge.

To eliminate the lack of uniqueness, Schenck<sup>71</sup> proposed the Combined Helmholtz Integral Equation Formulation (CHIEF). Basically CHIEF discretizes the surface Helmholtz integral equation into an  $N$  by  $N$  system of equations and then overdetermines the system by forcing additional compatibility equations to be satisfied. The additional compatibility equations are, in fact, the interior Helmholtz integral equation applied at selected interior points. Meyer et al.<sup>72</sup> points out two difficulties with CHIEF: (1) there is no simple method to determine how many additional interior compatibility equations are required to sufficiently overdetermine the system thereby eliminating the nonunique solutions. (2) there is

no scheme for choosing the appropriate interior points except to avoid obvious symmetry points. Rogers<sup>73</sup> develops a method to determine how many additional interior points are required by using eigenvalue decomposition. Recently (August 1986) Benthein and Barach<sup>74</sup> and Naval Ocean Systems Center, San Diego reissued CHIEF in a general program (fortran) format with modern memory (storage) allocation procedures which allows rapid program runs with different compatibility points so as to arrive at a "best" solution. This new version also includes a point source check feature.

A variation of CHIEF has been proposed by Shaw<sup>75</sup>. In this method additional points are placed in the exterior region,  $R_O$ , to overdetermine the exterior Helmholtz integral equation. Unlike the interior problem, the potential (pressure) at the additional field points is unknown and must be solved by iteration.

One method of eliminating the uniqueness problem is to use a different Green's Function. Ursell<sup>76</sup> provides a new function which involves the computation of infinite series. The shortcomings of this method are primarily computer related.

Burton<sup>77</sup> points out that a modified differentiated form of the surface Helmholtz Integral Equation (SHIE) also describes the surface pressure. It also has nonunique solutions corresponding to internal eigenvalues of the associated interior equation, but these are different from the eigenvalues of the previous interior Helmholtz Integral Equation (IHIE). The differentiated form results from

taking the normal gradient of the surface Helmholtz Integral Equation (SHIE).

This yields a Fredholm equation of the first kind.

$$\frac{\partial p(x)}{\partial n(x)} = \frac{1}{2\pi} \iint_S p(x_s) \frac{\partial^2 g(x, x_s)}{\partial n(x) \partial n(x_s)} - v(x_s) \frac{\partial g(x, x_s)}{\partial n(x)} dS(x_s) \quad (1-21)$$

The significant observation by Burton and Miller<sup>78</sup> was that combining the surface Helmholtz Integral Equation (SHIE) and its differentiated form results in a solution that is common to both equations. Since the eigenvalues are different for each equation, the solution of the combined equation will be unique. This combined equation is the starting point for Meyer et al.<sup>72</sup> application to radiation.

The combined equation is

$$p(x) + \alpha \frac{\partial p(x)}{\partial n(x)} = \frac{1}{2\pi} \iint_S \left[ p(x_s) \frac{\partial}{\partial n(x_s)} g(x_i, x_s) - i\omega\rho v(x_s) g(x_i, x_s) \right] dS(x_s) + \alpha \frac{1}{2\pi} \iint_S p(x_s) \frac{\partial^2 g(x, x_s)}{\partial n(x) \partial n(x_s)} - v(x_s) \frac{\partial g(x, x_s)}{\partial n(x)} dS(x_s) \quad (1-22)$$

where  $\alpha$  is a coupling constant. Meyer et al. points out that the term

$$\iint_S p(x_s) \frac{\partial^2 g(x, x_s)}{\partial n(x) \partial n(x_s)} dS(x_s) \quad (1-23)$$

is strongly singular and can not be numerically integrated. A method of overcoming this problem is then presented. Teraï<sup>79</sup> has also treated the highly singular integral by reducing it to a contour integral which is nonsingular for most practically realizable surface elements. The selection of  $\alpha$  is recommended to be  $-\iota/k$  by both Reut<sup>80</sup> and Meyer et al.

In an effort to evaluate which method to use, Tobocman<sup>81</sup> conducted a study of scattering from a rigid sphere in the intermediate wavelength region (i.e. wavelength comparable to target dimensions) using both CHIEF and the Burton-Miller method. The study was performed at four characteristic wave numbers between 3 and 10. The conclusion is that CHIEF converges more rapidly than the Burton-Miller method but at higher wave numbers,  $k > 10$ , CHIEF is more time consuming and becomes impractically slow. In the frequency range of interest, CHIEF out performed the Burton-Miller method both in time considerations and accuracy. A surprising result is that at higher characteristic wave numbers, the surface Helmholtz Integral Method (SHIEM) (without overdetermination) showed an increase in accuracy and was on the order of the Burton-Miller method. Therefore, if precise accuracy is not required at higher wave numbers, the SHIEM will give rapid results. Since this was shown for the rigid sphere only, extension to other geometries is cautioned.

The Simplified-Helmholtz-Integral Program (SHIP) developed by Rogers<sup>82</sup> solves the Helmholtz Integral (using the SHIEM) specifically for finite circular cylinders and free-flooded ring transducers. SHIP takes full advantage of the axial symmetry which results in the high speed of this method relative to others. The standard approach of the previously discussed methods is to solve the SHIE by dividing the surface into small surface subdivisions and solving the surface integrals. The axial symmetry allows: 1. the surface to be divided into bands (no division in  $\theta$  direction) which reduces the number of elements. 2. the conversion of the surface integrals into ordinary line integrals. For application to the scattering problem, SHIP requires complete axial symmetry and is, therefore, only usable for axial or end on incidence. SHIP is easily adaptable to the pressure release boundary condition.

The follow-on step to the overall scattering problem is to match the acoustic radiation condition with the structure reaction or fluid-structure coupling. This is accomplished by matching the normal surface velocity defined by the elastic equilibrium relations with that defined by the equations of the fluid field (HI). Mathews<sup>83</sup> developed a program called ADRAD which uses the finite element technique for the structural material and the Burton-Miller method for the fluid. He strongly recommends that CHIEF be avoided due to the previously mentioned problems.

Recently little has been done to improve the theoretical treatment of the radiation problem although gains have been made in the numerical implementation of the integral equations. Schuster and Smith<sup>84</sup> and Seybert et al.<sup>85</sup> have developed a more sophisticated boundary integral equation method of solution by using elements that are curvilinear and by representing acoustic variables with higher order interpolation functions in lieu of the planar elements and piecewise constant acoustic variables. The result is greater accuracy for the same number of elements, less computing time, but a more complicated formulation is required.

Waterman<sup>86</sup> developed an alternative method to the HIEM called the T-Matrix method (TMM). In this method the potential field is expanded in terms of the spherical wave functions which is then substituted into the Helmholtz equation. The result is a set of linear algebraic equations for the expansion coefficients. Tobocman<sup>87</sup> compares the two methods for a rigid prolate spheroid of various aspect ratios. His conclusions are summarized as follows: (1) The TMM converges more rapidly than the HIEM for spherical targets. (2) The rate of convergence deteriorates very rapidly for the TMM with increasing aspect ratios but the convergence of the HIEM shows little change. (3) The TMM was severely affected by overflow and roundoff error. (4) As the number of partial waves is increased in the TMM, the matrix which must be inverted becomes increasingly ill conditioned which is exactly opposite from the HIEM. Numrich et al.<sup>88</sup> has extended the TMM to finite cylinders using cylindrical basis functions. Additional results and usages of the TMM may be found in Varadan and Varadan<sup>89</sup>.

An alternative to the previously discussed methods is to utilize variational formulations to solve the Helmholtz integral equation. Until the recent work by Wu, et al.<sup>90</sup> and Pierce<sup>91</sup> very little interest in this approach has occurred since the 1950's. Morse and Feshbach<sup>61</sup> contains a summary of this previous work. Wu, et al., demonstrates a new approach of the variational principle to the Helmholtz integral equation (i.e. formulation contains all self-adjoint kernels) to transversely oscillating disks. Pierce derives a stationary expression for radiated acoustic power and target strength. In addition, Pierce discusses some alternatives or tricks to enhance the solution of the variational formulation but suggest additional study is required for comparison with other computational algorithms.

CHIEF has proven to be reliable for the finite cylinder particularly since the characteristic frequencies are well known. The particular advantages of the Benthien and Barach CHIEF program<sup>74</sup> is that it is pre-programmed for numerous coordinate systems which allows the program to be applied to an almost unlimited number of shapes. As the shape becomes more complex, the determination of the number and locations of the eigenvalues becomes almost impossible. The aforementioned program allows the easy input of numerous interior points which partially mitigates this problem. For scattering from the finite cylinder with axial incidence, the most accurate and computationally efficient alternative is SHIP<sup>82</sup>.



### Determination of Dynamic Viscoelastic Moduli

The closed cell rubber materials are considered to be viscoelastic with high losses. As with most rubbers, the dynamic behavior is strongly frequency, loading, and temperature dependent. The manufacturing process is also important, in particular, the addition of fillers such as carbon black<sup>92</sup> and the cure times. There are four distinct classes of methods employed to determine the dynamic viscoelastic constants:

1. free vibration method.
2. direct observation of stress-strain curves.
3. resonance methods.
4. wave propagation methods.

The free vibration method has been extensively utilized since its main advantage is simplicity. The method is particularly suitable for measurements at low frequencies and for low loss materials. Lethersich<sup>93</sup> has demonstrated the free vibration method for frequencies up to 1000 Hertz using photographic recording methods. The direct stress-strain method requires special equipment and involves considerable difficulties in determining the stress-strain curve at high loading rates. Kolsky<sup>94</sup> points out the advantage of this method is that no assumptions are made regarding the nature of the dissipative forces and the linearity of the system. The three other methods assume linearity (mechanical behavior is independent of

amplitude) and that the dissipative force is proportional to the time rate of change of the strain.

In the audio frequency range, the dynamic moduli and loss factors are best determined by resonance methods which are described by Read and Dean<sup>95</sup> and by wave propagation methods. There are basically three types of vibrations employed in resonance studies which in order of increasing frequency range, are (1) flexural, (2) torsional and (3) longitudinal. For isotropic materials, Read and Dean state that the complex Young's modulus is customarily determined from flexural resonance tests in the frequency range of 20 Hz to 10 kHz and by longitudinal resonance tests in the frequency range of 5 kHz to 50 kHz. The torsional resonance tests give the complex shear modulus for frequencies greater than 500 Hz. All of these tests are inherently low amplitude with average strain amplitudes on the order of  $10^{-6}$ . This low amplitude generally eliminates any problems with nonlinearity of the dynamic properties.

The method of exciting the flexural waves (i.e. free-free, clamped-free etc.) is important since significant errors and spurious resonances may be introduced. The flexural resonance method originated with Ide<sup>96</sup> and has undergone numerous improvements as test equipment and theory have evolved. Spinner and Tefft<sup>97</sup> provide an excellent summary of the methods and theory. Tefft and Spinner<sup>98</sup> also provide a review of torsional measurements for rectangular and cylindrical bars.

The longitudinal resonance method was first utilized by Quimby<sup>99</sup> who compared the resonances in a viscoelastic bar, determined by Stokes' theory, with the experimental results for glass, copper and aluminum bars. Quimby excited the specimen bar by attaching an oscillating quartz (piezoelectric) crystal to one end and then measured the particle velocity at the other end. The correlation between the experimental and theoretical results was considered excellent.

Ballou and Silverman<sup>100</sup> modified the technique by using a light source and photoelectric cell at the free end to record the displacement. Norris and Young<sup>101,102</sup> used the longitudinal resonance method and attached accelerometers to both ends. The fixed end was driven by a constant frequency source. Madigosky and Lee<sup>103</sup> improved on Norris and Young's technique by using miniature accelerometers (Bruel & Kjaer type 8307) and a random noise source as the forcing mechanism. The accelerometer signals were analyzed using a Fast Fourier Transform (FFT) spectrum analyzer. Both Norris and Young and Madigosky and Lee utilized Lee's<sup>104</sup> observation that if the frequency is adjusted such that the two ends are out of phase by 90 degrees, the resonances are easily determined. Madigosky and Lee also demonstrate wide applicability to both soft (lossy) polymers and rigid metals. Capps<sup>105</sup> has used this method to determine the dynamic Young's modulus of some commercially available polyurethanes. No published data for closed cell rubbers or corprene appears to be available<sup>106,107</sup>

Cramer<sup>108</sup> compares the Young' modulus determined by the flexural resonance method and by the longitudinal resonance method for rubber rods in the

1kHz to 8kHz region. He concluded that they agreed within the experimental accuracy.

Nolle<sup>109</sup> has investigated the elastic properties of rubber-like materials for frequencies between 0.1 Hertz and 120,000 Hertz using a combination of five experimental methods (one free oscillation method, three resonance methods and one wave propagation method).

The wave propagation methods have been extensively used for non-dispersive materials and ultrasonic measurements. Kolsky<sup>94</sup> points out the advantages of this method over the other methods are:

1. a large range of frequencies can be covered with a single specimen (specimen sizing is not particularly critical).
2. in determining the attenuation, losses caused by extraneous supports can easily be removed.
3. the method is highly accurate for non-dispersive materials.

Two disadvantages of the wave propagation method are:

1. generation of the particular wave of interest can be complicated.
2. interpretation of the results for dispersive materials can be very involved.

This investigation will use wave propagation methods.

Master curves (complex modulus-frequency and loss factor-frequency curves at constant temperature) can be generated for modulus measurements at different frequencies and temperature. This procedure is based on the time-temperature

superposition principle outlined by Ferry<sup>110</sup>. This principle is based on the viscoelastic material becoming more elastic due to greater molecular mobility as its temperature is increased at constant frequency. The converse is also observed. The result is that a decrease in temperature at constant frequency causes the same change in dynamic properties as an increase in frequency at constant temperature. Although there is no limit to the range this data may be shifted, Madigosky and Lee suggest that reliable interpolation is assured two decades above and below the measured range.

For rubber-like materials it is well established that Poisson's ratio,  $\nu$ , is approximately 0.49. Since the materials to be studied have large concentrations of air, it is expected that the Poisson's ratio will be less than 0.49 but it is unclear how much less.

The plane wave modulus,  $M$ , can be determined from the longitudinal wave speed. The common method of determining the wave speed is by using pulse and comparing arrival times with and without the material present. The attenuation, corrected for spreading loss and reflection, will yield the complex wave speed in the material.

The reflection and transmission coefficients are experimentally determined from panel measurements at various angles of incident (panel measurements involve placing a flat panel of the material with a known thickness in a sound field and measuring the transmission through or reflection off the panel. The panel

dimensions are usually large enough so that the panel may be considered one dimensional, i.e. an infinite planar surface). The experimental technique is documented by Barnard et al.<sup>111</sup> and the theory is based on the work of Brekhovskikh<sup>112</sup>. Folds and Loggins<sup>113</sup> corrected the errors in Brekhovskikh and Barnard et al. and extended the theory to multiple layers using a matrix approach.

To predict the elastic behavior of the material, two moduli must be determined. The plane wave modulus is determined from panel measurements and the Young's modulus,  $E$ , is determined from wave propagation in a bar. Losses in the material are accounted for by allowing the elastic constants to be complex (now, they are technically viscoelastic constants). The following assumptions concerning the materials are made:

1. The material is isotropic.
2. The air inclusions are relatively uniform in size and dispersion (homogeneous).
3. The air inclusions are small relative to a wavelength.
4. The material is stressed within the elastic limit.
5. The amplitude of the acoustic displacement is small enough so as to not affect the dynamic moduli.

The first assumption implies that the elastic properties are the same in all directions. Homogeneous implies that the results will be sample independent. The third assumption allows the material to be treated as a composite. The fourth

assumption allows the material to be modeled with classical elasticity theory. The final assumption eliminates displacement amplitude as an independent variable in the determination of the elastic constants for small amplitudes<sup>114</sup>.

## CHAPTER II

### Experimental Procedures

The experimental procedures are divided into two categories: determination of viscoelastic constant and acoustic scattering experiments.

#### Determination of Material Viscoelastic Constants

The materials investigated are grouped into two classes: closed-cell rubbers and rubber-cork composites. All materials are assumed to be isotropic. The four materials are:

neoprene rubber with air cells (RUBATEX* No. R-411-N)	}	closed-cell rubbers
nitrile rubber with air cells (RUBATEX* NO. R-416-N)		
neoprene rubber with cork (GROENDYKE* No. 712 [corprene])	}	rubber-cork composites
nitrile rubber with cork (GROENDYKE* No. 725)		

(\* refers to RUBATEX Corporation and GROENDYKE Manufacturing Company, corprene is the tradename of the ARMSTRONG Rubber Company)



In order to fully characterize the material, two viscoelastic constants and the density are required. The viscoelastic constants will be treated as complex elastic constants. The density is determined by the standard method of weighing a known volume of the material. The measured densities are all within the manufacture's specified ranges. The constants that are determined are the complex Young's modulus,  $E$ , and the complex plane wave modulus,  $M$ .

#### Complex Young's Modulus

The complex Young's modulus is determined from the relation

$$E = \rho c_e^2 \quad (2-1)$$

where  $c_e$  is the complex bar speed. The experimental setup is shown in figure 2-1. A long rectangular strip of the material is glued to a Bruel and Kjaer (B&K) shaker which is driven by a broadband pulse produced by a Wavetek model 275 signal generator and amplified by a Kronhite Model 7500 amplifier. The lateral dimensions of the strip are approximately .25 inches with a length of greater than 30 inches. Since the length is very much larger than the other two dimensions, the significant propagating wave is the extensional wave which is governed by the Young's modulus.

# YOUNG'S MODULUS MEASUREMENT

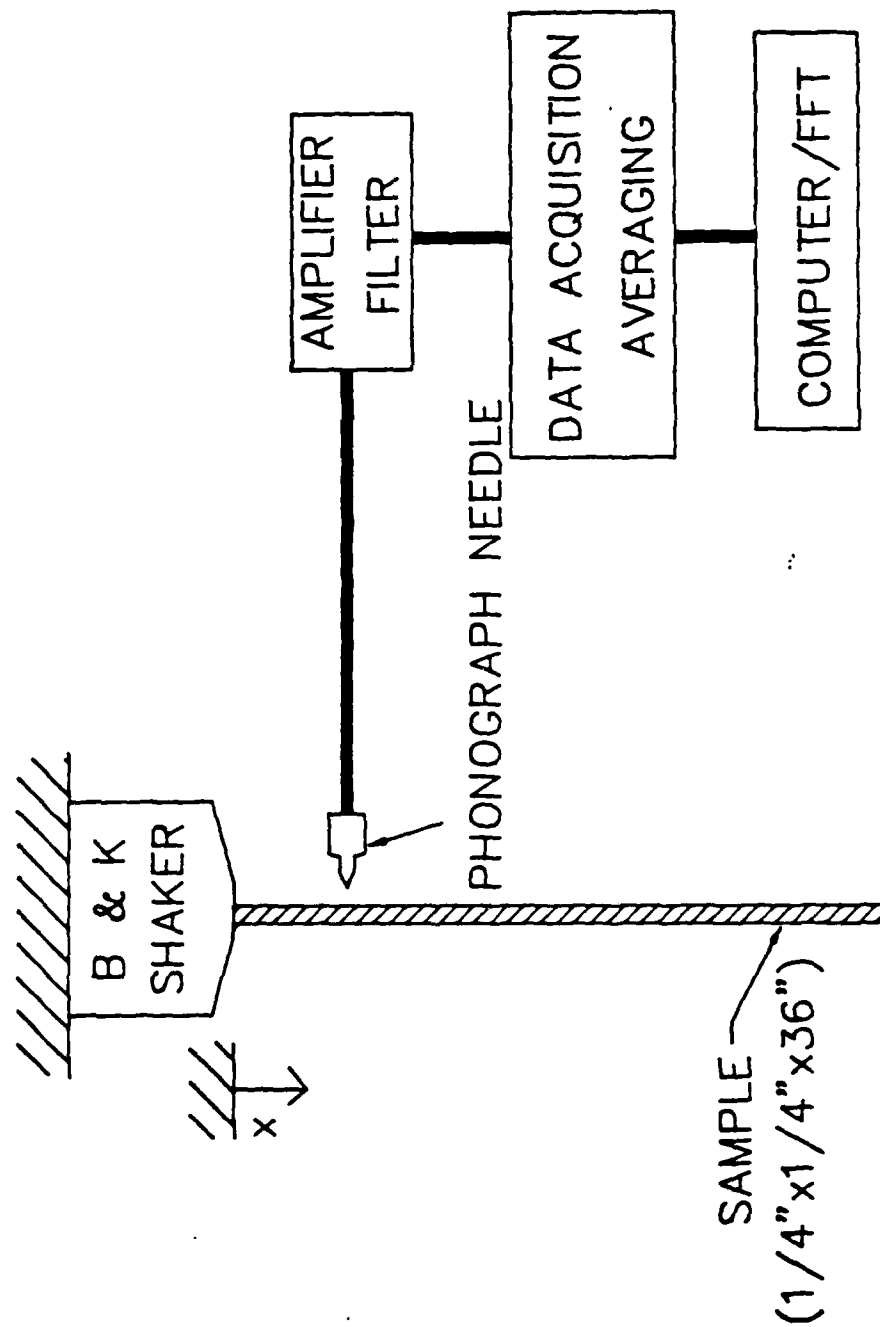


Figure 2-1 Experimental Apparatus for Young's Modulus Measurement

The procedure is to record the broadband pulse waveform at three locations along the sample and at several center frequencies. The filter settings remained constant for each center frequency group so as to ensure a consistent time delay. Each waveform was time shifted to place the earliest pulse for a particular center frequency group near the time origin. This shift is somewhat arbitrary and not always the same for all groups. It is of paramount importance that the time shift be the same for all samples within a particular center frequency group. A fast Fourier transform (FFT) (standard IMSL FFT routine used) is then performed on the shifted waveform. The purpose of the time shift is to reduce the frequency of discontinuities in the FFT phase caused by the signal being time displaced from the origin. Although it is not theoretically required, the reduction of the numerous phase discontinuities facilitates unwrapping (removal of the  $2\pi$  discontinuities resulting from the tangent function). The phase speed is determined from

$$c = \frac{\omega L}{\Delta\phi + n2\pi} \quad (2-1)$$

where  $\Delta\phi$  is the unwrapped phase difference and  $L$  is the distance between two measurement points. Since the exact multiple of cycles between the two sample points is not obvious, the  $n2\pi$  multiple is required for proper scaling. The  $2\pi$  multiple is determined from the time domain waveform. The time difference between two apparently similar points on the two pulses is measured to obtain an estimate of the phase speed. Ideally the center of the pulse should be used for

estimation, however this point is often difficult to ascertain; therefore the largest peak was used and assumed to be at the center frequency. An error in the selection of  $n$  is easily recognized since there is a significant deviation in the calculated phase speed from the estimated value. The distance between sample points was kept small so as to prevent significant distortion of the waveform caused by dispersion. Specifically, the  $2\pi$  multiple is determined from

$$n2\pi = \frac{\omega L}{c_{\text{est}}} - \Delta\phi \quad (2-2)$$

The ratio of the FFT amplitudes determines the attenuation by

$$\alpha = -\frac{1}{L} \log_e \left[ \frac{\text{Amp}_2}{\text{Amp}_1} \right] \quad (2-3)$$

The FFT amplitudes also determine the boundaries of the usable frequency range for the individual center frequencies. There is no specific guidance as to what amplitude decrease from the maximum results in meaningless data. The procedure employed is to use data with amplitudes greater than 10% of the maximum (center frequency) amplitude and evaluate the data using a "reasonableness criteria". The "reasonableness criteria" is based on:

1. there is sufficient overlap between frequency bands that the values should be approximately the same.
2. the speed and attenuations of these materials are slowly varying

(increasing) with frequency.

3. the frequency spacing is small enough so as to ensure large variations between individual frequency points do not occur.

The wave was recorded at each sample location using a stereo phonograph needle as a displacement sensor. The two outputs from the needle were summed using an Ithaco preamplifier operating in the differential input mode which maximizes the normal displacement. The amplitude of the signal is not dependent on the contact pressure provided contact is maintained and the pressure is not great enough to cause the needle to contact the backing assembly which results in distortion of the observed waveform.

The sample was suspended vertically with the shaker at the top. The bottom of the sample was glued to a 2 inch square lead block simulating a rigid boundary condition. Attenuation in all the test materials was large enough to require the sample points be located near the shaker. The attenuation and large distance from the rigid end allows multiple reflections to be neglected.

Since temperature control facilities were not available, complete master curves were not obtained. Extrapolation of the data using a log-log plot has been shown to be valid for up to 2 decades above and below the measured data (see Madigoski and Lee<sup>103</sup>). The data was obtained over the approximate frequency range of 300 Hz to 3000 Hz. The upper frequency is limited by attenuation causing the observed pulse to be dominated by noise. The maximum frequency required for the shell modeling is 60,000 Hz which can be obtained by extrapolation.

The above measurement procedure is subject to the following sources of errors:

1. errors in digitizing the data.
2. computer round off error during the FFT procedure.
3. misalignment of the sample over the center of the shaker causing introduction of surface and flexural waves.
4. error in determining the distance between sample points resulting from uncertain positioning of the stereo needle.

Errors introduced by means 1 and 2 are random and assumed to be very small resulting in a less than 1% combined error. The generation of surface and flexural waves can be disregarded since they travel slower than the extensional wave and are highly attenuated. It is estimated that the sample point locations are accurate to within 2mm resulting in a possible 10% error for small sample point separations at the higher frequencies.

#### Plane Wave Modulus Determination

The plane wave modulus is also determined by traveling wave techniques. The experimental apparatus is illustrated in figure 2-2. A broadband pulse is generated by a USRD F-33 transducer and measured by a B&K 8103 hydrophone. The 8103 hydrophone is placed on the central axis of the F-33 transducer. A 36 inch by 36 inch panel of .25 inch thick sample material is placed between the F-33 transducer and the 8103 hydrophone. The sample is attached to a wood frame for

# TRANSMISSION MEASUREMENT

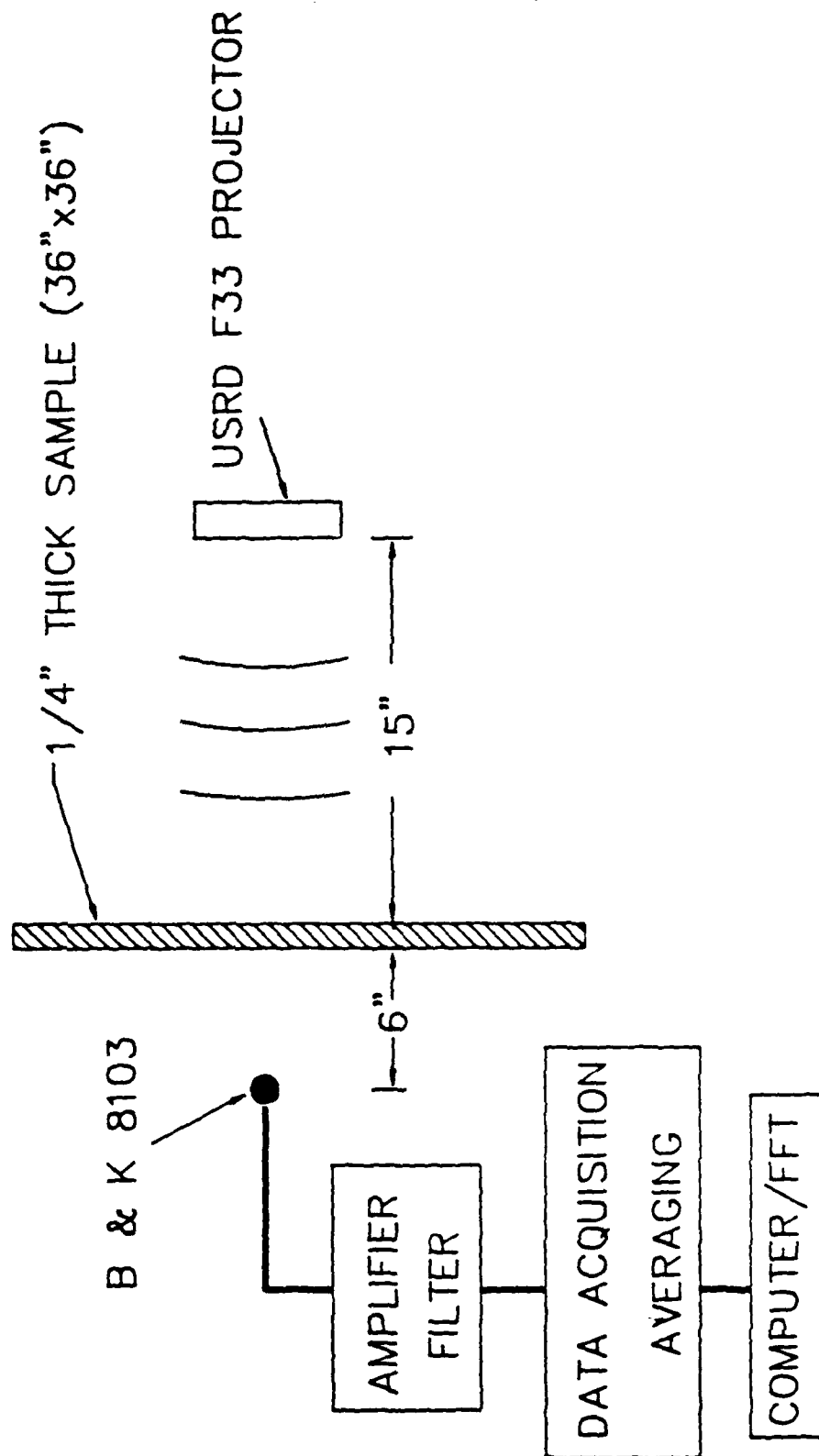


Figure 2-2 Experimental Apparatus for Plane Wave Modulus Measurement

support and is weighted so as to suspend vertically. The panel is positioned 15 inches (38 cm) from the F-33 transducer. This places the panel in the far field of the transducer for all measured frequencies. Far field measurements are utilized so as to avoid the axial (z axis) field amplitude variations that occur in the near field of a piston-type transducer such as the F-33. In addition, far field measurements allow the usage of a receiving hydrophone (8103) which is physically smaller than the projector (F-33 transducer) since the x-y field variations that exist in the near field are mitigated. For a frequency of 50 kHz, transition to the far field occurs at 13.1 inches ( $= [\text{F-33 radius}]^2/\lambda$ ). As illustrated in figure 2-3, for 15kHz the columnar portion of the axial field (near field) extends for a distance of 3.94 inches (10 cm) from the F-33 transducer. This results in a spreading angle of  $45^\circ$  from the center axis; therefore at the panel location of 15 inches from the transducer, the sound will cover 15 inches of the panel in the x-y plane. Diffraction by the edges of the panel could interfere with the received signal for frequencies less than 15kHz.

The experimental procedure is to record the waveform from the 8103 hydrophone with and without the panel in place. An FFT is performed on the signal as was done in the Young's modulus experiment. From a comparison of the FFT data, the phase speed and attenuation is obtained. The closed cell rubbers are highly attenuating and multiple internal reflections within the panel can be neglected. The phase speed,  $c_s$ , is calculated from



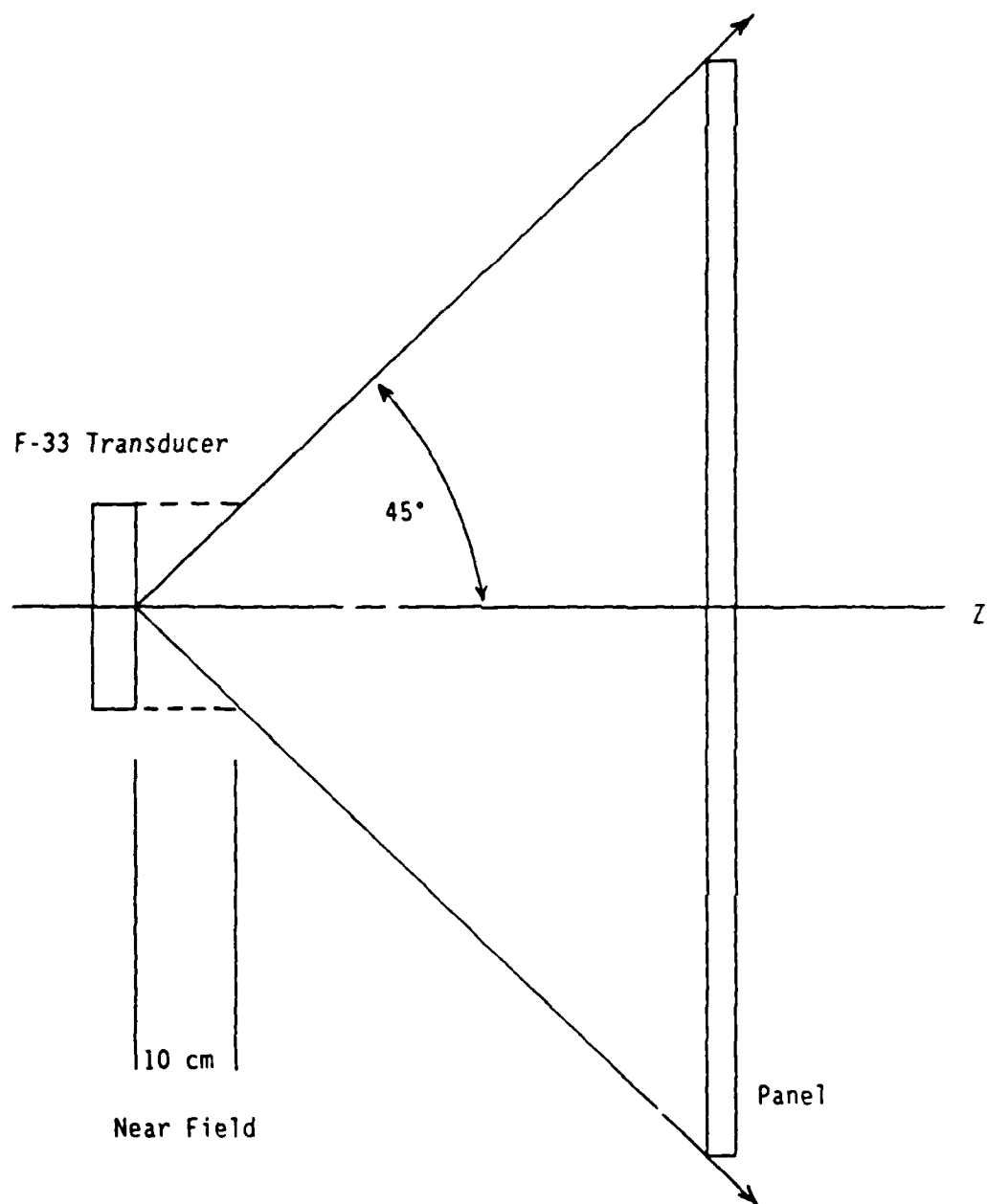


Figure 2-3 F-33 Beam Spreading at 15 kHz for Panel Measurement

$$\frac{\Delta\phi}{\omega L} = \frac{1}{c_s} - \frac{1}{c_w} \quad (2-4)$$

where  $L$  is the panel thickness (0.25 inches (0.635 cm)),  $c_w$  is the phase speed in water ( $1.5 \times 10^5$  cm/sec), and  $\Delta\phi$  is the unwrapped phase difference between the two signals. The attenuation,  $\alpha$ , is determined from

$$\frac{P_{\text{with panel}}}{P_{\text{without panel}}} = \frac{4 r_1 r_2}{(r_1 + r_2)^2} e^{-\alpha L} \quad (2-5)$$

where  $r_1$  is the specific acoustic impedance of the water ( $= \rho_w c_w$ ) and  $r_2$  is the specific acoustic impedance of the panel ( $\rho_2 c_2$ ). The internal multiple reflections for the corprene and cork-nitrile composites can not be neglected and are removed by an iterative method described in Appendix E.

There are four possible sources of error in this experimental procedure:

1. errors in the digitizing of the data.
2. computer round off error during the FFT procedure.
3. misalignment of the F-33 transducer, panel, or 8103 hydrophone.
4. diffraction effects.

The first two error are the same as for the Young's modulus experiment and are considered very small. Misalignment resulting from the F-33 transducer and the panel not being exactly parallel results in a variation of the effective thickness. A  $10^\circ$  misalignment will cause an error of 1.5% in the speed measurement.

Additionally, shear and flexural waves can now be generated in the panel. The fourth source of error, diffraction effects, is avoided by setting the lowest usable frequency greater than 15kHz. Since the wave generation effects will not be investigated, the maximum error assumed will be equal to the maximum data spread for the same frequency between two adjacent center frequency data groups. The maximum observed data spread in the phase speed measurement was 7%.

### Scattering Experiments

Two basic scattering experiments were performed: (1) scattering at normal incidence from a long circular tube simulating an infinite cylindrical shell, and (2) scattering from a thick, finite cylindrical shell with flat end caps. The pertinent distances for the scattering experiments are determined acoustically.

#### Infinite Cylinder Experiment

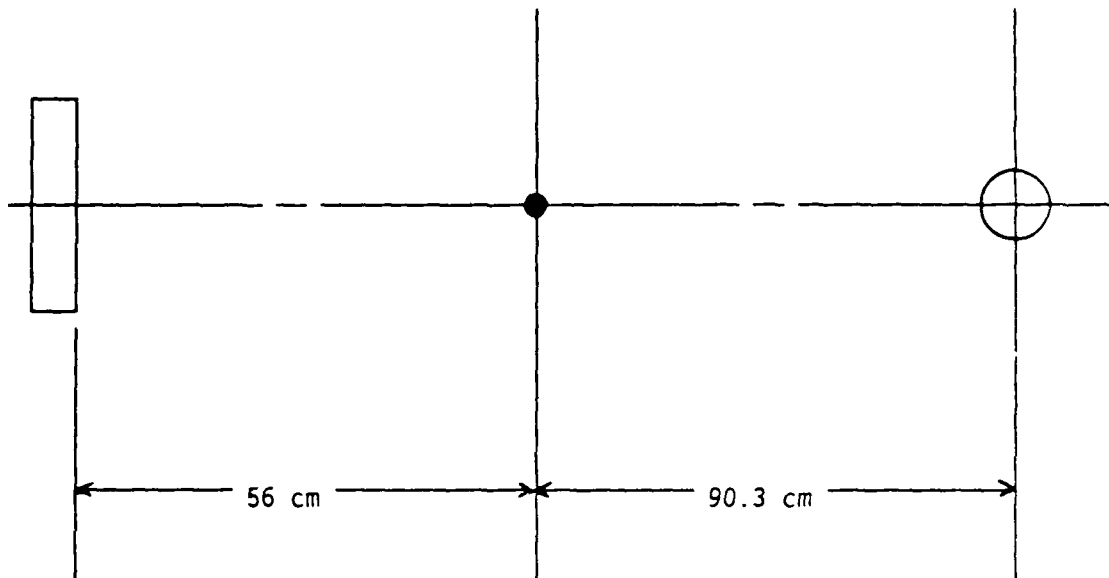
For the infinite cylinder simulation, the tube is commercial grade, seamless, 304 stainless steel tubing with an outside radius of 1.5 inches (3.81 cm) and a wall thickness of 0.035 inches (0.089 cm). The ratio of inner to outer radii is 0.977 which implies the tube should scatter like a thin shell. The length of the tube is 8 feet.

The experimental setup is illustrated in figure 2-4. The acoustic source is a USRD F-33 transducer. The receiving hydrophone is a B&K 8103 hydrophone. Both the cylinder and F-33 are suspended vertically which ensures they are

F-33 Transducer

8103 Hydrophone

Shell



$$d_1 = 56 \text{ cm} + 90.3 \text{ cm} = 146.3 \text{ cm}$$

$$d_2 = 90.3 \text{ cm}$$

Figure 2-4 Experimental Setup for Infinite Shell Measurements

parallel. The B&K 8103 and target are both located in the far field of the transducer. Due to the length of the target and location of the transducer, end effects of the target are negligible for center frequencies greater than 18 KHz. Since broadband pulses were used, the scattered signals from the ends could be time-gated out for center frequencies less than 18 KHz. The measurements are taken over an approximate ka range of 1.5 to 15 using ten broadband pulses. The reference (incident) signal is obtained by replacing the target with the B&K 8103 hydrophone (at the same physical location). The FFT amplitude of the reference signal is compared to the FFT amplitude of the scattered signal to determine the form function.

The scattered signal must be corrected for spherical spreading in the vertical plane since the incident wave is spherical not planar. The form function corrects for cylindrical spreading in the horizontal plane. Spherical spreading in the backscatter direction can be represented as cylindrical spreading in two orthogonal planes; therefore the scattered signal is multiplied by

$$\text{correction} = \sqrt{\frac{d_1 + d_2}{d_1}} \quad (2-6)$$

where  $d_1$  is the distance from the F-33 transducer to the center of the target and  $d_2$  is the distance from the center of the target to the 8103 hydrophone.

The following four experiments are performed:

1. uncoated shell only.
2. .25 inch (.635 cm) nitrile coated shell.
3. .0625 inch (.159 cm) corprene coated shell.
4. .3125 inch (.794) corprene coated shell.

The coatings were glued with contact cement and care was taken to prevent any air inclusions between the coating and the shell. The seams of the coating were placed on the forward scatter side of the target.

The measurements on the uncoated shell were used to validate the experimental method and theoretical calculations since similar results are well documented. The purpose of the two thicknesses of corprene was to determine if a pressure release boundary condition could be achieved and the effect of thickness towards the realization of this goal. A secondary purpose of the two thicknesses of corprene was to validate the theory for low attenuation material and for thickness variation. The nitrile coating's main purpose was to attempt to achieve a pressure release boundary condition and secondary purpose was to validate the theory for large attenuation materials.

#### Finite Cylinder Experiment

The finite cylinder is constructed of commercial grade, seamless, 304 stainless steel pipe with an outer radius of 2.0 inches (5.08 cm) and a wall thickness of 0.1875 inches (0.476 cm). The ratio of inner to outer radii is 0.906. The length is 12.75 inches (32.39 cm). The end caps are constructed of 304 stainless steel plate

and are 0.75 inches (1.905 cm) thick. The scattering geometries used are:

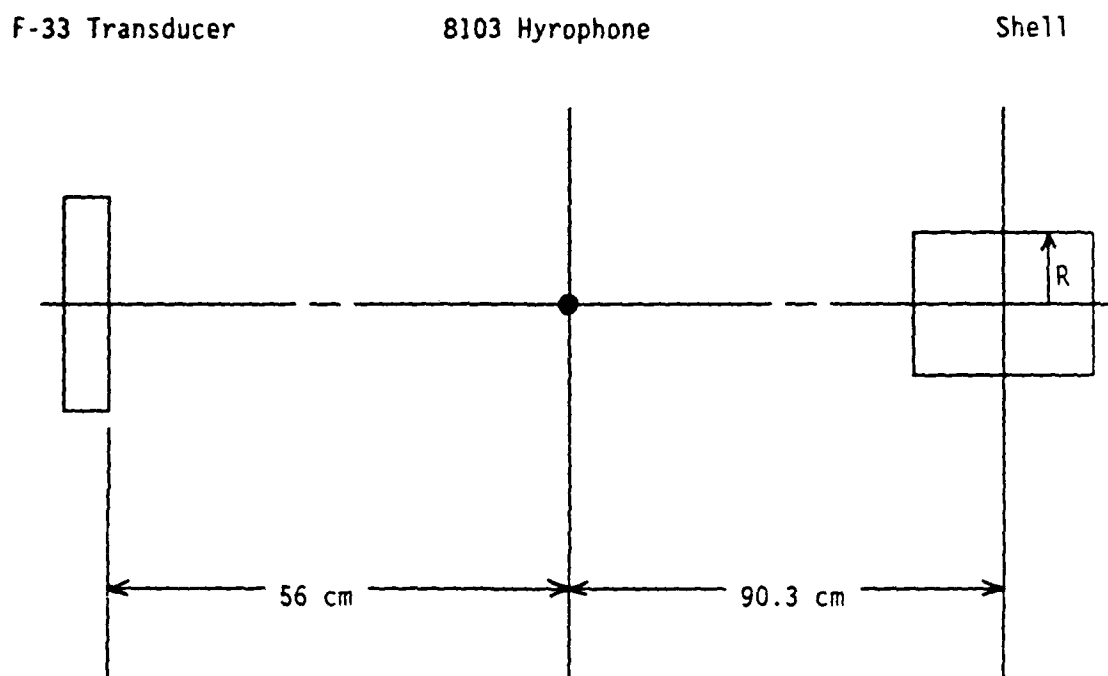
(1) incident wave traveling along the center axis (end on), illustrated in figure 2-5.

(2) incident wave traveling normal to the center axis (side incidence), illustrated in figure 2-6.

This cylinder should scatter in a similar manner to the classical thick shell, i.e. the first antisymmetric and symmetric Lamb modes in addition to other resonance structure should be present.

The purpose of this experiment is to determine if the scattered pressure of the finite thick shell would as a pressure release finite cylinder as determined by the SHIP and CHIEF radiation programs. This requires the characteristic scattering behavior of the stainless steel structure to be eliminated by coating the finite cylinder with a highly attenuating, low acoustic impedance coating. In other words, can the structure be made to "look" pressure released thereby acoustically decoupling the structure by use of the coating.

For each geometry, measurements are taken for the uncoated cylinder and for the cylinder coated with 0.25 inches (0.635 cm) of the closed cell neoprene. The  $ka$  range covered is approximately 1.5 to 15 by using broadband pulses as in the previous experiments. An FFT is taken on the scattered signal and the FFT amplitude is compared to a common reference obtained at the geometric center of the cylinder. Positioning information is not of sufficient accuracy to make the FFT phase information useful. For both geometries, the 8103 hydrophone is located in



$R$  = Radius of finite cylinder (5.08 cm)

Figure 2-5 Finite Cylinder Experimental Setup for Axial Incidence



F-33 Transducer

8103 Hydrophone

Shell

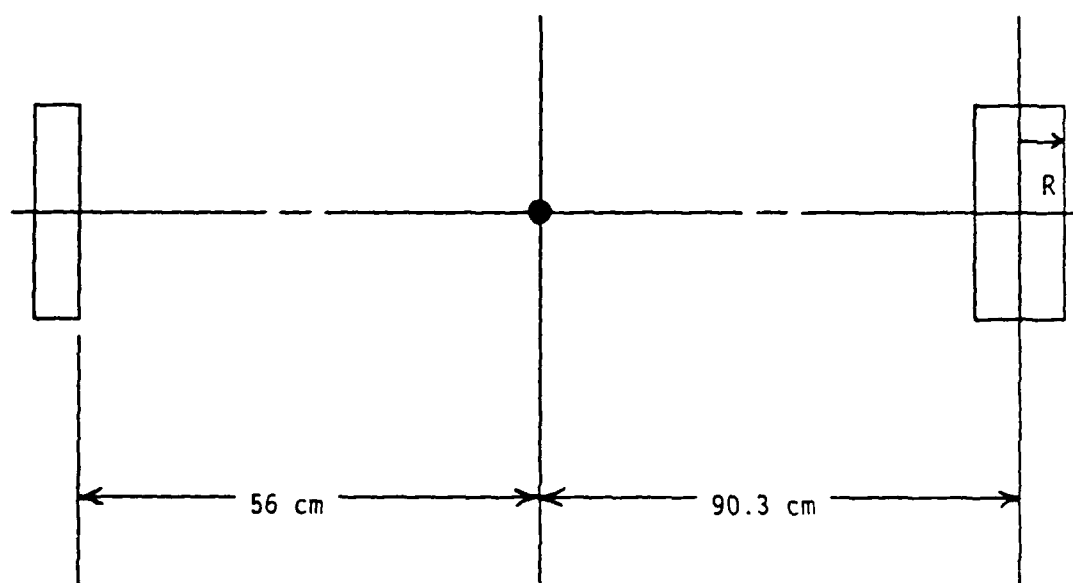
 $R$  = radius of finite cylinder

Figure 2-6 Finite Cylinder Experimental Setup for Normal Incidence

the far field of the target.

Experimental errors arise predominantly from misalignment of the target.

Two possible errors are:

(1) the target is not positioned at exactly the same location relative the reference location.

(2) the target is angularly misaligned so that the incident signal is not exactly normal to the surface of interest.

## CHAPTER III

### Experimental Results and Discussion

#### Viscoelastic Moduli Determination

For the Young's modulus and plane wave modulus determinations, the measured quantities are the phase speed,  $C_p$ , and attenuation,  $\alpha$ . These two quantities combine to give the wave number of the particular wave, either extensional or longitudinal wave, generated.

$$k = \frac{\omega}{C_p} + i\alpha \quad (3-1)$$

The attenuation is determined in units of nepers/cm and converted to dB/cm (by multiplying by the conversion factor of 8.6859). The respective viscoelastic constant (complex quantity) is determined from the complex wave number by

$$M = \frac{\rho \omega^2}{k_m^2} \quad (3-2)$$

The measurements were not performed on numerous samples or lot numbers so direct application of these results to other samples is cautioned. Accuracy of the

results is difficult to estimate. However, the data spread obtained for different center frequency groups provides a reasonable measure of the accuracy. The Kramers-Kronig relation, linking the attenuation with dispersion (frequency dependence of the phase speed), is utilized as a check of the data for a particular measurement sequence. O'Donnell, et al.<sup>115</sup>, derives the local Kramers-Kronig relation for linear acoustic systems:

$$\alpha = \frac{\pi^2 f^2}{C_0^2} \frac{dC_p}{df} \quad (3-3)$$

where  $f$  is the frequency,  $C_0$  is the phase speed, and  $dC_p/df$  is the experimentally measured local slope from the phase speed verses frequency curve at  $C_0$ . The densities of the materials are tabulated in table 3-1.

Table 3-1

Density of Materials

<u>Material</u>	<u>Density (grams/cc)</u>
closed cell neoprene	0.224
closed cell nitrile	0.248
corprene	0.720
cork-nitrile	0.670

The closed cell neoprene data is shown in figures 3-1 through 3-4.

The extensional data becomes unusable at frequencies greater than 3500 Hz. The maximum spread of data for the extensional speed measurements was 10% and for the extensional attenuation measurements was less than .5 dB/cm. The maximum spread of data for the plane wave speed measurements was 5% and for the plane wave attenuation measurements was less than 1.0 dB/cm. The extensional attenuation predicted by the Kramers-Kronig relation using the experimentally determined phase speed - frequency curve is within 7.5% of the experimentally measured attenuation. The plane wave attenuation predicted by the Kramers-Kronig relation is within 3% of the measured attenuation. Extrapolation of the extensional data to higher frequencies indicates that the Poisson's ratio is slightly greater than 0. Microscopic inspection of a cross section of the material indicated the material should be isotropic.

The closed cell nitrile data is shown in figures 3-5 through 3-8. The attenuation is too large to allow accurate measurement of extensional data at frequencies greater than 3500 Hz. The maximum spread of data for the extensional speed measurements was 5% and for the extensional attenuation measurements, the maximum spread of data was less than .5 dB/cm. The maximum spread of data for the plane wave speed measurements was 4% and for the plane wave attenuation measurements was 1.0 dB/cm. The extensional attenuation predicted by the Kramers-Kronig relation is within 3.7% of the experimentally measured attenuation. The plane wave attenuation predicted by the Kramers-Kronig rela-

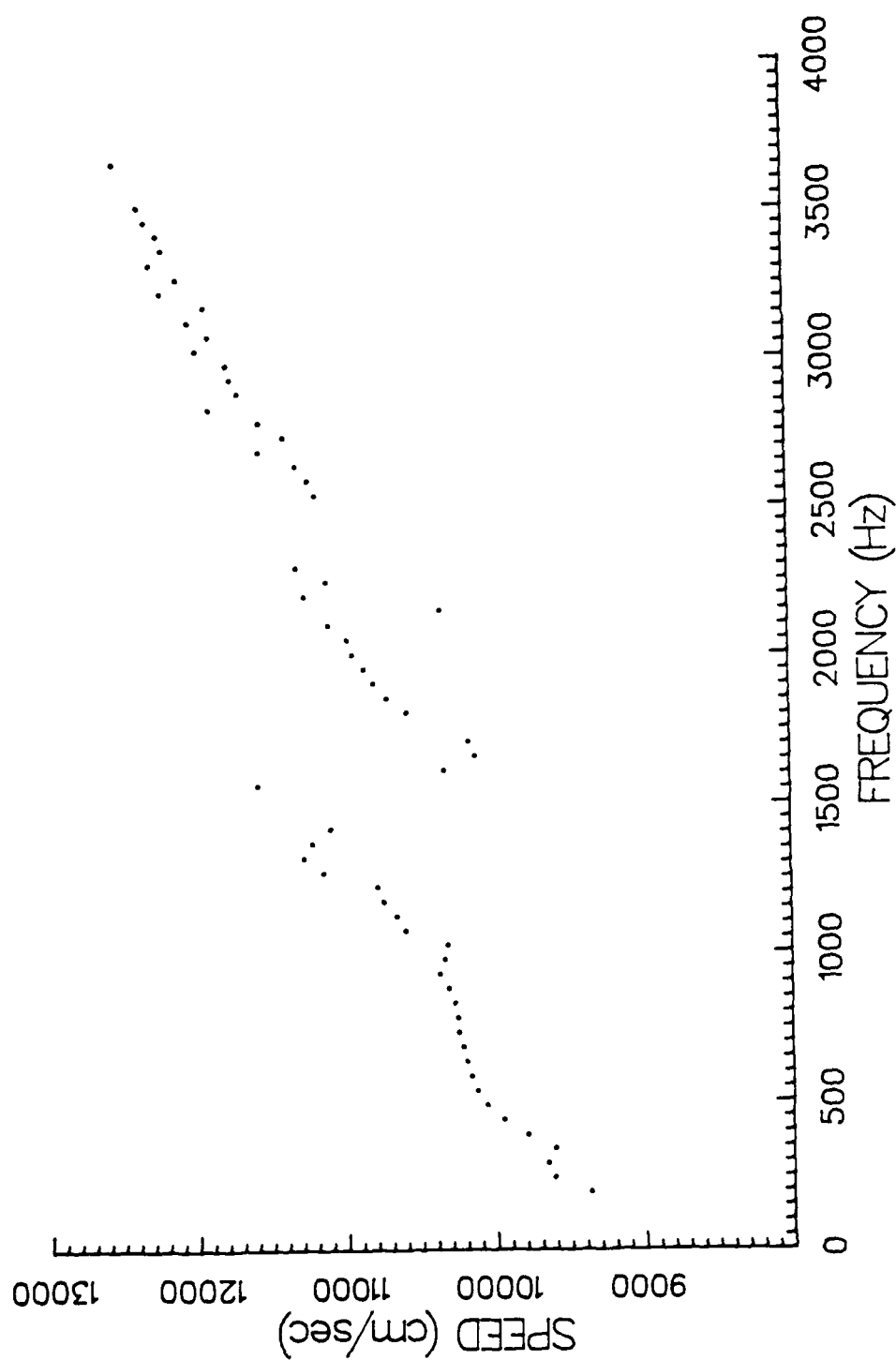


Figure 3-1 Neoprene Extensional Speed versus Frequency

# NEOPRENE EXTENSIONAL ATTENUATION

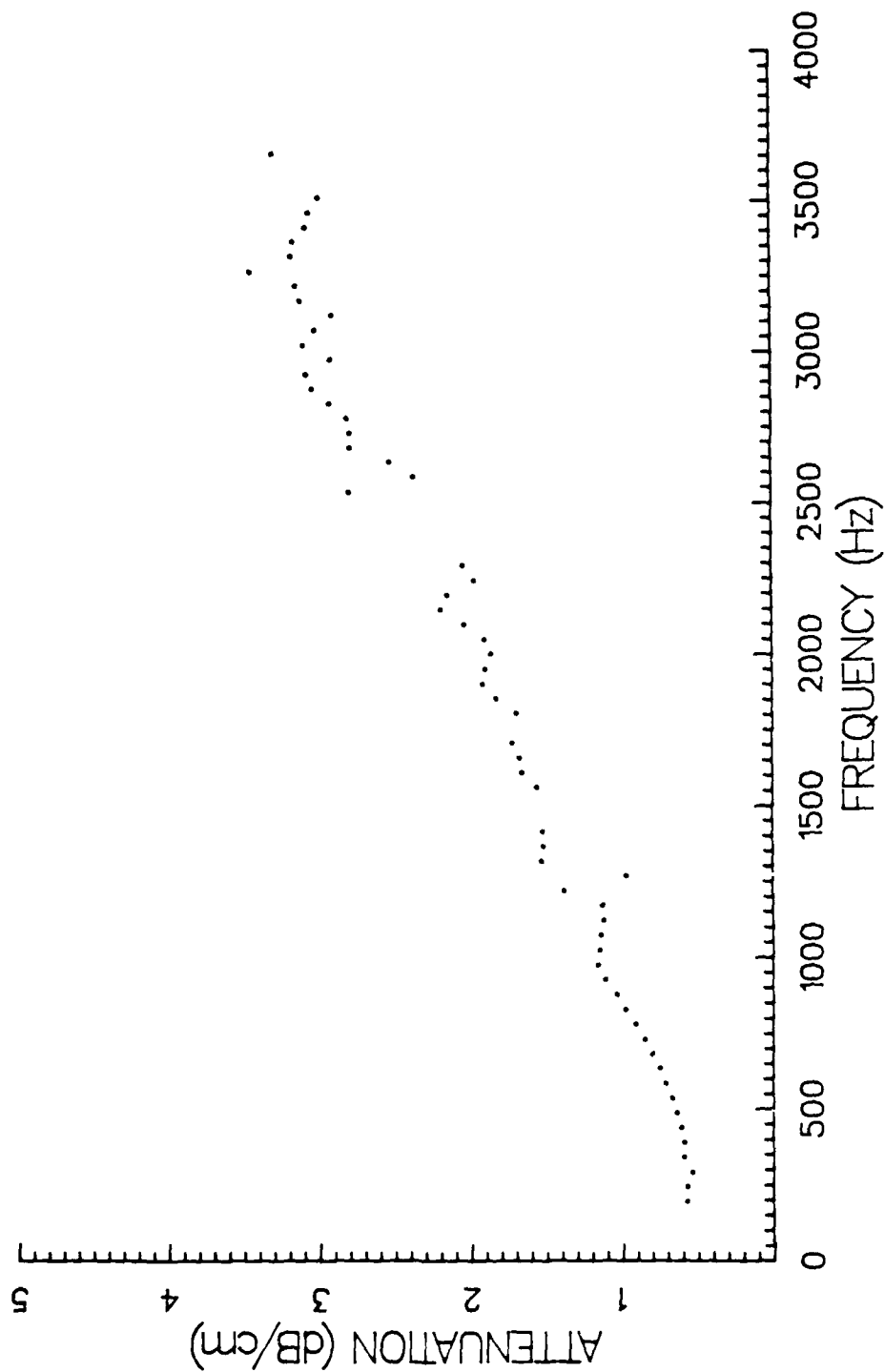


Figure 3-2 Neoprene Extensional Attenuation versus Frequency

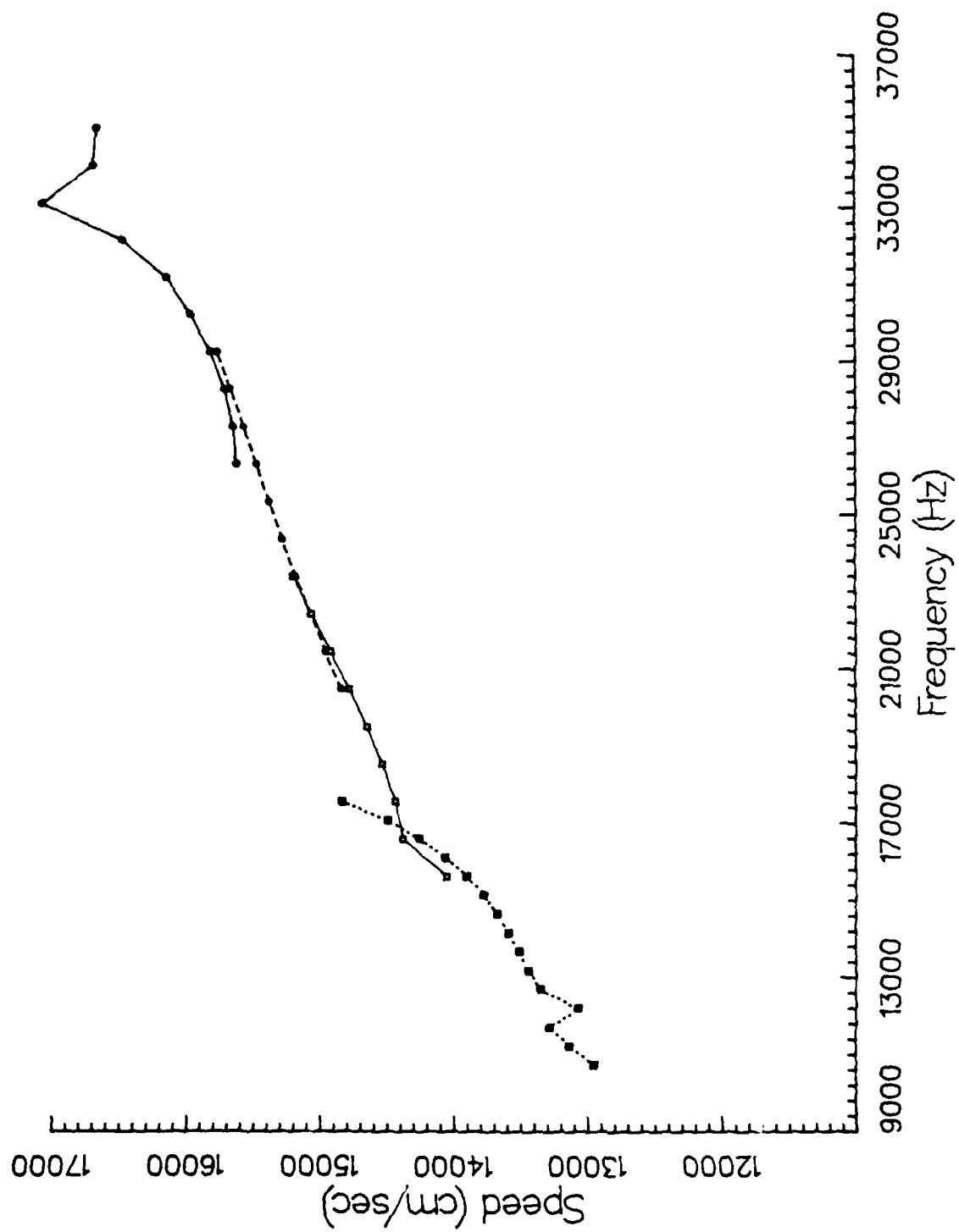


Figure 3-3 Neoprene Plane Wave Speed versus Frequency



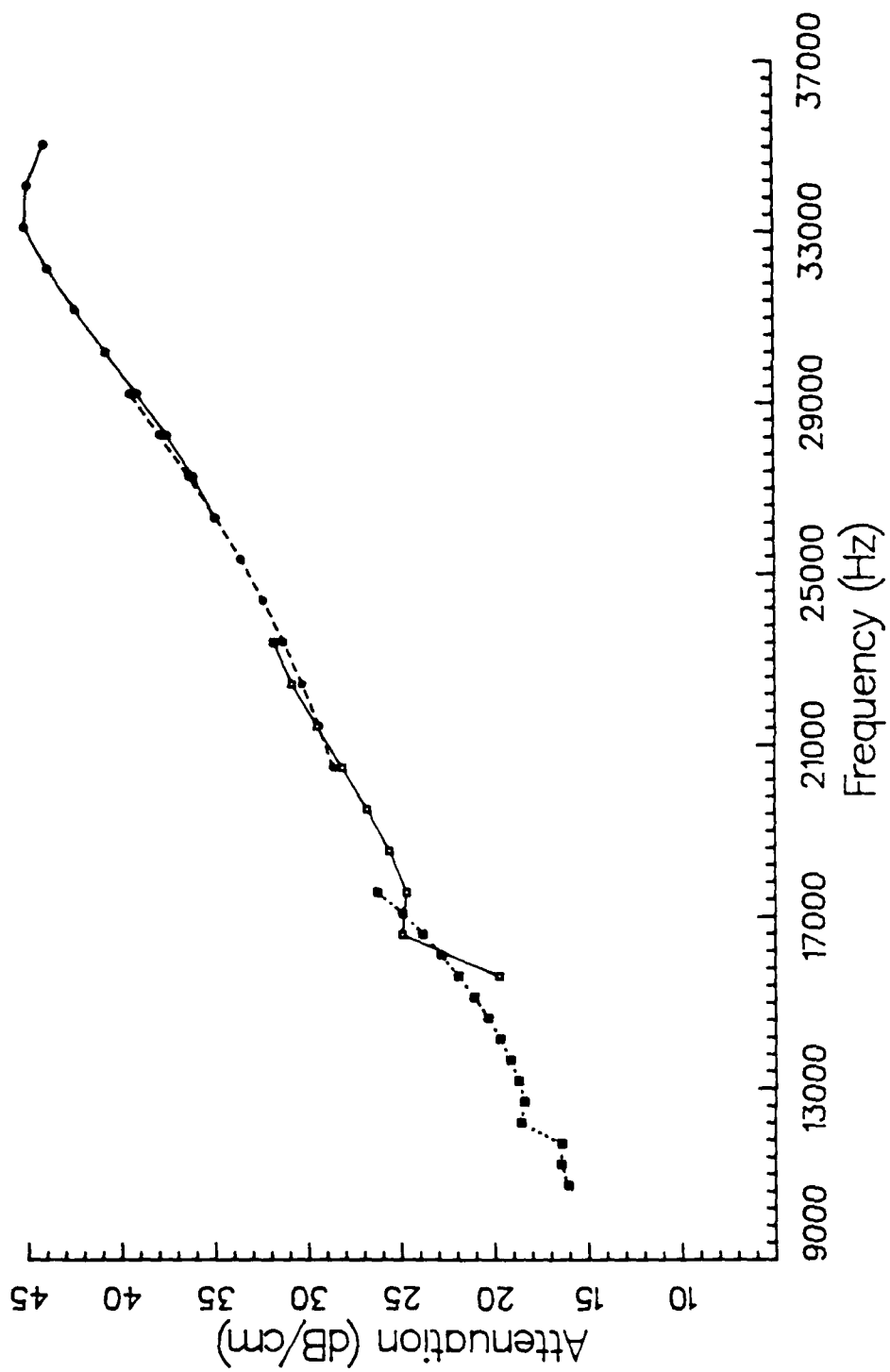


Figure 3-4 Neoprene Plane Wave Attenuation versus Frequency

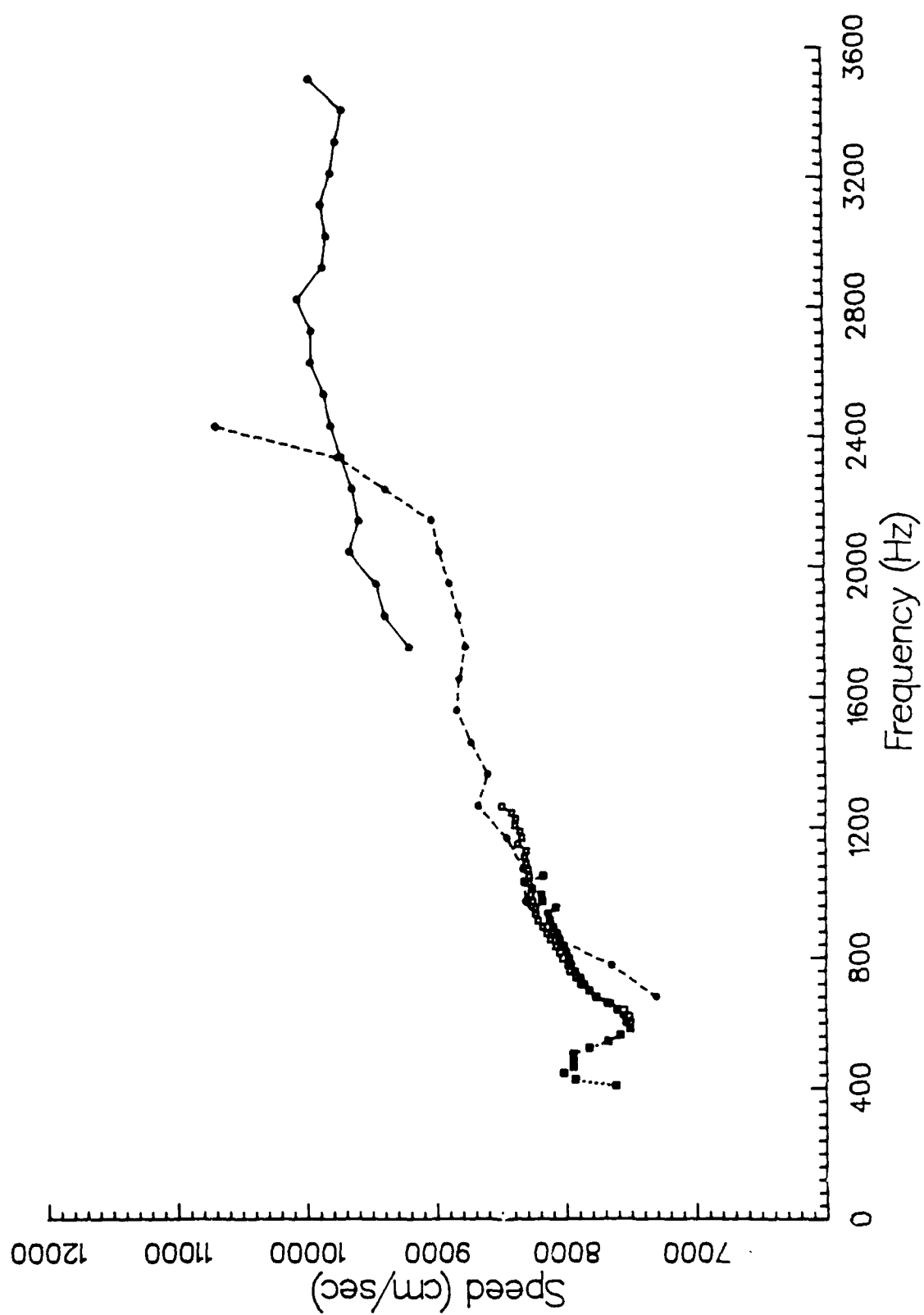


Figure 3-5 Nitrile Extensional Speed versus Frequency

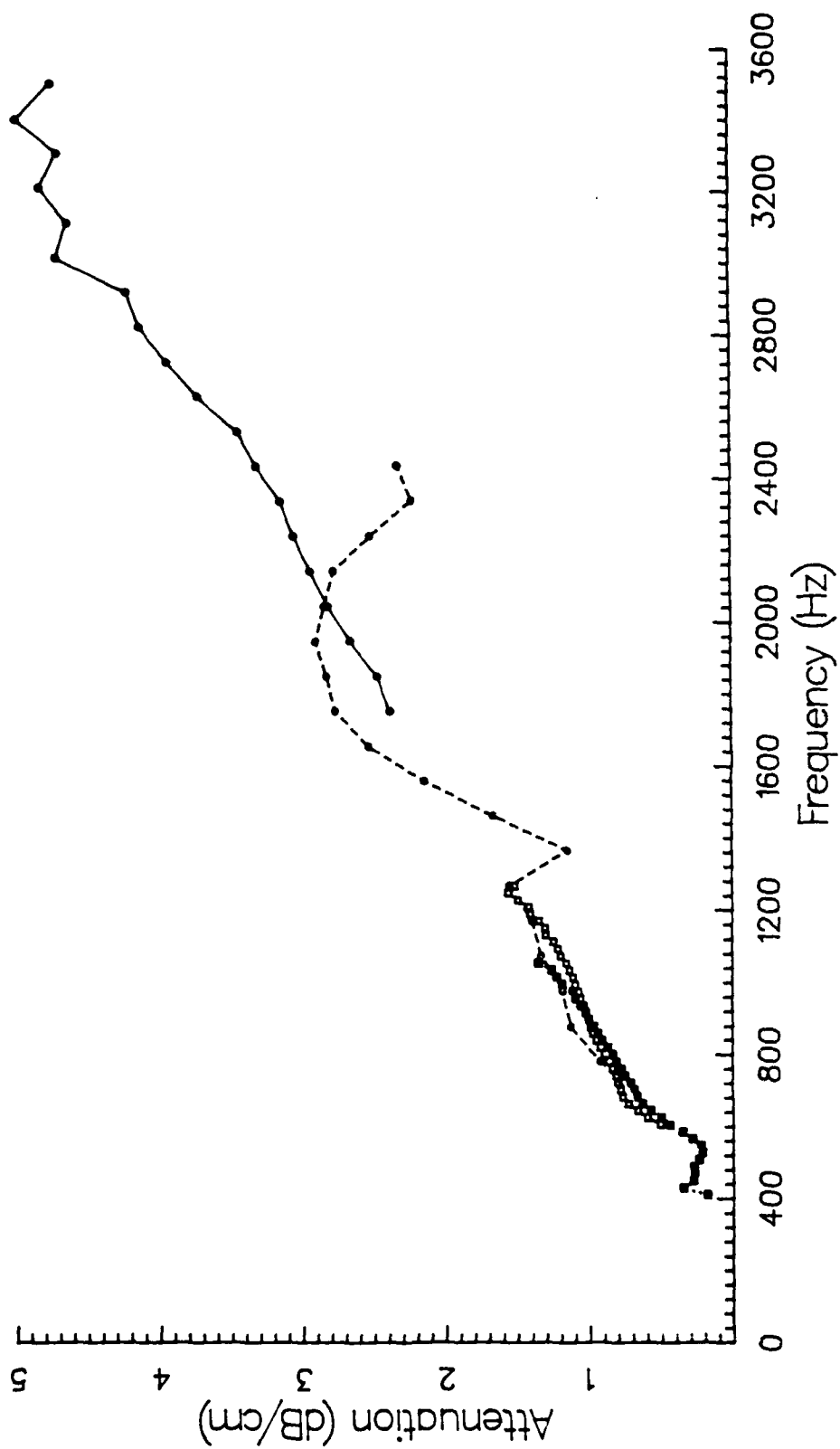


Figure 3-6 Nitrile Extensional Attenuation versus Frequency

NITRILE PLANE

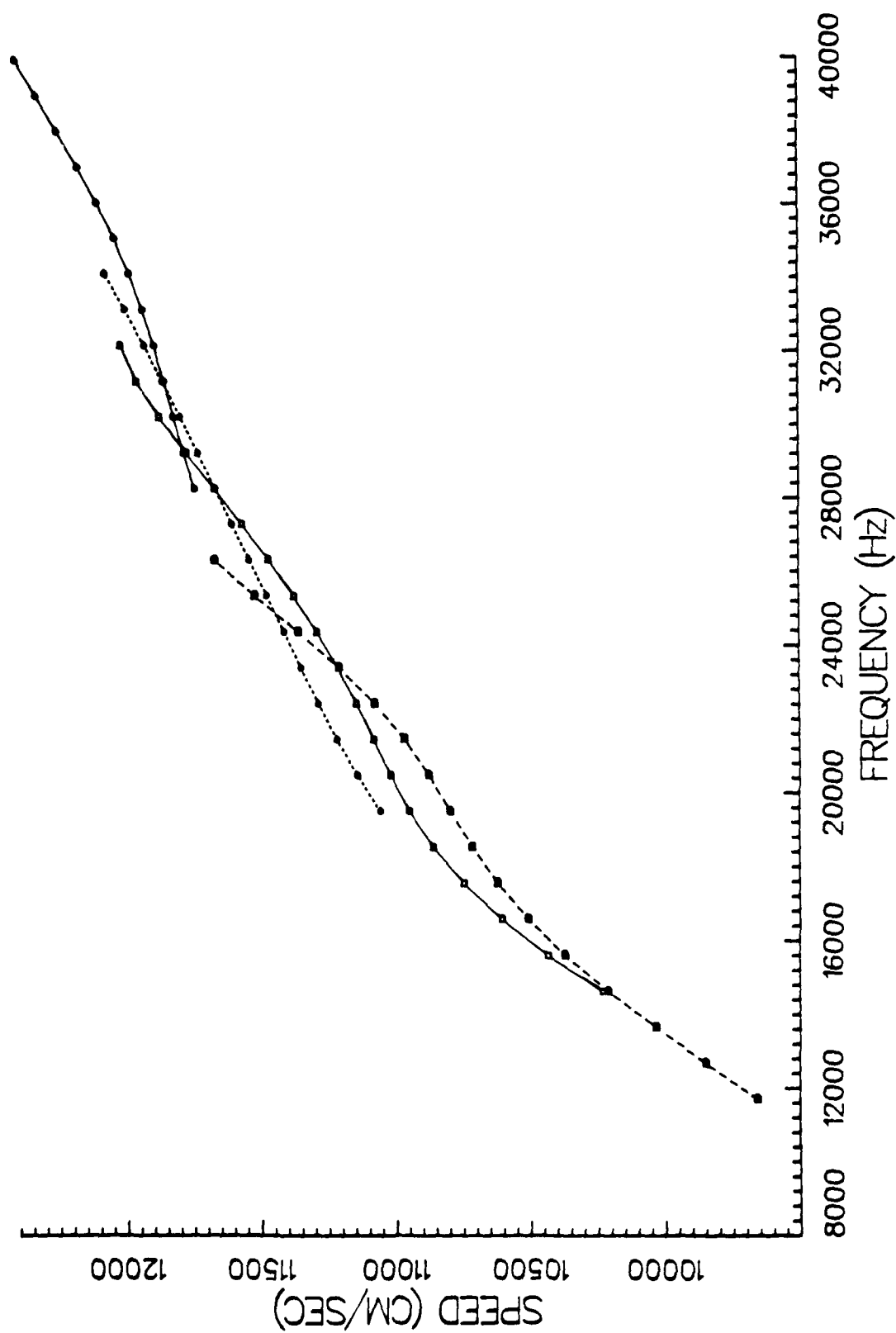


Figure 3-7 Nitrile Plane Wave Speed versus Frequency

# NITRILE PLANE WAVE ATTENUATION

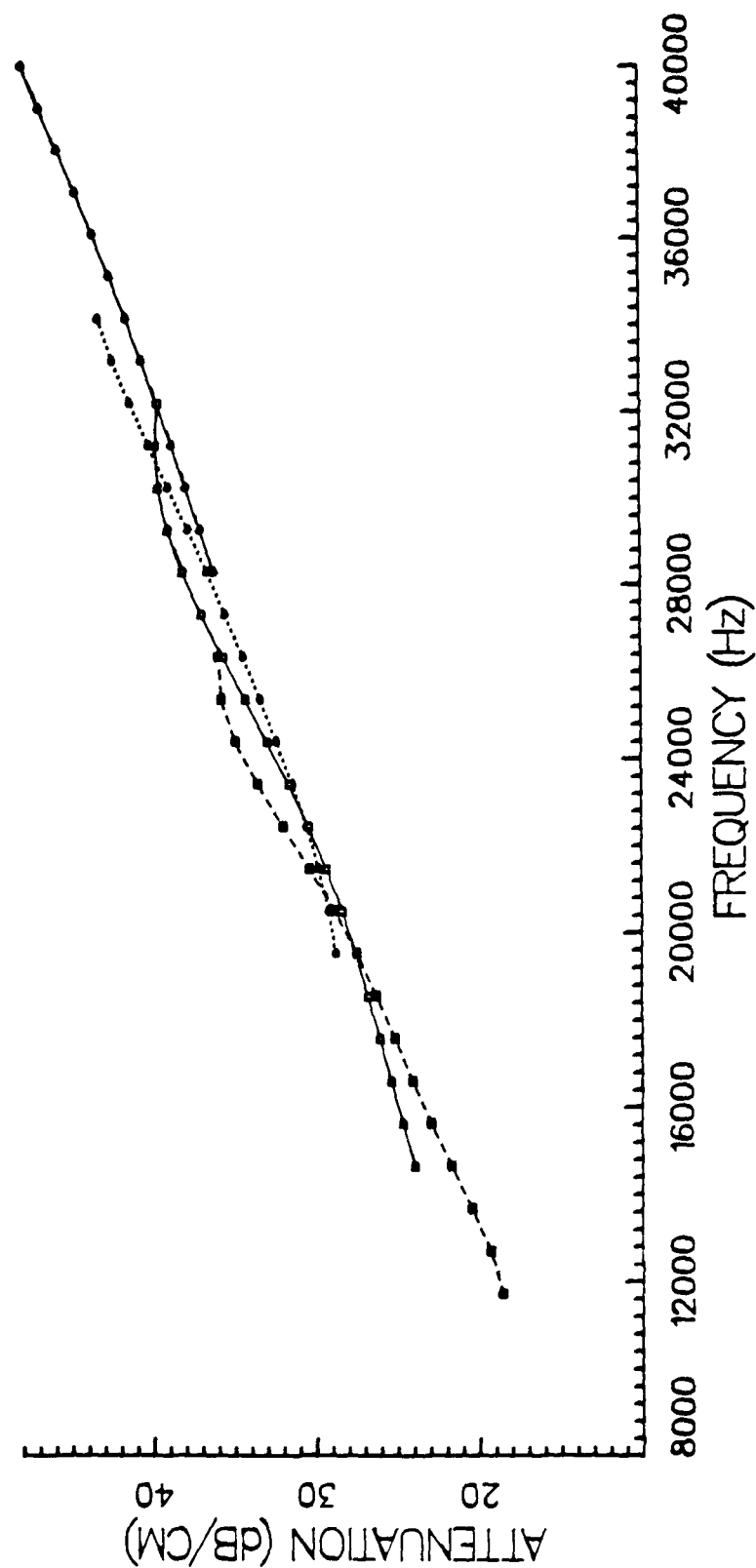


Figure 3-8 Nitrile Plane Wave Attenuation versus Frequency

tion is within 1% of the measured attenuation. Extrapolation of the extensional data to higher frequencies indicates that the Poisson's ratio is between 0 and 0.2. Microscopic inspection of a cross section of the a .25 inch thick material indicates the material is isotropic. Microscopic inspection of the 1/16 inch thick nitrile reveals a very different air bubble structure than is present in the .25 inch nitrile. The thicker nitrile consists of relatively small, uniformly dispersed air bubbles throughout the matrix whereas the 1/16 inch nitrile has the same small bubble consistency but with the additional presence of the very large bubbles randomly dispersed throughout the matrix. It is very questionable if the measurements for the .25 inch thickness apply to the thinner material.

The corprene data is shown in figures 3-9 through 3-12. The extensional attenuation is too large at frequencies greater than 5000 Hz. to allow accurate measurement. The maximum spread of data for the extensional speed measurements was 3% and for the extensional attenuation measurements was 0.7 dB/cm. The maximum spread of data for the plane wave speed measurements was 1.5% and for the plane wave attenuation measurements was less than 0.3 dB/cm. The extensional attenuation predicted by the Kramers-Kronig relation is within 25% of the experimentally measured attenuation. The Kramers-Kronig relation is not easily applied to the plane wave data since the slope of the phase speed-frequency curve is small and not obvious. Small variations in the slope result in differences of 50% of the predicted attenuation. As a check of the data, the FFT analysis was performed on the early portion of the transmitted waveforms where

## CORPRENE EXTENSIONAL SPEED

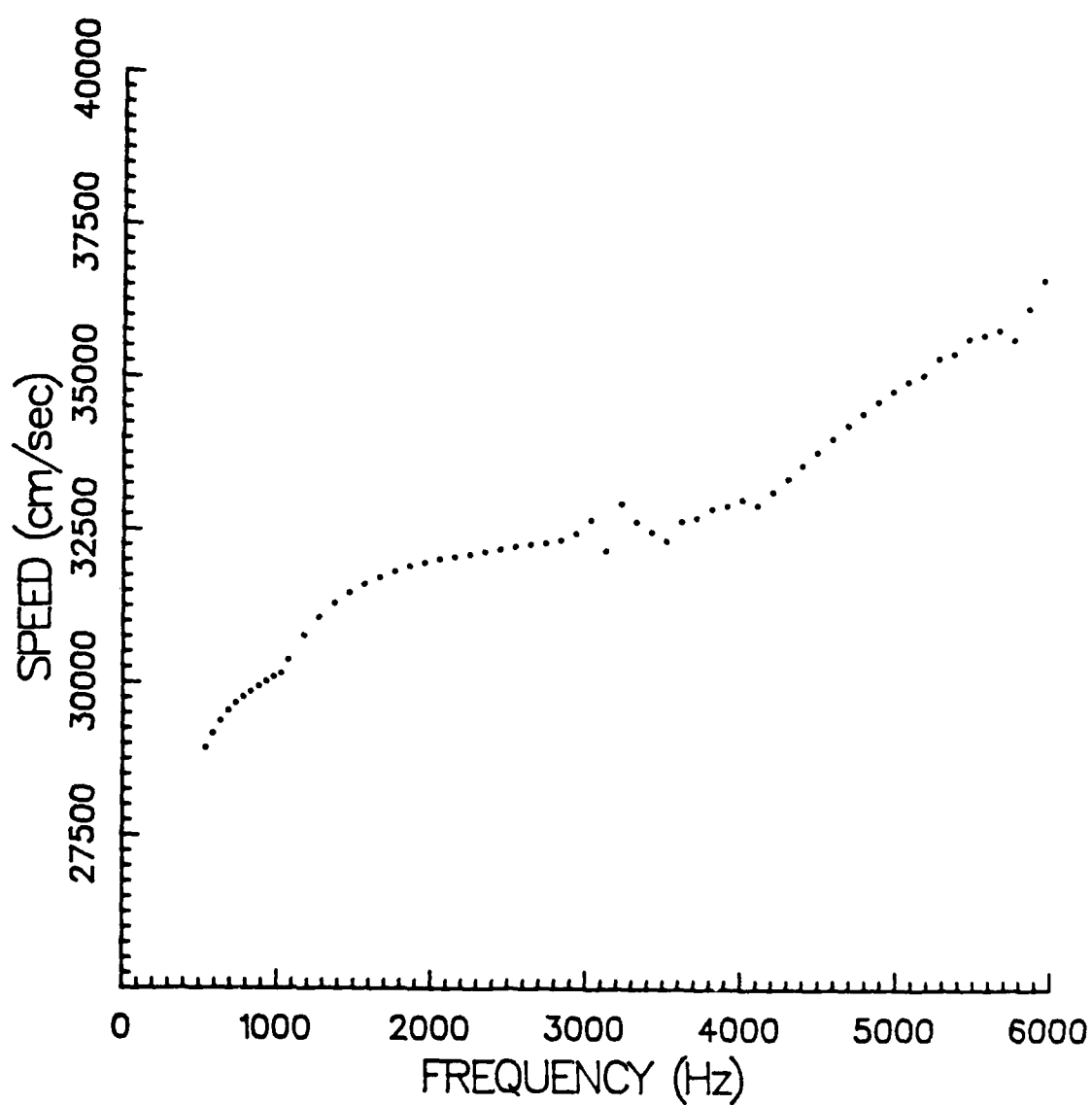


Figure 3-9 Corprene Extensional Speed versus Frequency

## CORPRENE EXTENSIONAL ATTENUATION

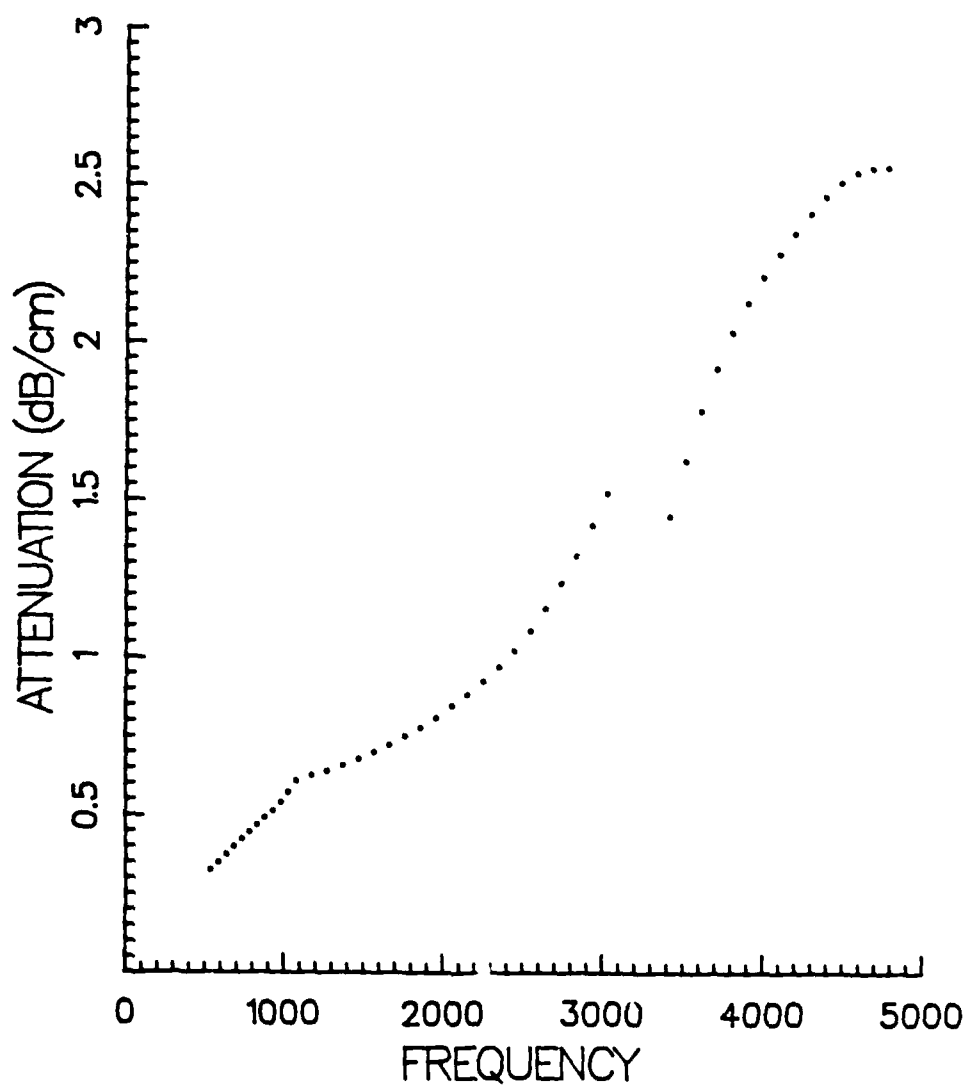


Figure 3-10 Corprene Extensional Attenuation versus Frequency



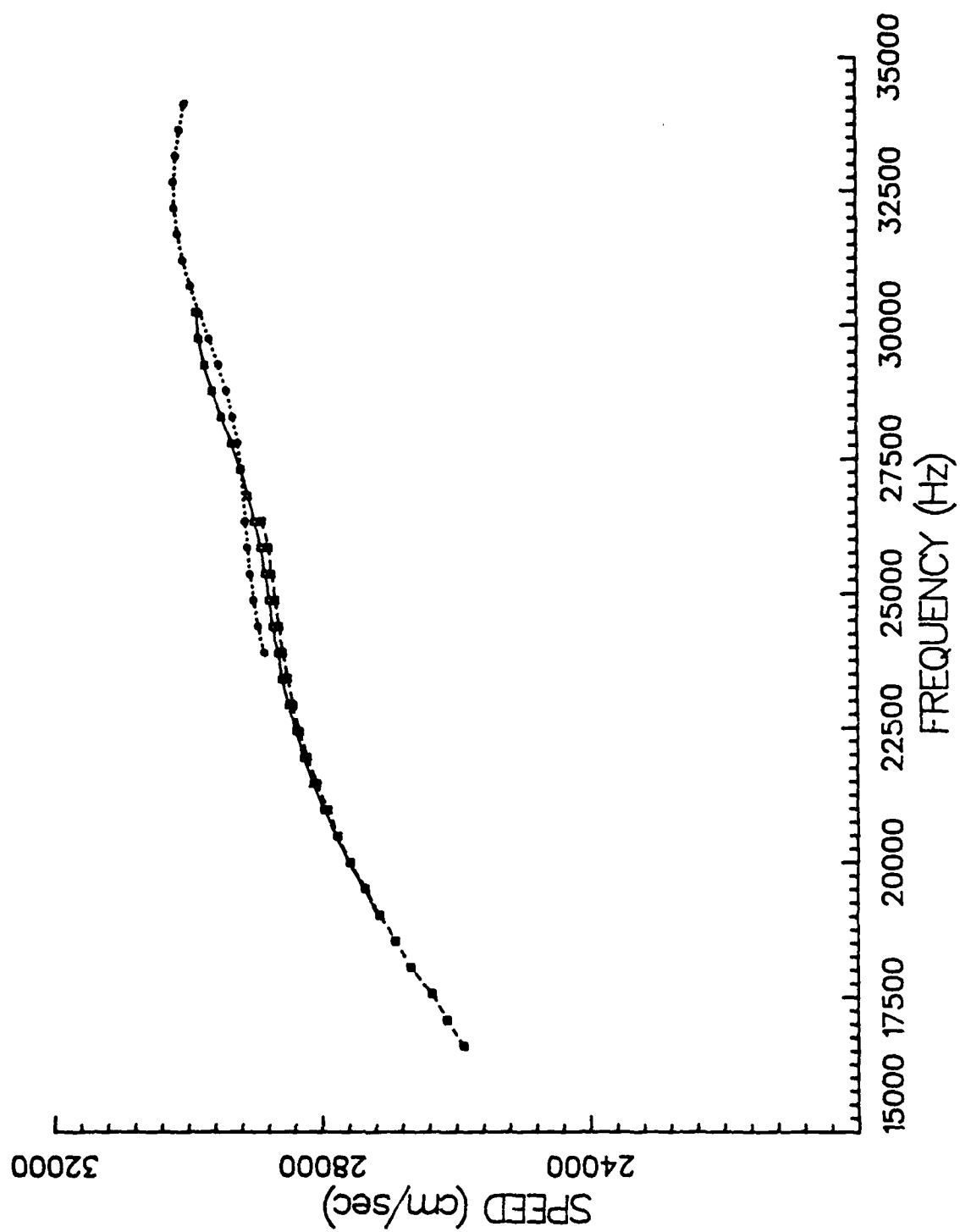


Figure 3-11 Corprene Plane Wave Speed versus Frequency

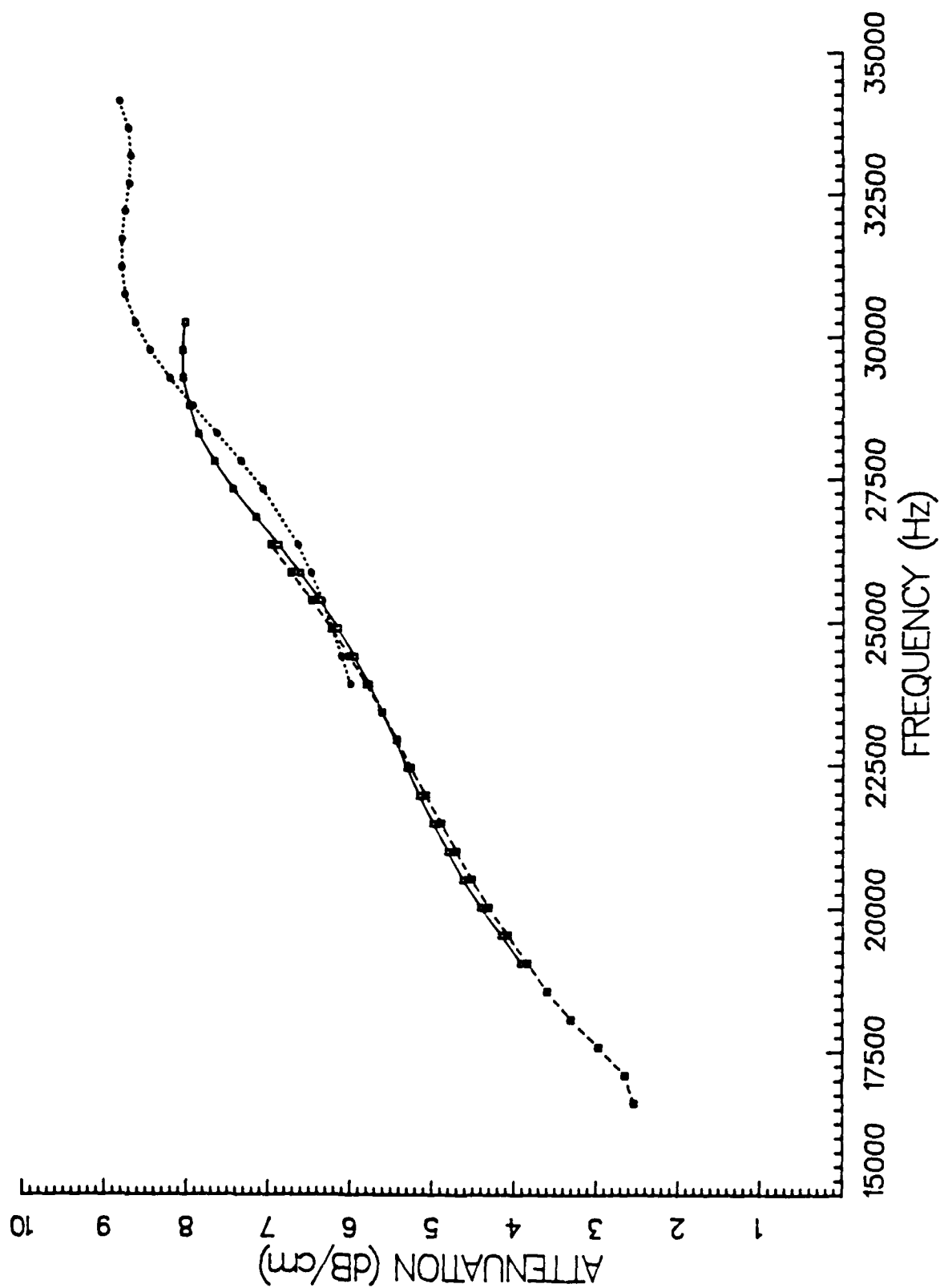


Figure 3-12 Corprene Plane Wave Attenuation versus Frequency

the length of the waveform was selected so as to prevent any multiple internal reflections from interfering. The above analysis of the shortened waveform was in excellent agreement with the analysis of the complete waveform which accounted for multiple internal reflections. Horsley and Thompson<sup>116</sup> report the longitudinal speed of corprene (manufactured by Armstrong Rubber Company) to be  $3.0 \times 10^5$  cm/sec at 10 kHz as determined by impedance tube measurements. Although these two materials are not produced by the same manufacturer, they do have the same military specification (mil spec). The extensional phase speed is significantly greater than the longitudinal phase speed for comparable frequencies (well beyond any possible experimental error) which indicated the Young's modulus is larger than the plane wave modulus. The moduli are related by Poisson's ratio as follows

$$M = \frac{E (1 - \nu)}{(1 + \nu)(1 - 2\nu)} \quad (3-4)$$

For any positive value of Poisson's ratio, the plane wave modulus is always greater than the Young's modulus and they are equal at a Poisson's ratio of 0. The conclusion is that the material is slightly anisotropic. Microscopic inspection of the longitudinal wave path and the extensional wave path shows a preferential alignment of the cork particles so that the thinner portion of the cork particle is aligned in the extensional wave propagation direction. This particle alignment mostlikely occurred during the rolling phase of fabrication. Since the plane wave

data is directly applicable to the frequency range of interest, a Poisson's ratio of 0 is assumed and the Young's modulus is set equal to the plane wave modulus. The shear modulus, which is required for the viscoelastic layer program, is determined from

$$G = \frac{E}{2} \quad (3-5)$$

The validity of this assumption will be determined when the actual scattering measurements are compared with theoretical calculations for a Poisson's ratio of 0 and 0.4.

The cork-nitrile data is shown in figures 3-13 through 3-16. The extensional attenuation is too large at frequencies greater than 5000 Hz. to allow accurate measurement. The maximum spread of data for the extensional speed measurements was 3% and the maximum spread of data for the extensional attenuation measurements was 0.2 dB/cm. The maximum spread of data for the plane wave speed measurements was 8.3% and for the plane wave attenuation measurements was less than 1.5 dB/cm. The extensional attenuation predicted by the Kramers-Kronig relation does not agree with the experimentally measured attenuation. The experimental attenuation was verified by direct calculation from the waveforms. The plane wave attenuation predicted by the Kramers-Kronig relation is within 25% the experimentally measured attenuation. The larger than expected variations in the plane wave measurements appear to be the result of in-

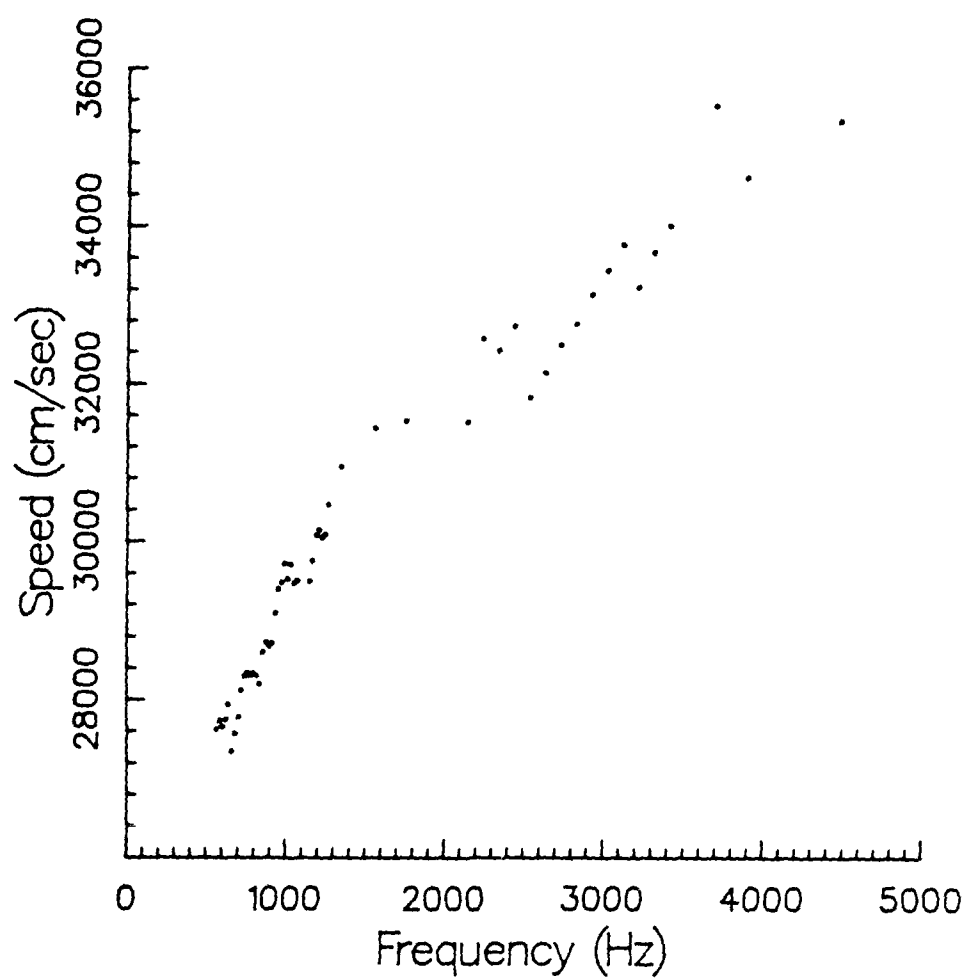


Figure 3-13 Cork-Nitrile Extensional Speed versus Frequency

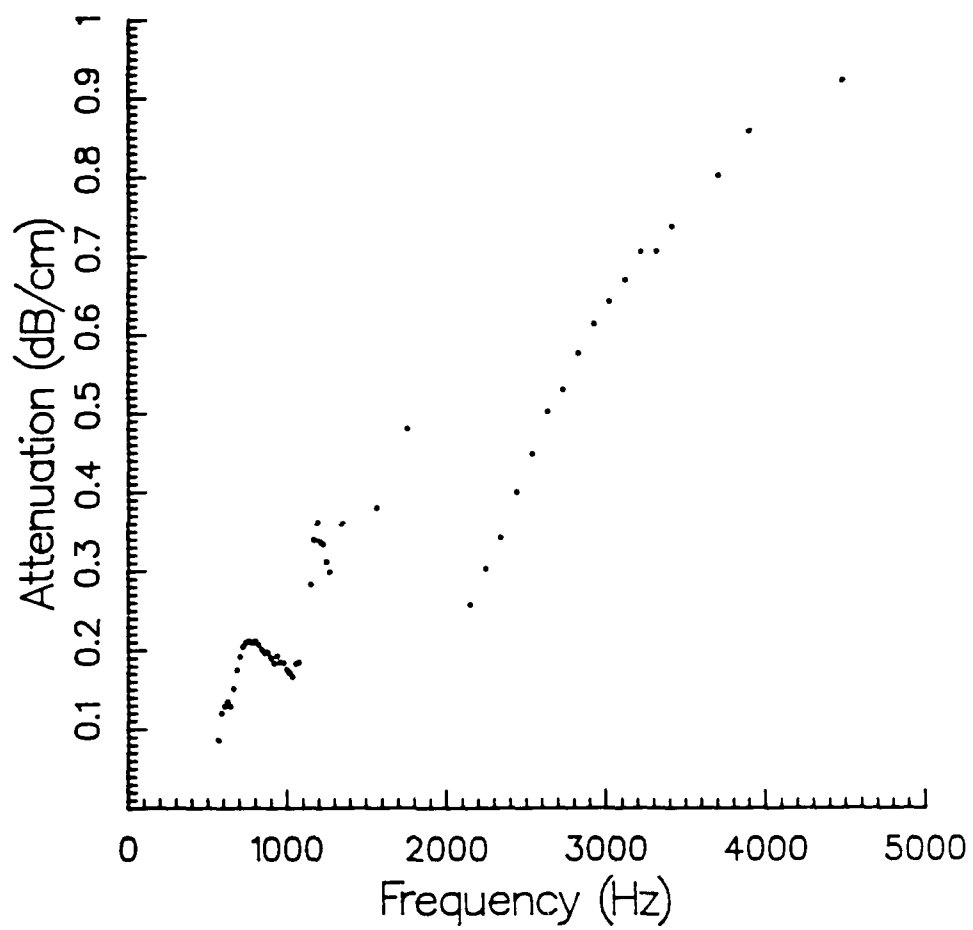


Figure 3-14 Cork-Nitrile Extensional Attenuation versus Frequency

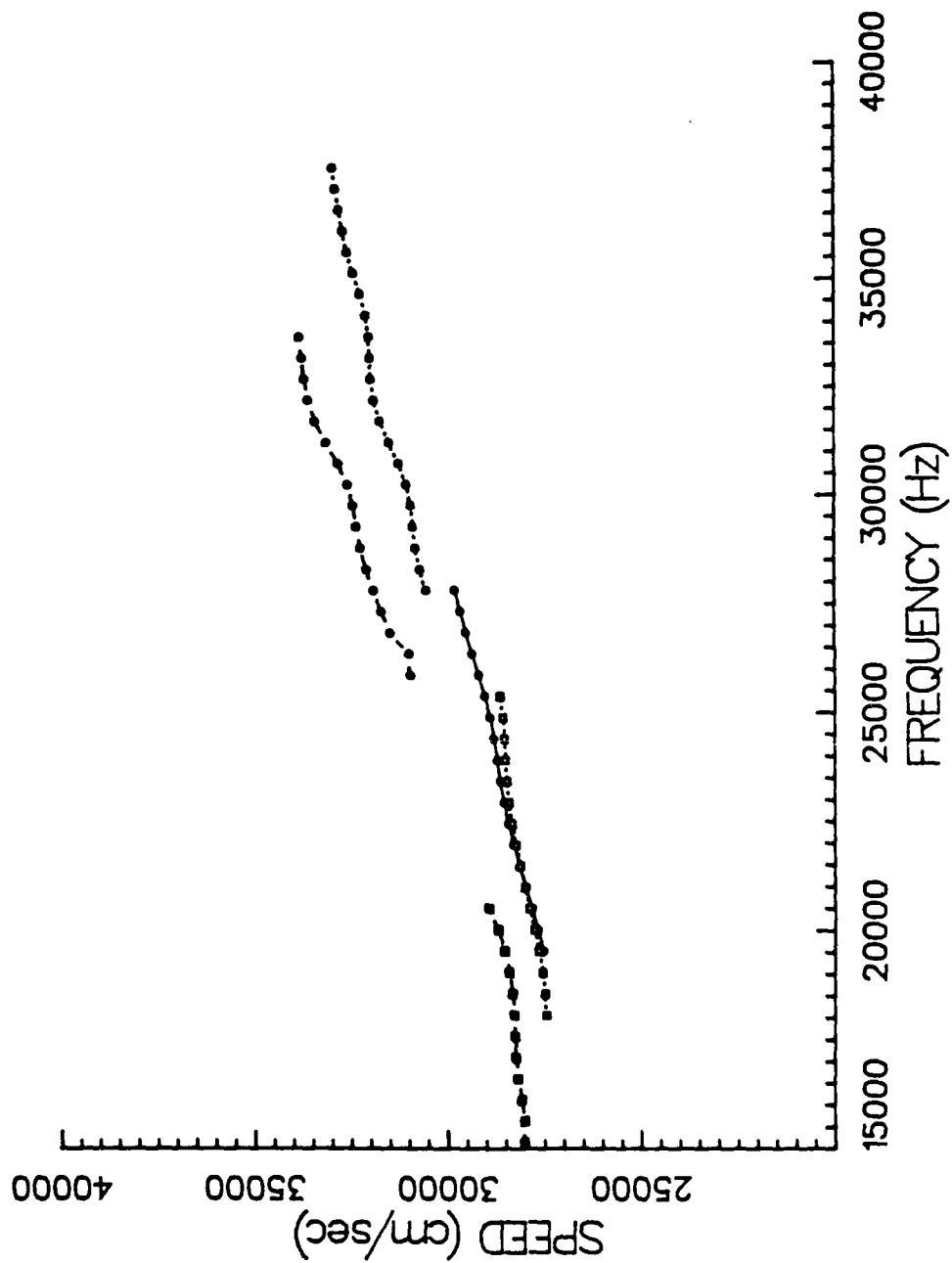


Figure 3-15 Cork-Nitrile Plane Wave Speed versus Frequency

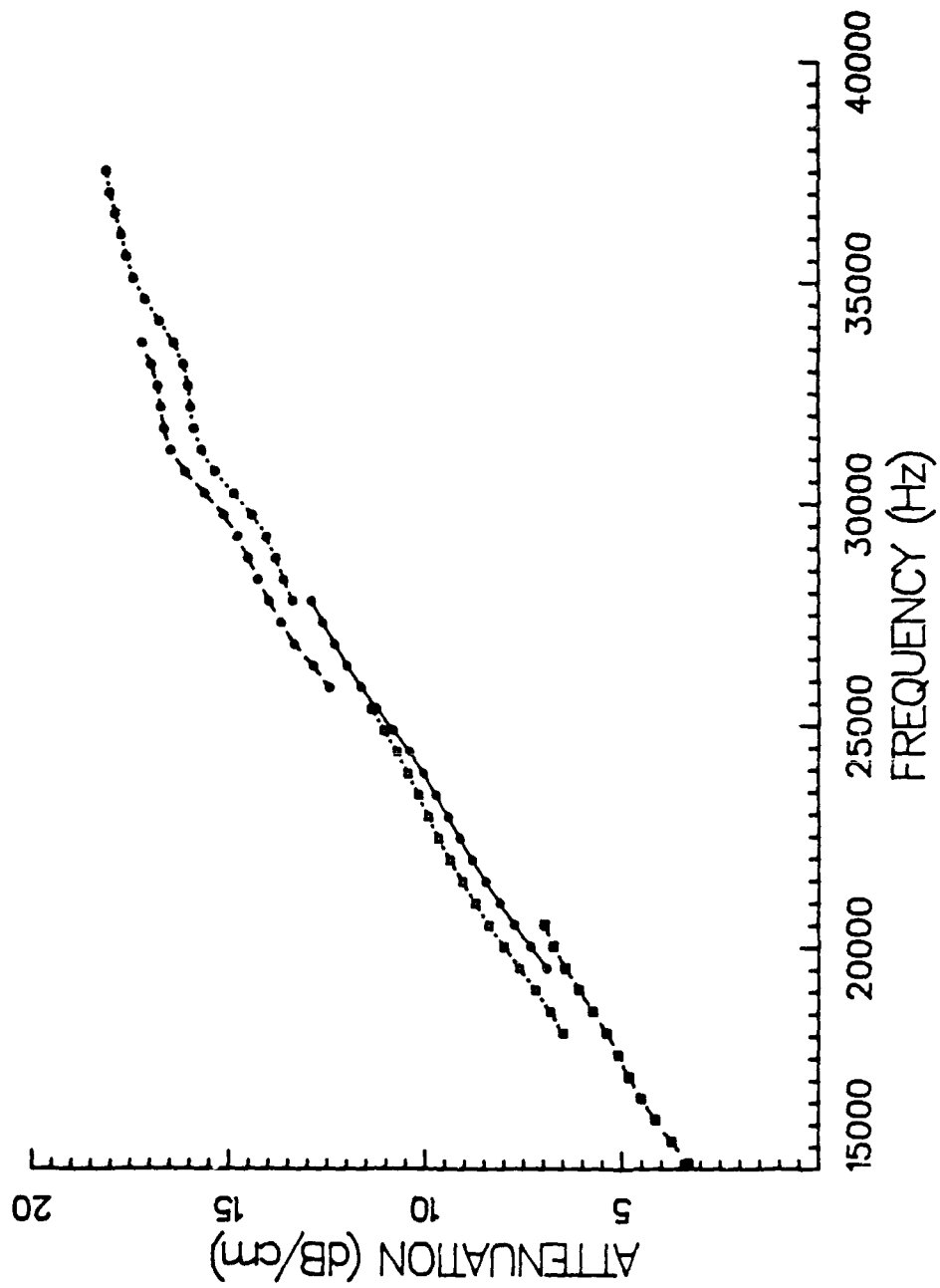


Figure 3-16 Cork-Nitrile Plane Wave Attenuation versus Frequency



strument malfunction. The waveforms were recorded by a digital waveform recorder which appears to have had a slight oscillation in the trigger delay function. This would insert a constant phase shift error for a particular center frequency group causing the phase speed and attenuation results to be slightly shifted relative to other center frequency groups. Review of the extensional phase speed and longitudinal phase speed shows the same anisotropic behavior as the corprene. Microscopic inspection of the cork-nitrile shows a preferential alignment of the cork particles in the extensional wave propagation direction.

To summarize our experiences with the measurement methods employed: 1. The panel measurements consistently provided excellent result with proper overlap between individual center frequency groups (with one exception attributed to instrument malfunction). 2. The Young's modulus method, although appearing simple, was in reality a difficult measurement to obtain reasonable data from for two reasons: (1) the closed cell rubbers were highly attenuating, which required locating the data samples too close together, which introduced large percentage errors in the distance measurement between data collection locations. (2) the Poisson's ratios for all of the sample materials was unexpectedly low which reduced the amplitude of the displacement recorded by the phonograph needle making the signals susceptible to noise. It appears the Kramers-Kronig relation agrees well with experimental data for isotropic materials but not so well for slightly anisotropic materials.

### Scattering From the Simulated Infinite Cylinder

Scattering measurements for the uncoated cylindrical shell were the first measurements performed. The frequency range covered by these measurements was 5 kHz to 65 kHz. This experiment served as a check of the experimental method since similar measurements are well documented. The scattered signal for all  $ka$  values was inverted relative to the incident signal. The plot of the experimentally determined form function versus  $ka$ , where  $k$  is the wave number in water and  $a$  is the outer radius of the shell, is plotted in figure 3-17. The different point markers and connecting lines indicate different center frequency groups of the incident signal. The theoretical calculation of the form function is plotted as the solid line superimposed over the experimental data. The agreement between the experimental data and the theory is generally excellent. Agreement is poor in the region between  $ka$  values of 1 and 2 due to an unexplained resonance present in the experimental data at a  $ka$  equal to 1.5. There should not be any resonances in this  $ka$  region hence some undetermined experimental factor must be involved. Measurements in this  $ka$  region (frequencies of 10 kHz and less) are potentially suspect due to the physical size of the measurement tank which makes the separation of the scattered signal from the multiple background echos progressively more difficult at low frequencies. Both curves indicate the presence of the first symmetric Lamb mode which causes the first sharp dip in the form

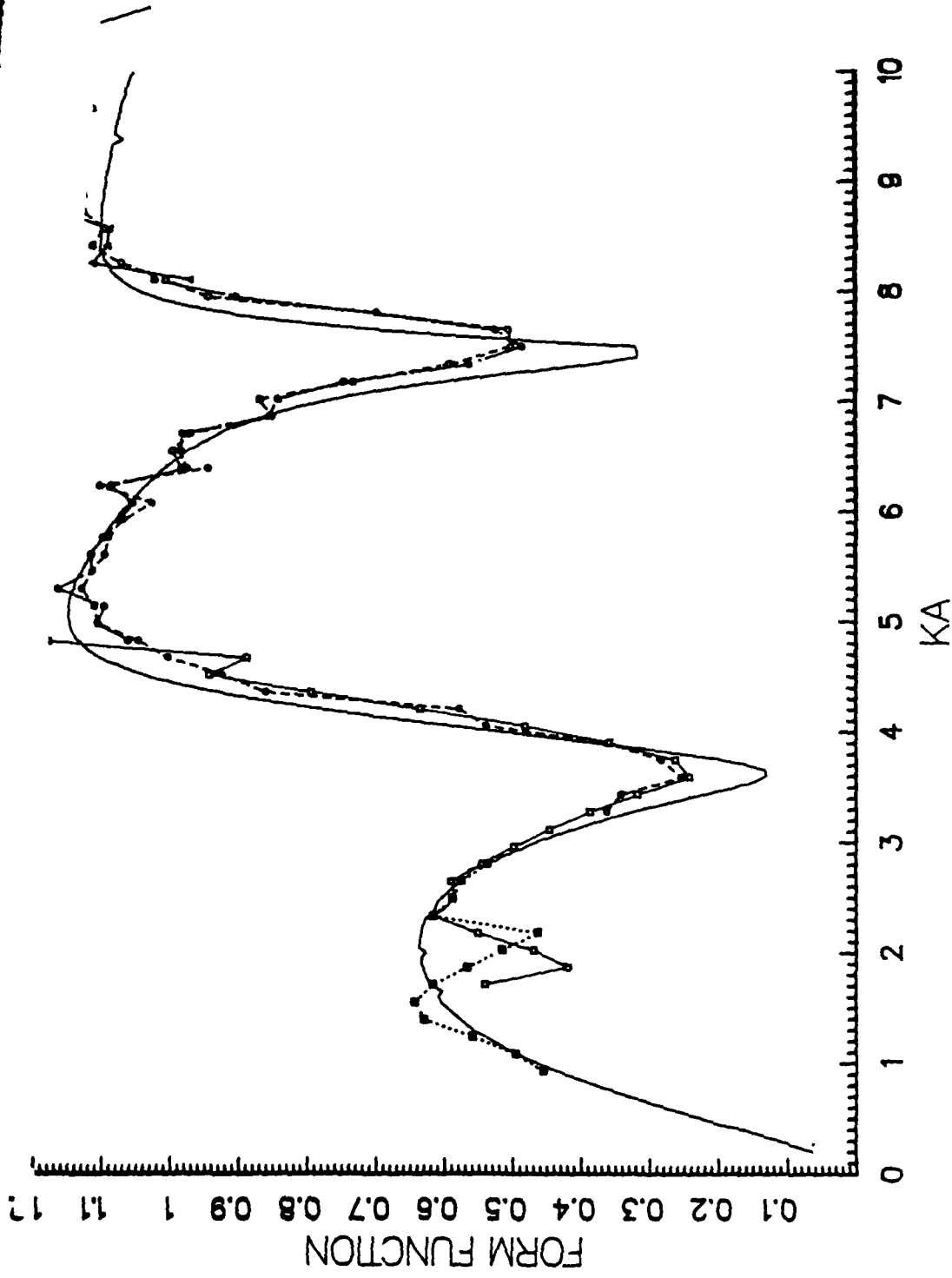


Figure 3-17 Uncoated Thin Shell Backscatter Form Function ( $b/a = .97$ )

function at a  $ka$  of 3.7. The second circumnavigation of this wave is observed at a  $ka$  of 7.45 resulting in a  $\Delta ka$  of 3.75. The theoretical calculations assume a Young's modulus of  $2.2 \times 10^{12}$  dynes/cm<sup>2</sup>. The first resonance dip occurs when the wavelength of the first symmetric Lamb mode is equal to the circumference of the shell. The corresponding value of  $ka$  that the resonance dip occurs at is determined below.

$$v_{s,p} = \sqrt{\frac{E}{\rho(1 - \nu^2)}} = 5.53 \times 10^5 \frac{\text{cm}}{\text{sec}} \quad (3-6)$$

$$ka = \left[ \frac{2\pi}{C_w} \right] \left[ \frac{v_{s,p}}{2\pi a} \right] a = 3.69 \quad (3-7)$$

The theoretical value of the  $ka$  location of the first symmetric mode is slightly lower than the experimental  $ka$  value indicating a small error in using the tabulated values of either the Young's modulus or other constants. This slight deviation in the material constants most likely resulted from the manufacturing processes. Since facilities were not available to actually measure the elastic moduli of the stainless steel and the deviation is small, the tabulated values will be used. The form function versus  $ka$  plot also indicated the first antisymmetric mode will not be excited for  $ka$  values less than 10. (This observation is consistent with the theory since for the thin shell the phase speed of the first antisymmetric Lamb mode is significantly less than the propagation speed of the water.)

The first coating experiment performed was with the shell coated with 1/16 inch corprene. Figure 3-18 shows the theoretical form function, calculated by the procedure derived in Appendix D, as the solid line and the experimental data as points. The theoretical calculation assumes a Poisson's ratio of 0. The agreement of the theory with the experimental data is excellent. The form function graph does indicated a slight  $ka$  misalignment of the theoretical values with the experimental values of the form function similar to that observed for the uncoated shell. The theoretical and experimental form functions show resonance dips at approximate  $ka$  values of 1, 2, 3.7, and 4.2. The experimental data for  $ka$  values less than 2 is sparse. Two significant observations regarding the effect of the thin coating are:

1. the magnitude of the form function is reduced by the coating for  $ka$  values greater than 4 but, for  $ka$  values less than 4, the form function has an overall greater magnitude.
2. the resonance dip caused by the second circumnavigation of the first symmetric mode has been completely eliminated.

Figure 3-19 compares the theoretical form functions for the 1/16 inch corprene coating assuming a poisson's ratio of .4 and 0. For  $ka$  values less than 3.5, there is little difference. Substantial difference occurs for  $ka$  values greater than 3.5. Specifically, there is a larger and shifted resonace at a  $ka$  of 4.8 and a second resonace, mostlikely the second travel of the first symmetric wave at an approximately  $ka$  of 7.5. These additional resonances are not substantiated by the

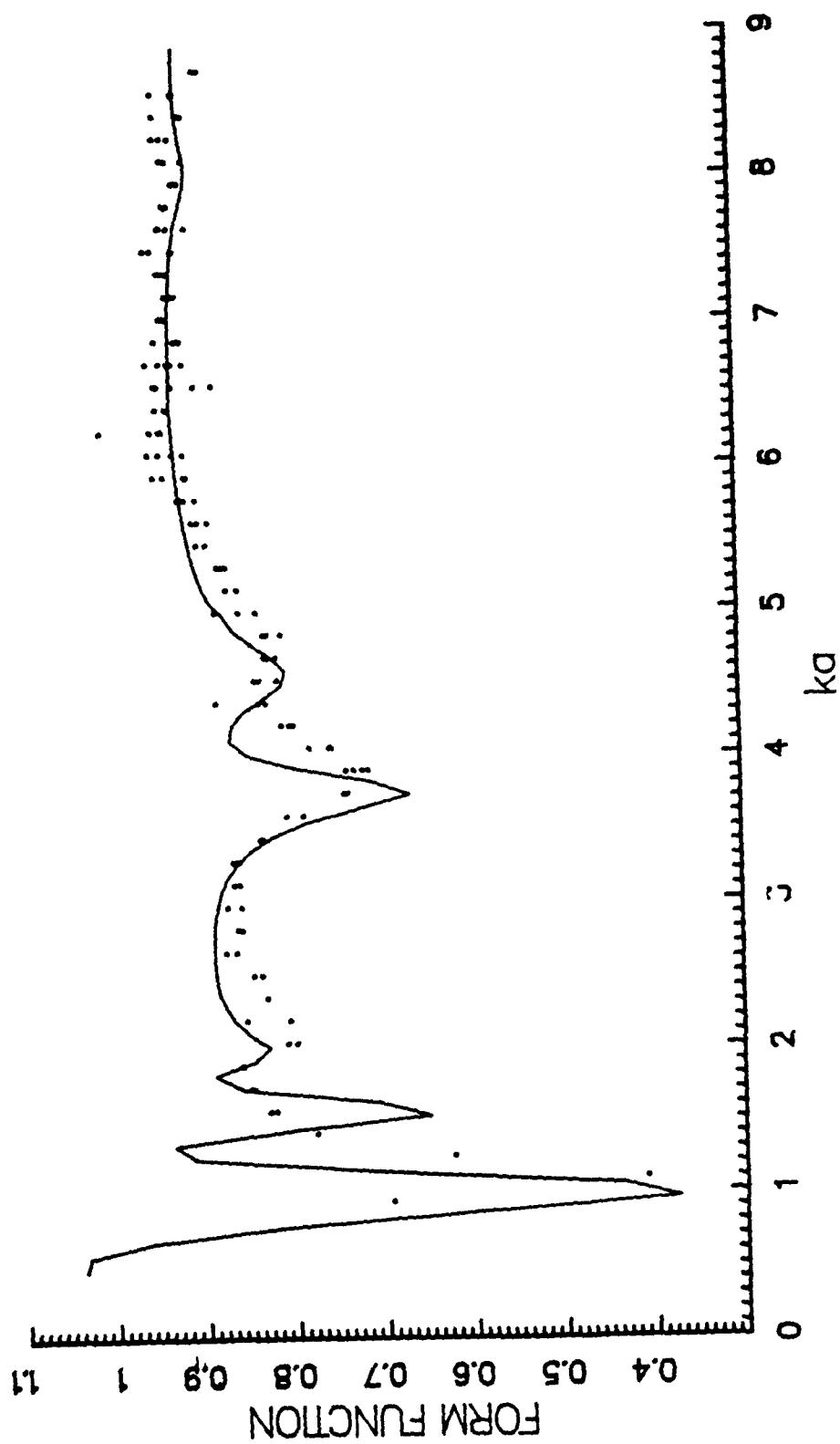


Figure 3-18 1/16" Corprene Coated Thin Shell Backscatter Form Function  
( $b/a = .97$ ) (Solid Line - Theory, Dots - Experimental Data)

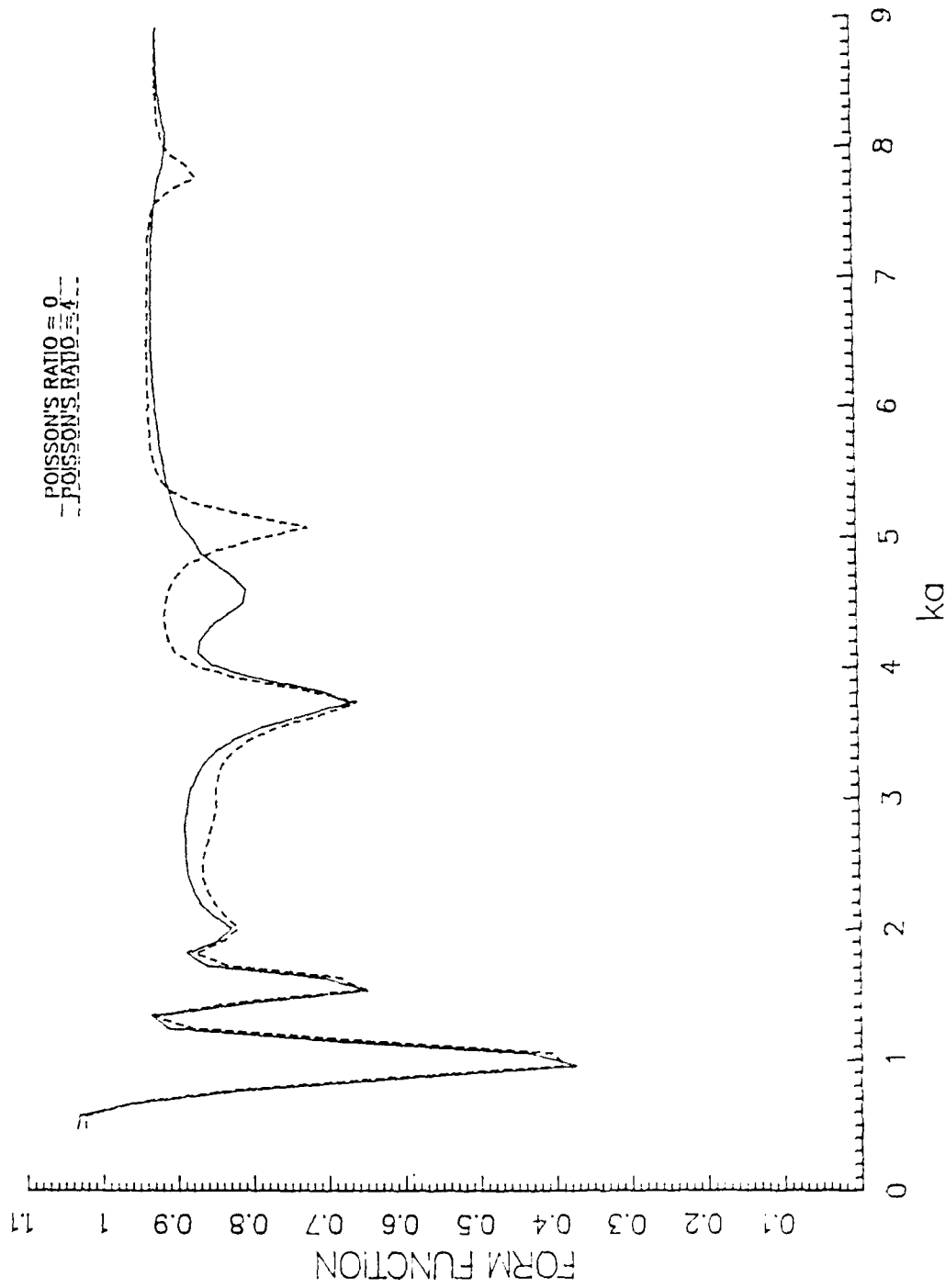


Figure 3-19 1/16" Cerprene Coated Thin Shell Theoretical Backscatter  
Form Function( $b/a = .97$ ) (Solid Line - Poisson's Ratio = 0.,  
Dashes - Poisson's Ratio = .4)

experimental data. Due to excellent agreement between the theoretical and experimental values, Poisson's ratio will be assumed to be 0.

In order to investigate the effect of thickness on coating performance, an additional .25 inches (.635 cm) of corprene was added to the 1/16 corprene coating (total corprene coating of 5/16 inches). Figure 3-20 shows the theoretical form function as the solid line and the experimental results as points. The agreement is excellent between  $ka$  values of 1.5 and 8.5. The experimental data shows a decrease of approximately 0.5 dB at  $ka \approx 9.0$ . This decrease is probably caused by experimental error. In the higher frequency range, the compliant coating is becoming more attenuating, therefore decoupling sound from the shell more efficiently, and theoretically should be approaching the pressure release boundary condition. Experimental errors that could cause a reduced scattered signal at this relatively high frequency (56 kHz) are:

1. the shell may not be completely vertical.
2. slight misalignment of the shell, 8103 hydrophone, and F-33 transducer.
3. possible scattering of the incident signal by the 8103 hydrophone and its support tube.

Significant deterioration of the experimental data occurs below a  $ka$  value of 1.5. This result is consistent with all previous measurements and is attributed to the frequency range and measurement facilities. The effect of the additional coating material is to shift the resonances to lower  $ka$  values and to spread the resonance dip over a wider  $ka$  range (remove the sharpness of the dip). The sharp resonance



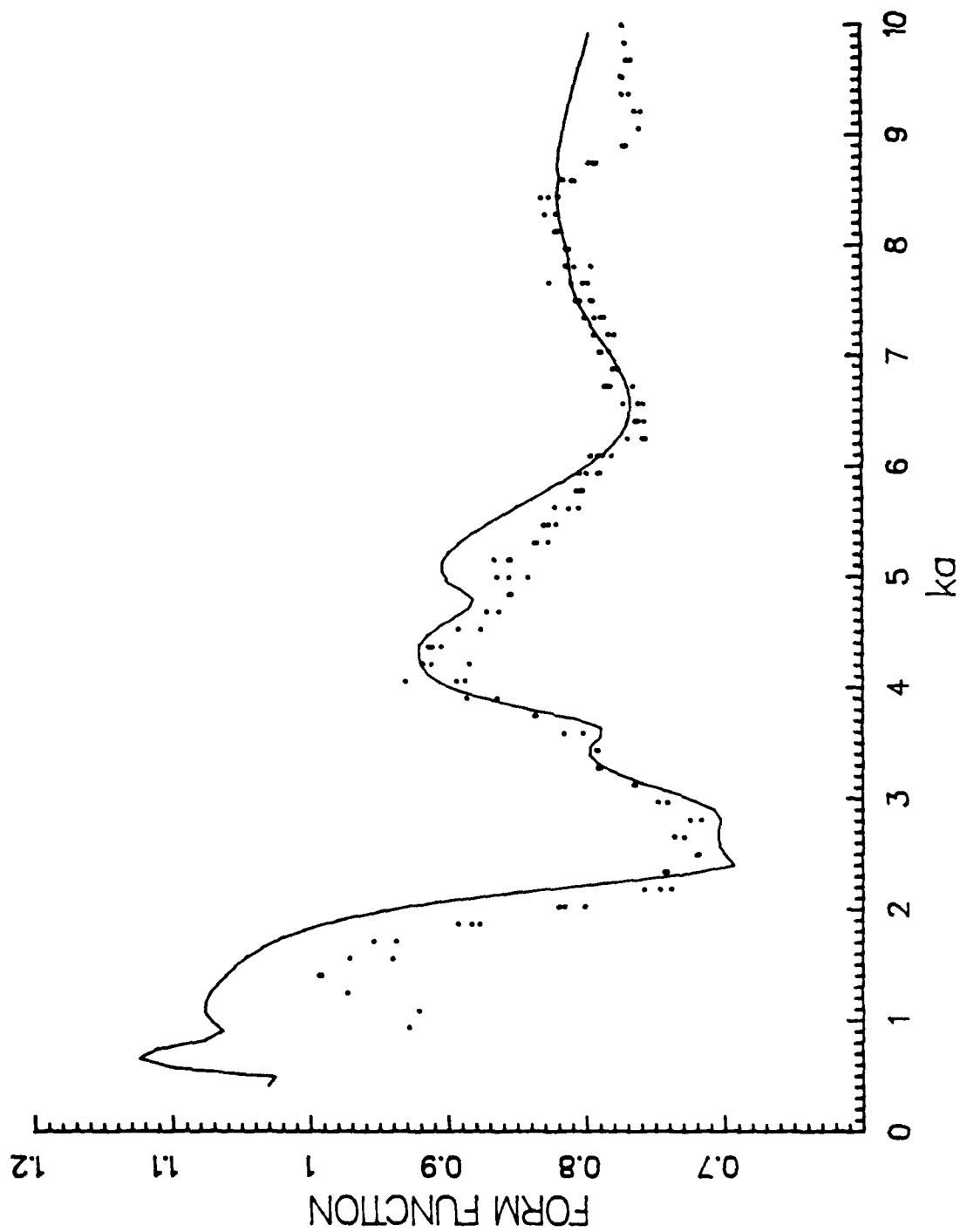


Figure 3-20 5/16" Corprene Coated Thin Shell Backscatter Form Function  
( $b/a = .97$ ) (Solid Line - Theory, Dots - Experimental Data)

dip that occurs at a  $ka$  of 3.7 on the thinner corprene coating is shifted to a  $ka$  value of 2.5. The dip also covers a  $\Delta ka$  range of 2 whereas the resonance width of the thinner material covers a  $\Delta ka$  of .5. The depth of the dip is slightly reduced for the thicker coating but not as much as expected. The relative peak that occurs at a  $ka$  of 4.2 for the thinner coating is shifted to a slightly lower  $ka$  value and its magnitude is increased from 0.88 to 0.93. Noticeably missing from the thicker coating plot is the extensive resonance structure that exist for the thinner coating at  $ka$  values less than 2. Another unanticipated result is that the magnitude of the form function after a  $ka$  of 7 is approximately 1 dB lower than the thinner coating form function. The peak that exist at the approximate  $ka$  value of 4 has reversed relative magnitude positions with the flat portion of form function (for  $ka$  values greater than 7). If a Poisson's ratio of .4 is utilized in the theoretical calculations, the resonance dip at  $ka=2.7$  and peak at a  $ka=4.3$  are significantly larger than indicated by the experimental data. The thicker corprene layer has therefore reinforced the evidence for a small Poisson's ratio.

For both corprene thicknesses, the scattered signal was inverted relative to the incident signal.

Figure 3-21 shows the form function plots for various thicknesses of corprene coatings. It is particularly apparent that for even large thicknesses of corprene (36 times the shell thickness), the resonance structure is present for  $ka$  values less than 3.0.

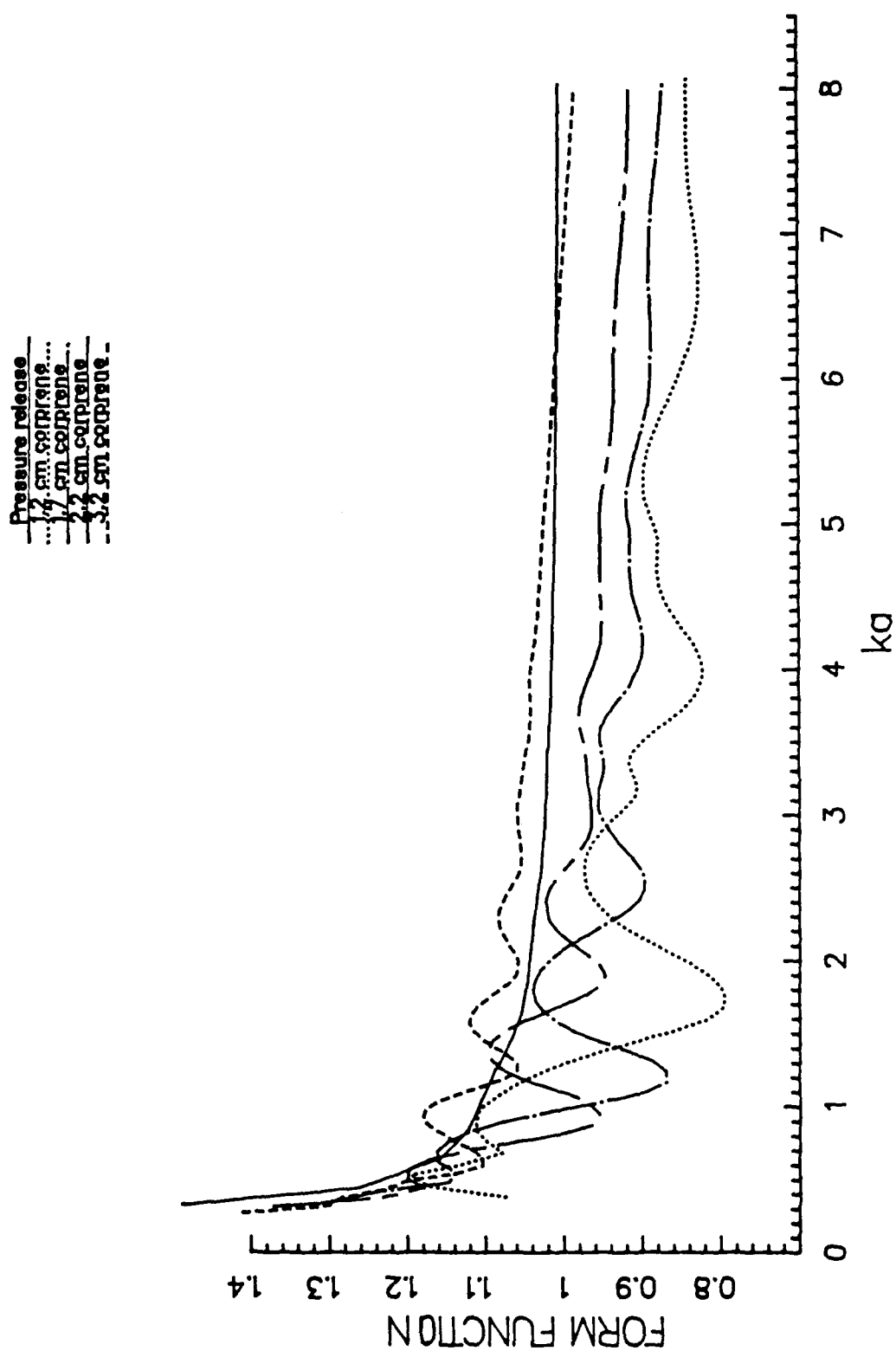


Figure 3-21 Theoretical Backscatter Form Function for Four Thicknesses of Corprene

The final infinite cylinder coating experiment was to coat the shell with .25 inches of closed cell nitrile. Figure 3-22 shows the results of the experimental values (points) plotted with the theoretical form function (solid line). Again, the agreement between the theoretical and experimental values is excellent. The experimental data shows some structure in the 3 to 5 ka range that is not indicated in the theoretical form function. Two plausible explanations for this additional structure are:

1. seams in the coating were not sufficiently closed to prevent partial excitation of the shell.
2. when the coating was placed on the shell, the curvature caused the coating to be slightly stretched to ensure a smooth fit over the shell. The stretching may have caused the air bubble in the coating to elongate in the tangential direction and shrink in the radial direction causing an effective reduction in the percentage of air, relative to a wavelength, between the fluid and the shell.

As ka values become smaller, the theoretical form function increases rapidly which is characteristic of the perfect pressure release cylinder. At a ka of approximately .2, the form function peaks and approaches 0 as ka approaches 0. This behavior is consistent with physical reality since at some small ka (large wavelength to coating thickness ratio), the coating will cease to "look" pressure release and the form function will be dominated by the characteristics of the shell, i.e. approach 0 as ka goes to 0.

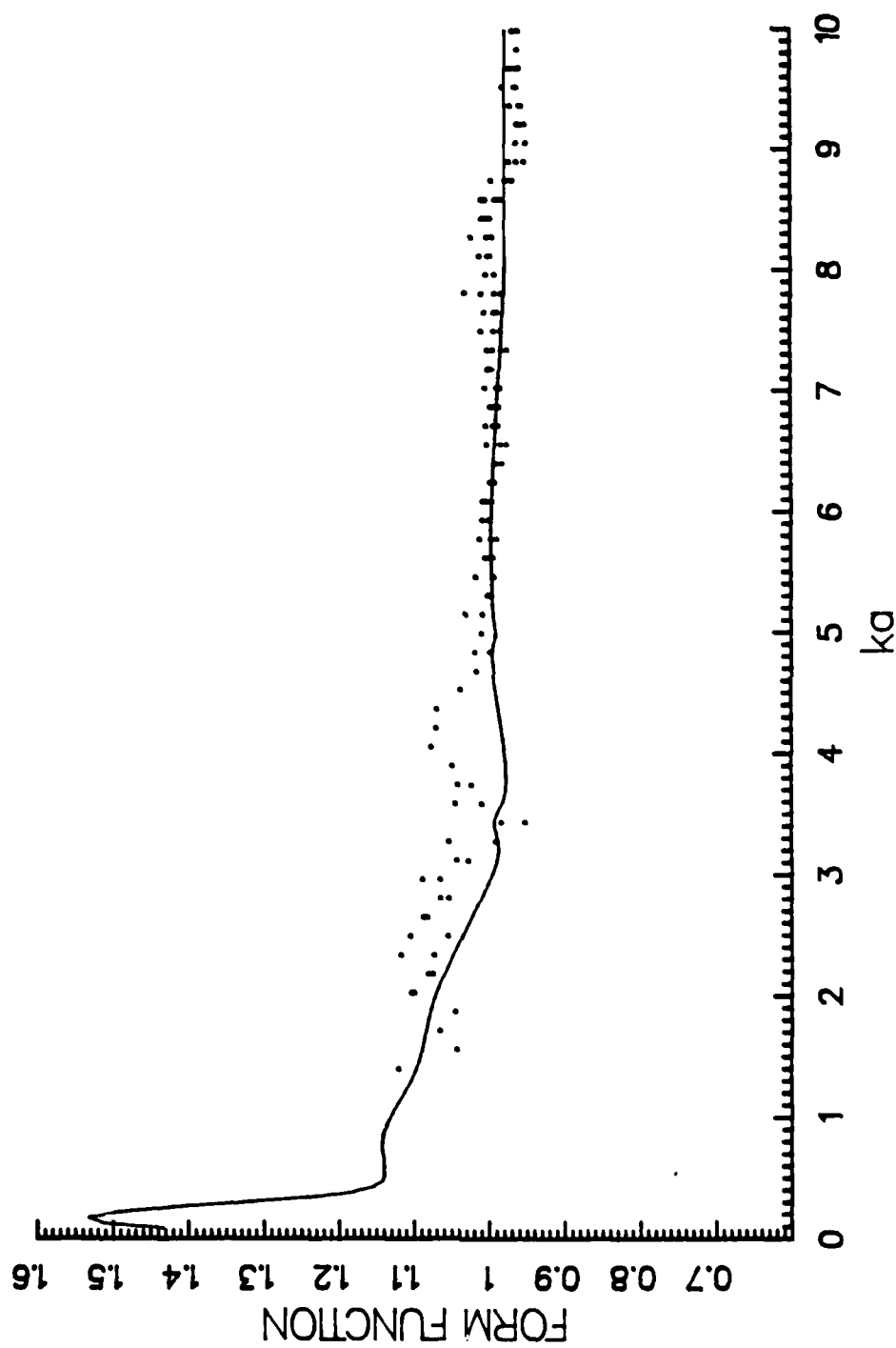


Figure 3-22 1/4" Nitrile Coated Thin Shell Backscatter Form Function  
( $b/a \approx .97$ ) (Solid Line - Theory, Dots - Experimental Data)

Figure 3-23 displays the theoretical form functions for two thicknesses of the closed cell nitrile and the pressure release cylinder as a function of  $ka$ . The form function for the .25 inch thick sample of nitrile is within 1 dB (the standard accuracy measure for most scattering experiments) of the form function for the pressure release cylinder for  $ka$  values equal to and greater than 0.5. The resonance structure of the shell is effectively removed (there are no resonance peaks or dips that have a greater variation than 1 dB from the baseline form function). The 1/16 inch nitrile does not produce a pressure release condition for  $ka$  values less than 4 as indicated by the large resonance dips at  $ka$  values of 3.7 and 0.8. As the  $ka$  values increase, both thicknesses of nitrile show an increased pressure release behavior as expected.

Figure 3-24 is the scattered waveform for the uncoated shell and figure 3-25 is the waveform for the nitrile coated shell for center frequencies of 40 kHz. The echo from the uncoated shell is dominated by the specular reflection. The only obvious difference in the waveforms (coated shell versus uncoated shell) is the presence of a small extension of the signal at the end of the specular reflection for the uncoated shell.

Figure 3-26 illustrates that a .25 inch nitrile coating on a thin shell, with an inner to outer radius ratio of .99, will decrease the form function of the shell by 1.6 dB (the form function of the coated shell remains about the same magnitude regardless of the shell thickness but, the form function of the shell increases for low  $ka$  values as the thickness decreases).

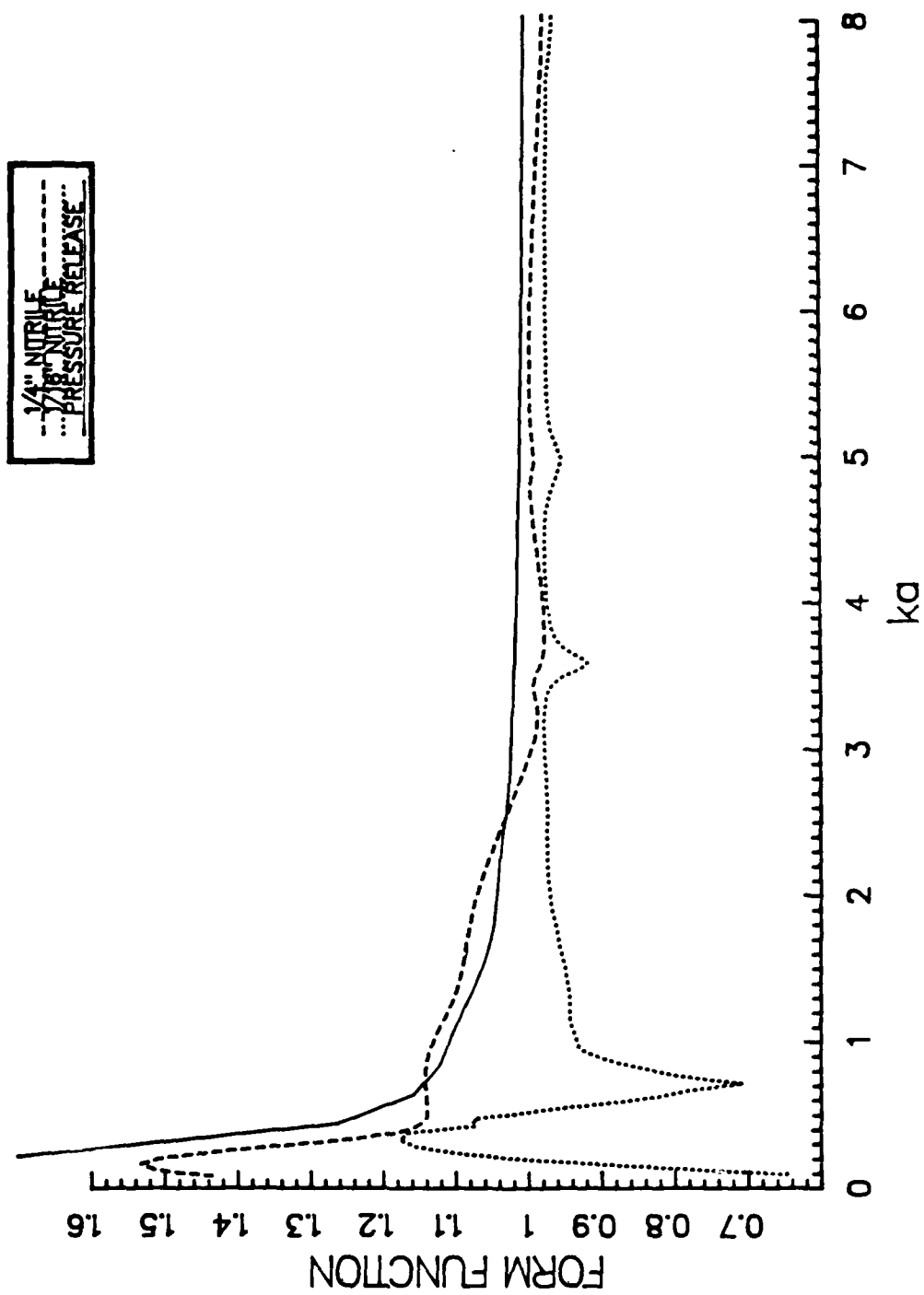


Figure 3-23 Theoretical Backscatter Form Function for Two Thicknesses of Nitrile and Pressure Release Cylinder

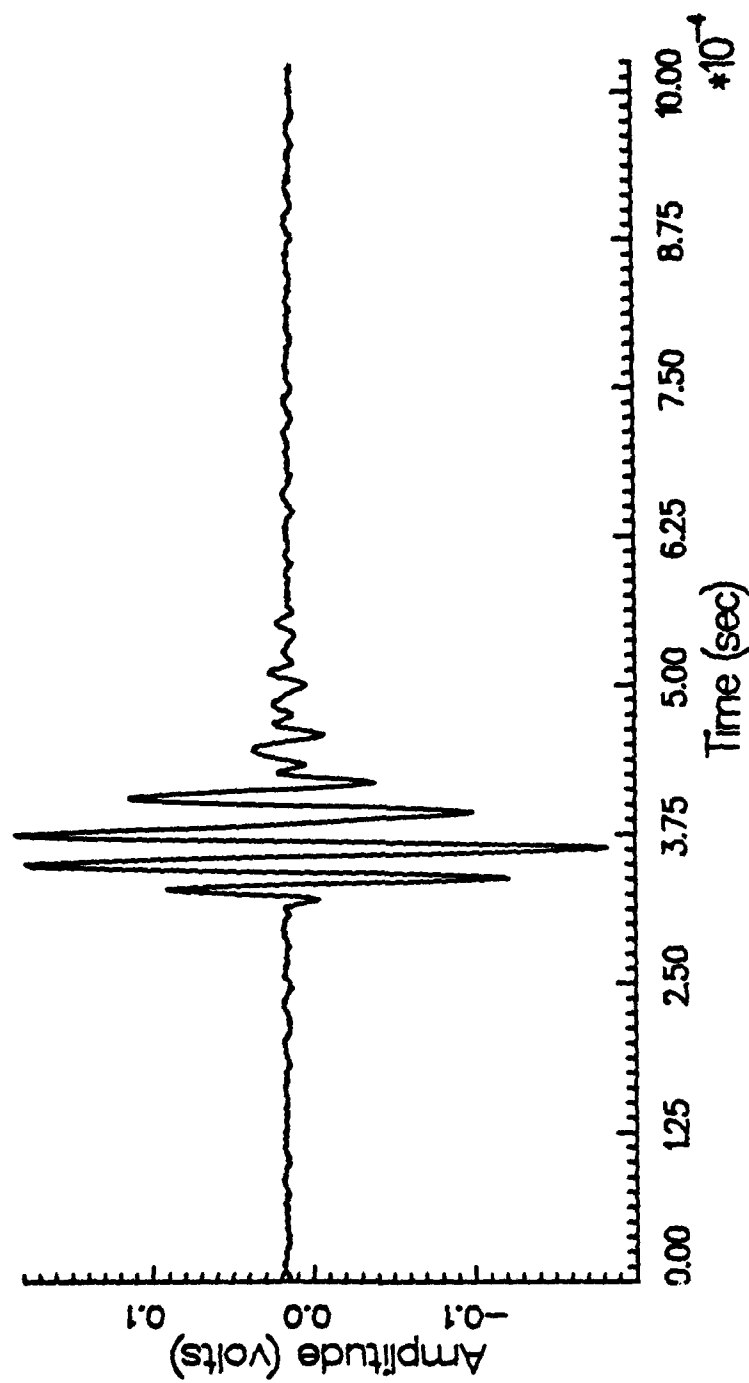


Figure 3-24 Uncoated Thin Shell Backscatter Waveform (40kHz Center Frequency)



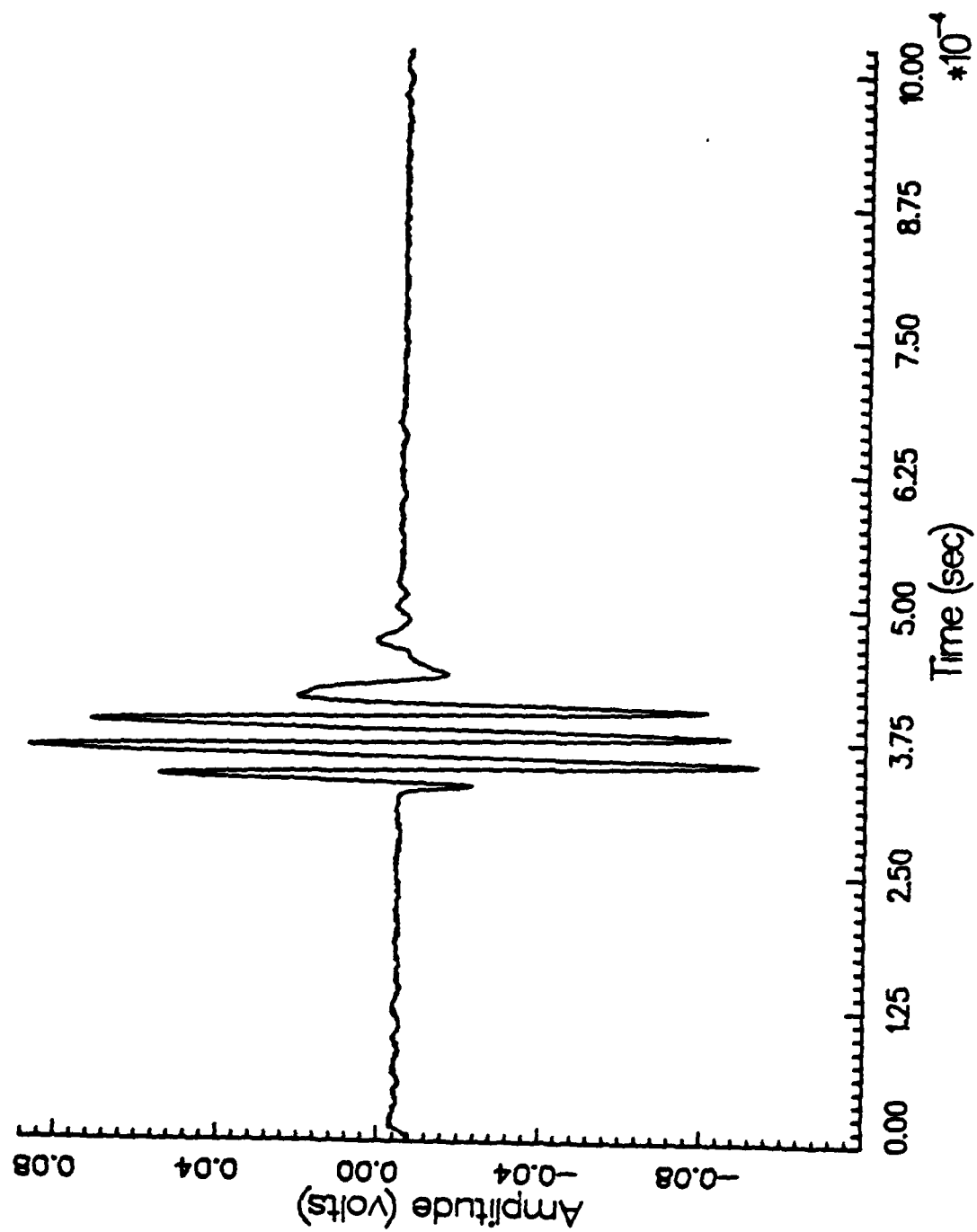


Figure 3-25 Nitrile Coated Thin Shell Backscatter Waveform (40kHz Center Frequency)

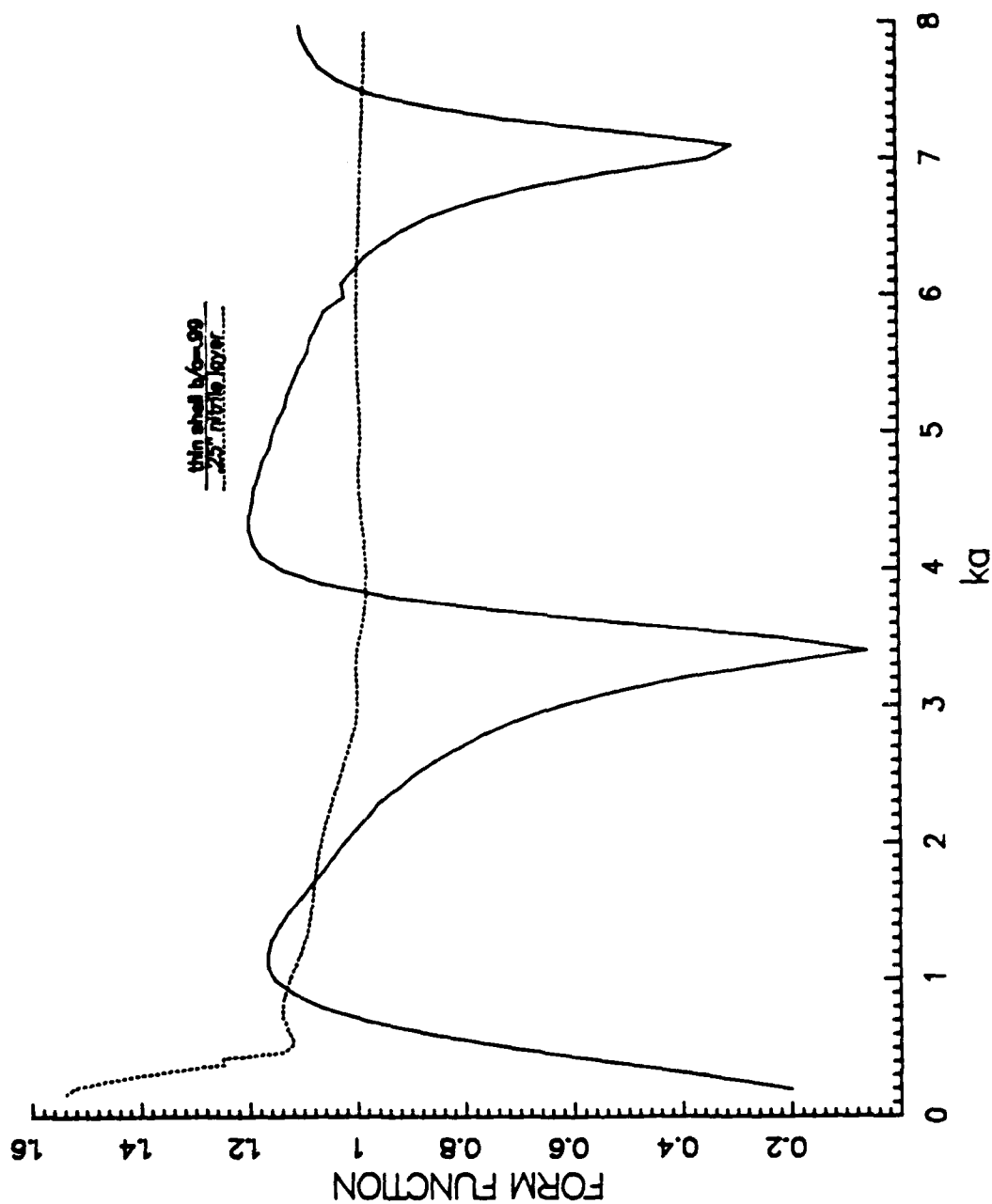


Figure 3-26 Theoretical Backscatter Form Function for 0.25 inches of Nitrite Coating on Thin Shell and Pressure Release Cylinder

### Finite Shell with End On Incident Signal

The following observations are made from the waveforms and normalized scattered pressure versus  $ka$  plots for the coated and uncoated finite cylindrical shell experiments for axial incidence. The finite shell is coated with .25 inches of closed cell neoprene rubber for the coated case. Figures 3-27 and 3-28 are representative waveforms for the uncoated and coated cases. The center frequency for the waveforms in figures 3-27 and 3-28 is 60 kHz. The significant observations are:

1. the uncoated shell's specular reflection is in phase with the incident signal whereas the coated shell's specular reflection is inverted relative to the incident signal.
2. The specular reflections for both cases have similar magnitudes. The coating does not have a significant effect on the magnitude of the normalized scattered pressure, although the coated shell's normalized scattered pressure is consistently slightly larger than the uncoated normalized pressure, for  $ka$  values less than 11 as indicated in figure 3-29. The reason for this slight magnitude difference is that the coated cylinder is physically larger due to the .25 inch increase in radius. This 12.5% increase in radius affects the scattered field in a quadratic manner whereas the  $ka$  scaling only accounts for the increased radius linearly. For  $ka$  values greater than 11, the neoprene coating eliminates the severe

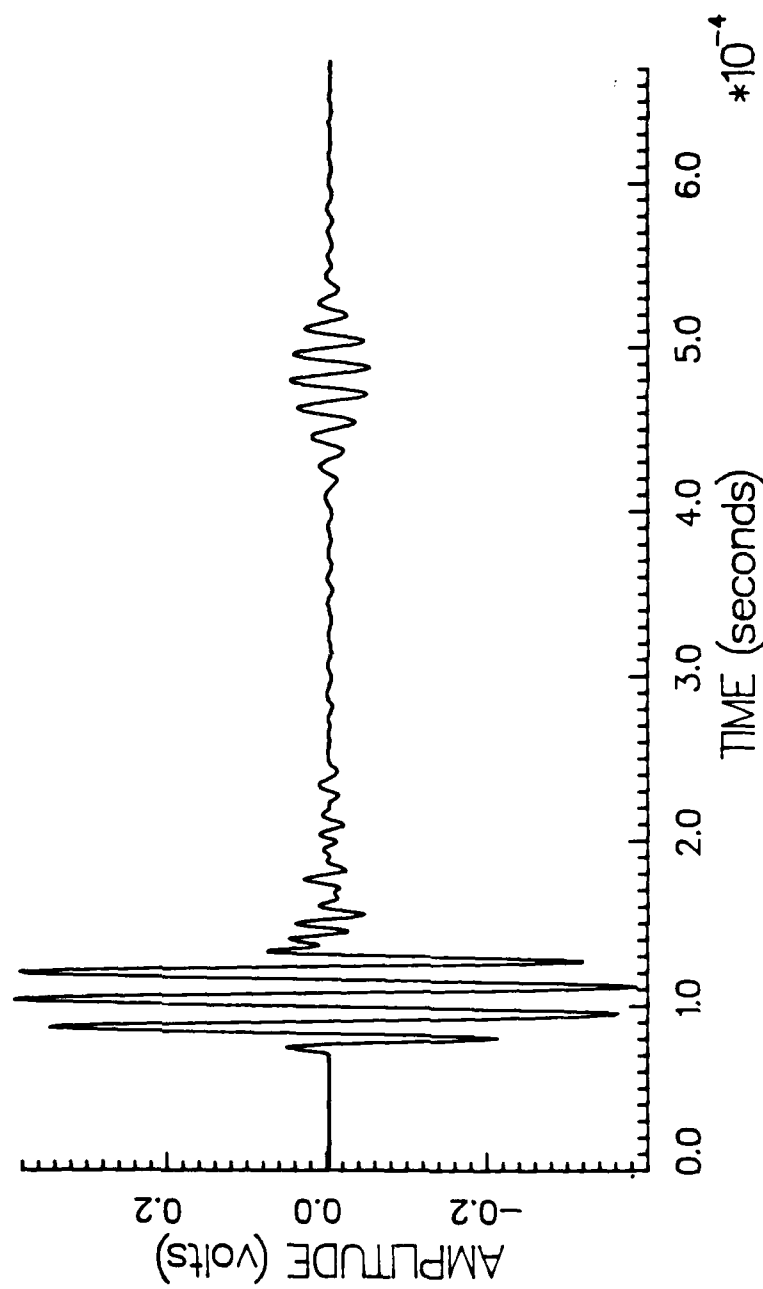


Figure 3-27 Scattered Signal from Uncoated Thick Finite Shell ( $b/a = .9$ )  
for Axial Incidence (60 kHz Center Frequency)

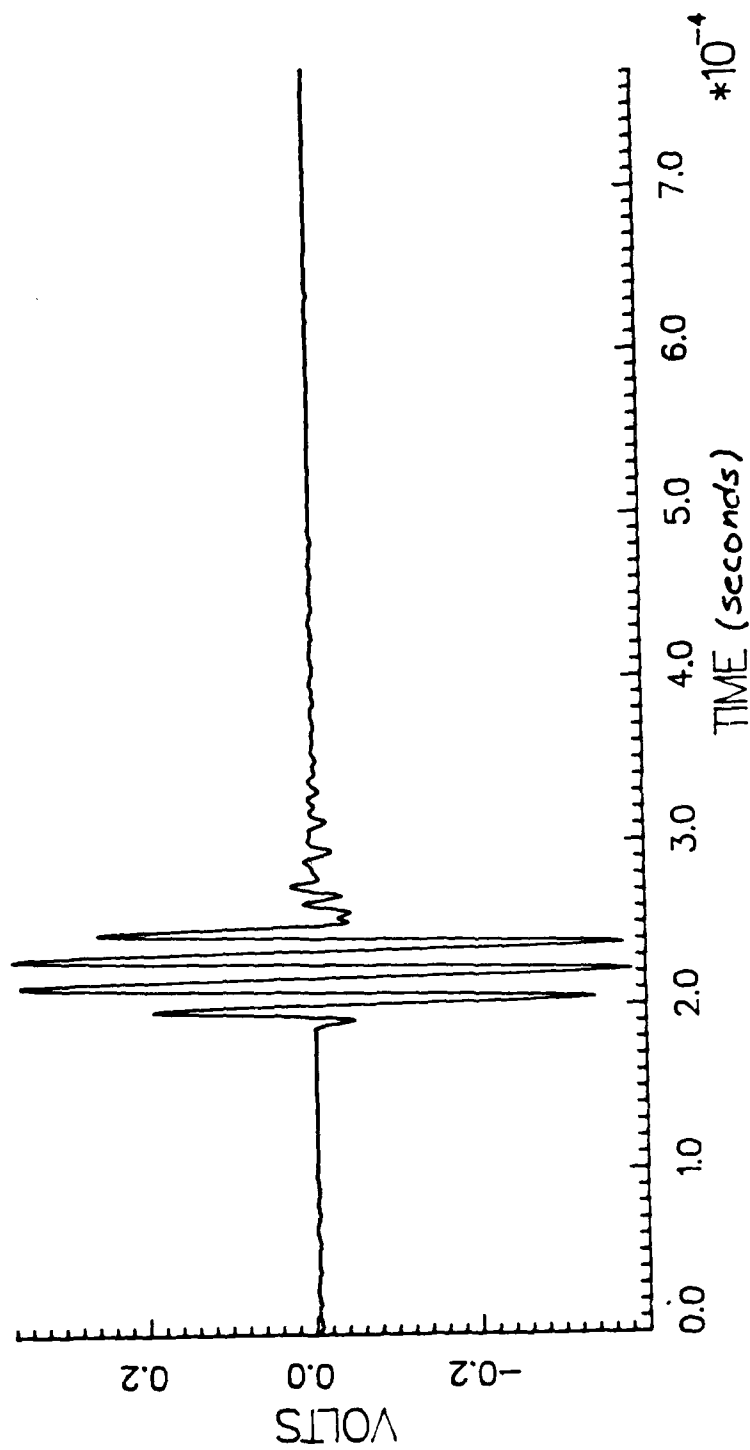


Figure 3-28 Scattered Signal from Thick Finite Shell ( $b/a = .9$ ) Coated  
with 0.25 inches of Neoprene for Axial Incidence  
(60 kHz Center Frequency)

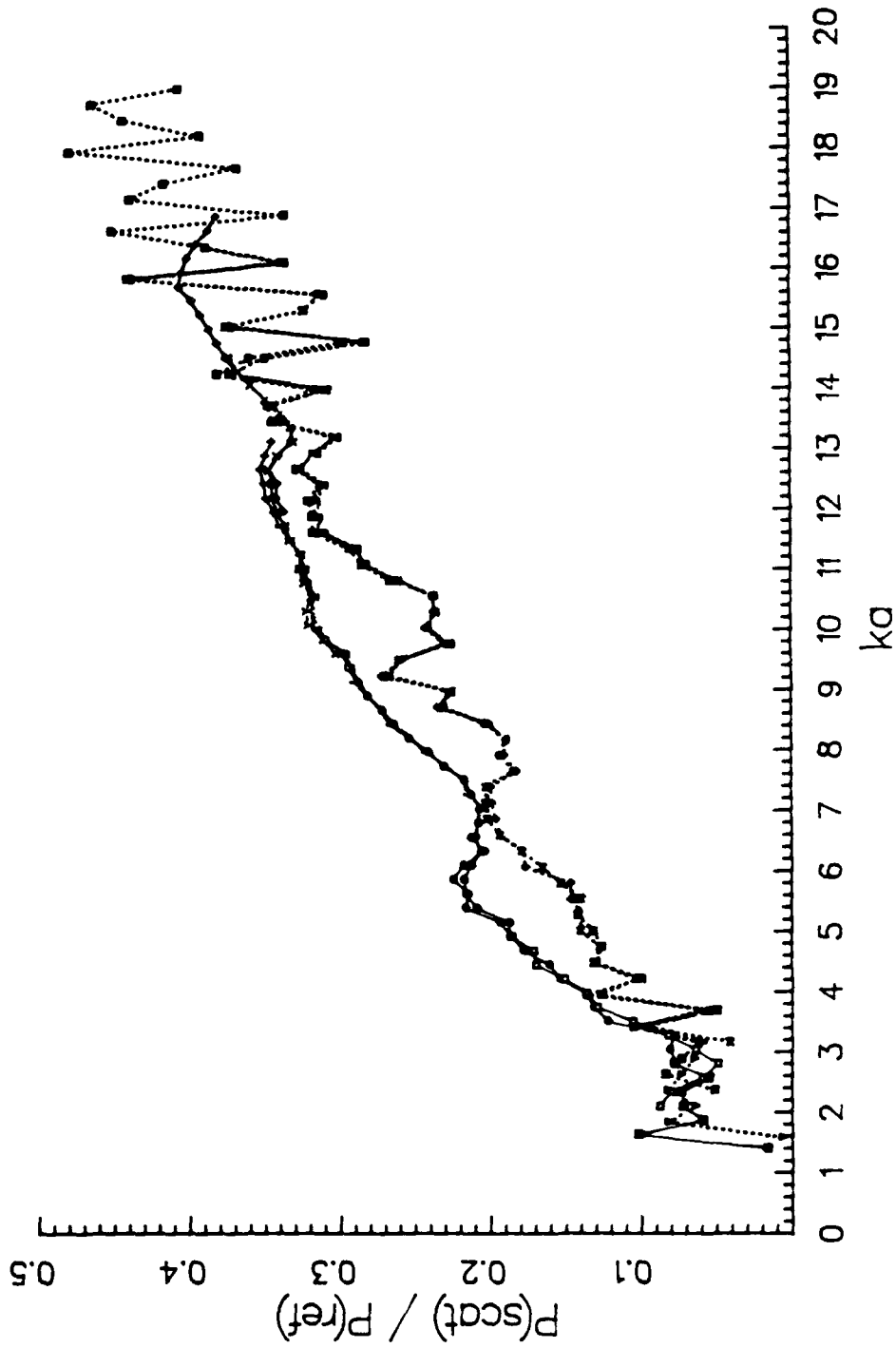


Figure 3-29 Normalized Scattered Pressure Versus  $ka$  for Thick Finite Shell ( $b/a = .9$ ) with Axial Incidence (Solid Line is Shell Coated with 0.25 inches of Neoprene, Dotted Line is Uncoated Shell)

resonance structure present in the uncoated case.

3. For the uncoated shell, a second scattered signal arrives at 320 microseconds after the specular reflection. This time difference corresponds to the time necessary to travel the length of the shell at the longitudinal wave speed of the stainless steel ( $68 \mu\text{seconds}$ ) plus the time to travel the length of the shell at the propagation speed of the water ( $251 \mu\text{seconds}$ ). The difference between the experimentally observed time delay and the calculated time delay is less than 5%. The actual path traveled is unknown. In figure 3-30, the center frequency is 45 kHz, the second scattered signal shape is different from figure 3-28 and it appears the signal is actually a combination of signals indicating possible multiple reflections are occurring in the end caps.

4. Figure 3-31 compares the coated shell's normalized scattered pressure versus  $ka$  with the normalized scattered pressure determined by the SHIP program for the ideal pressure release finite cylinder. Both the coated and uncoated shells' normalized pressures follow the trend of and are within 2.5 dB of the SHIP results for  $ka$  values less than 11. At the larger  $ka$  values, the uncoated shell's normalized pressure significantly departs from the pressure release structure predicted by the SHIP program. The SHIP program values were verified by the CHIEF program and were found to be within 1% at a  $ka$  of 2.0 and within 3% at a  $ka$  of 3.0. The CHIEF program employed a 480 sub-division scheme. Verification at larger  $ka$  values was not performed due to the large amount of computer memory (proportional to the number of subdivisions squared) and the long computational

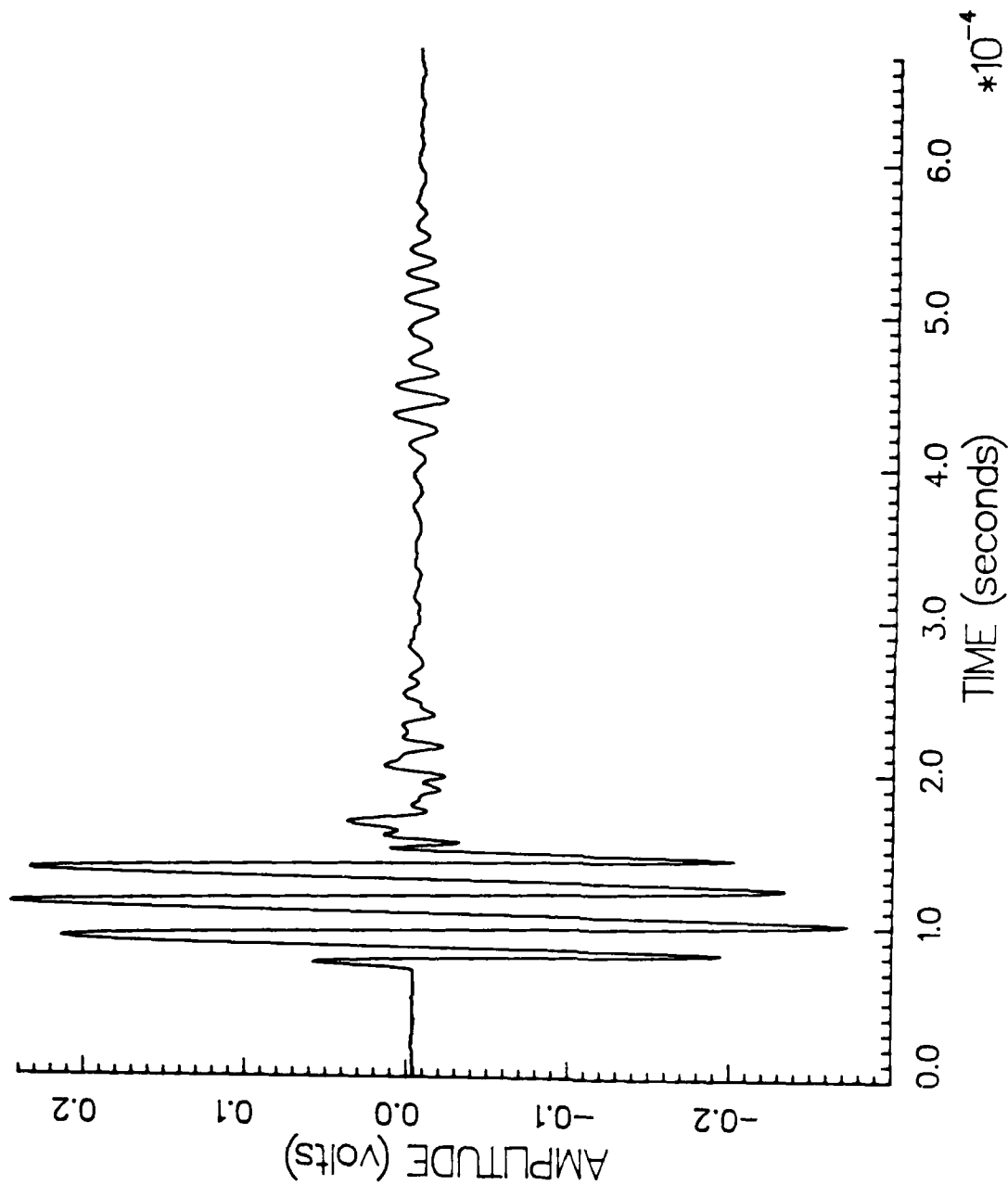


Figure 3-30 Scattered Signal from Uncoated Thick Finite Shell ( $b/a = .9$ )  
for Axial Incidence (45 kHz Center Frequency)



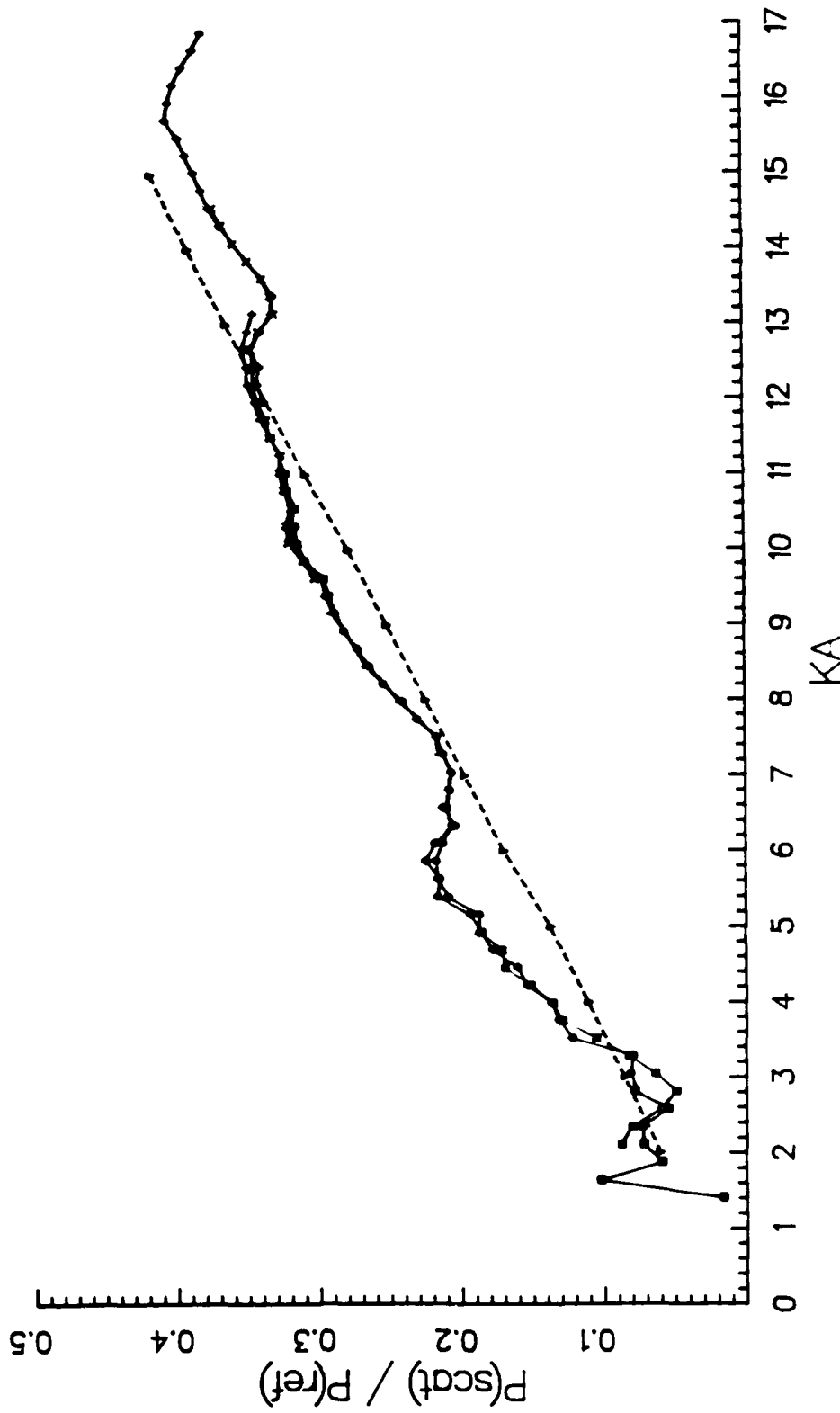


Figure 3-31 Normalized Scattered Pressure Versus  $ka$  for Thick Finite Shell ( $h/a = 9$ ) with Axial Incidence and SHIP Output for Pressure Release Finite Cylinder (Solid Line is Shell Coated with 0.25 inches of Neoprene, Dashed Line is SHIP)

time required by CHIEF. For the equivalent accuracy (as indicated above), the CHIEF program required approximately 5 hours computer time (cpu) versus approximately 2 minutes of computer time for the SHIP program on a VAX 750 computer.

Although the coated shell's normalized pressure does show some structure, particularly at the low  $ka$  values, it is unclear if this results from acoustic transmission through the layer and excitation of the shell or from acoustic excitation of shell via the seams of the coating. In either case, the resonance effects are substantially damped.

#### Finite Shell with Normal (Side) Incident Signal

The following observations are made from the waveforms and normalized scattered pressure versus  $ka$  plots for the coated and uncoated finite cylindrical shell experiments for normal incidence. The finite shell is the same shell and coating used for the end on or axial incidence case. Figures 3-32 and 3-33 are representative waveforms for the uncoated and coated cases. The center frequency for the waveforms in figures 3-32 and 3-33 is 40 kHz. The observations are:

1. The uncoated shell's specular reflection is in phase with the incident signal whereas the coated shell's specular reflection is inverted relative to the incident signal.

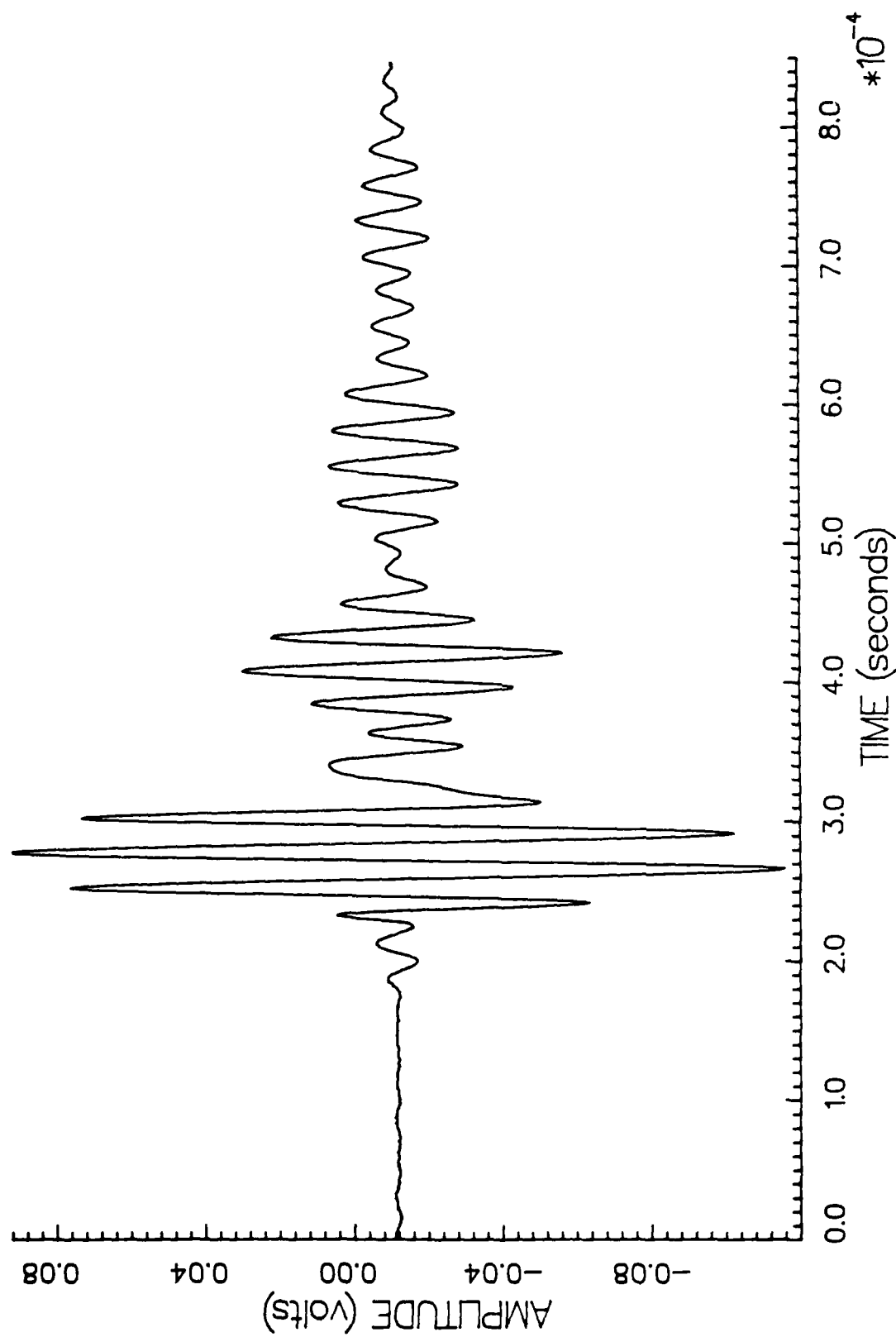


Figure 3-32 Scattered Signal from Uncoated Thick Finite Shell ( $b/a = .9$ )  
for Normal Incidence (40 kHz Center Frequency)

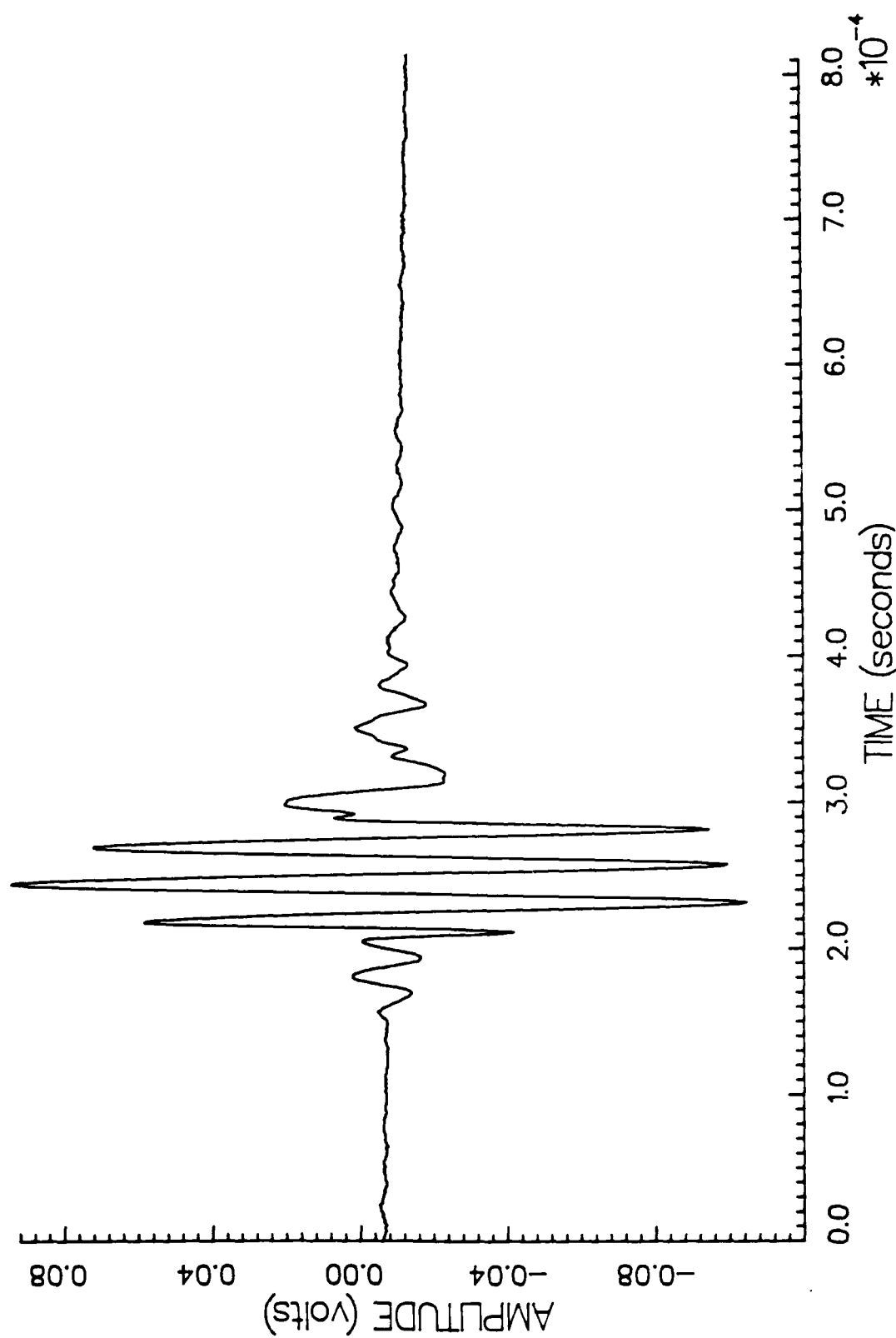


Figure 3-33 Scattered Signal from Thick Finite Shell ( $b/a = .9$ ) Coated  
with 0.25 inches of Neoprene for Normal Incidence  
(40 kHz Center Frequency)

2. For the uncoated shell, the two types of circumferential waves are observed. The first circumferential wave observed is the first symmetric Lamb mode which travels with a phase and group speed of

$$v_s = \sqrt{\frac{E}{\rho (1 - \nu^2)}} = 5.53 \times 10^5 \frac{\text{cm}}{\text{sec}} \quad (3-8)$$

The difference in arrival times of subsequent circumnavigations of the shell is equal to the circumference of the shell divided by the phase speed (60  $\mu$ seconds). The first travel of the symmetric wave is contained in the specular reflection and can not be directly observed. Subsequent travels of this wave is observable in figure 3-34 which has a 20 kHz center frequency. The second circumferential wave observed is the first antisymmetric Lamb mode. The phase speed is determined from equation (1-8)

$$v_{a,p} = 4 \sqrt{\frac{E}{3\rho (1 - \nu^2)}} \sqrt{\frac{\omega h}{2}}$$

This equation for phase speed neglects any curvature effects. Viktorov<sup>36</sup> demonstrates a curvature correction that relates the phase speed as calculated in the center of the shell (by the above equation) to the phase speed at the outer surface by

$$v_{p,\text{surface}} = \frac{\frac{h}{2} + a}{a} v_p = 1.047 v_p \quad (3-9)$$

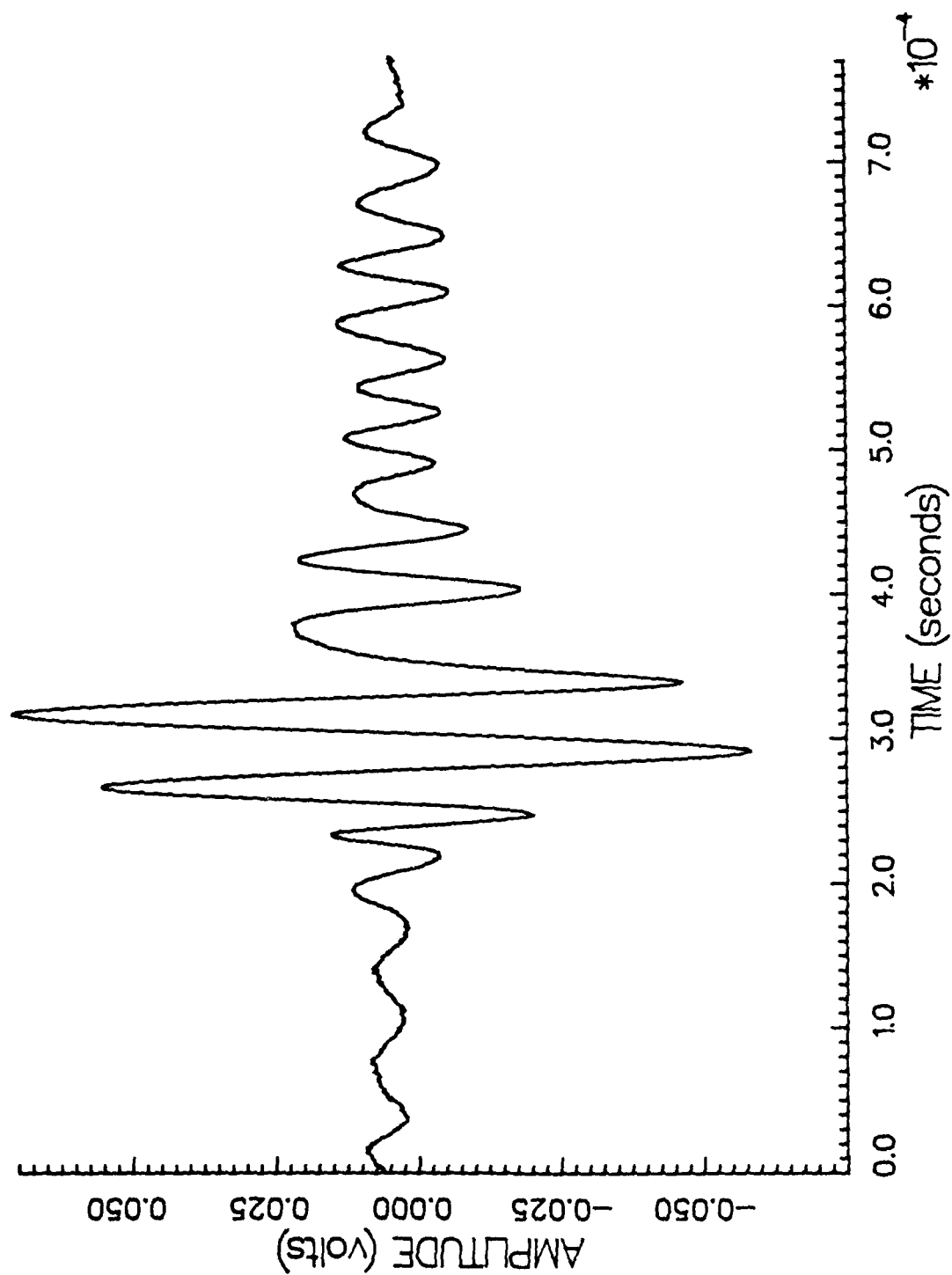


Figure 3-34 Scattered Signal from Uncoated Thick Finite Shell ( $b/a = .9$ )  
for Normal Incidence (20 kHz Center Frequency)

where  $a$  is the outer radius of the shell. For the 40kHz center frequency incident signal, the curvature corrected phase speed for the first antisymmetric Lamb mode is  $1.53 \times 10^5$  cm/sec. In order for the wave to be generated in the shell, the phase speed of the wave must be greater than the propagation speed of the water. For a 30 kHz center frequency, the first antisymmetric mode is still observed even though the calculated phase speed is less than the propagation speed of the water. Three reason for this are:

- a. The elastic constants for the stainless steel shell are actually higher than the tabulated values, possibly due to the fabrication process.
- b. The sound propagation speed for the actual measurement facilities needs to be more accurately determined (actual temperature corrected speed is  $1.48 \times 10^5$  cm/sec).
- c. The standard plate analysis is not sufficiently accurate for this shell experiment, since the shell is fluid loaded on one side and air loaded on the other. In addition, end effects caused by the thick end caps are not accounted for.

Figure 3-35 is the waveform for the coated shell for an incident signal center frequency of 40kHz. Particularly noticeable is the lack of the antisymmetric mode signal after the specular reflection.

3. In figure 3-36, the normalized scattered pressure is plotted against increasing  $ka$  values for both the coated and uncoated cases. The normalized scattered pressure for the coated shell is approximately three times larger than the

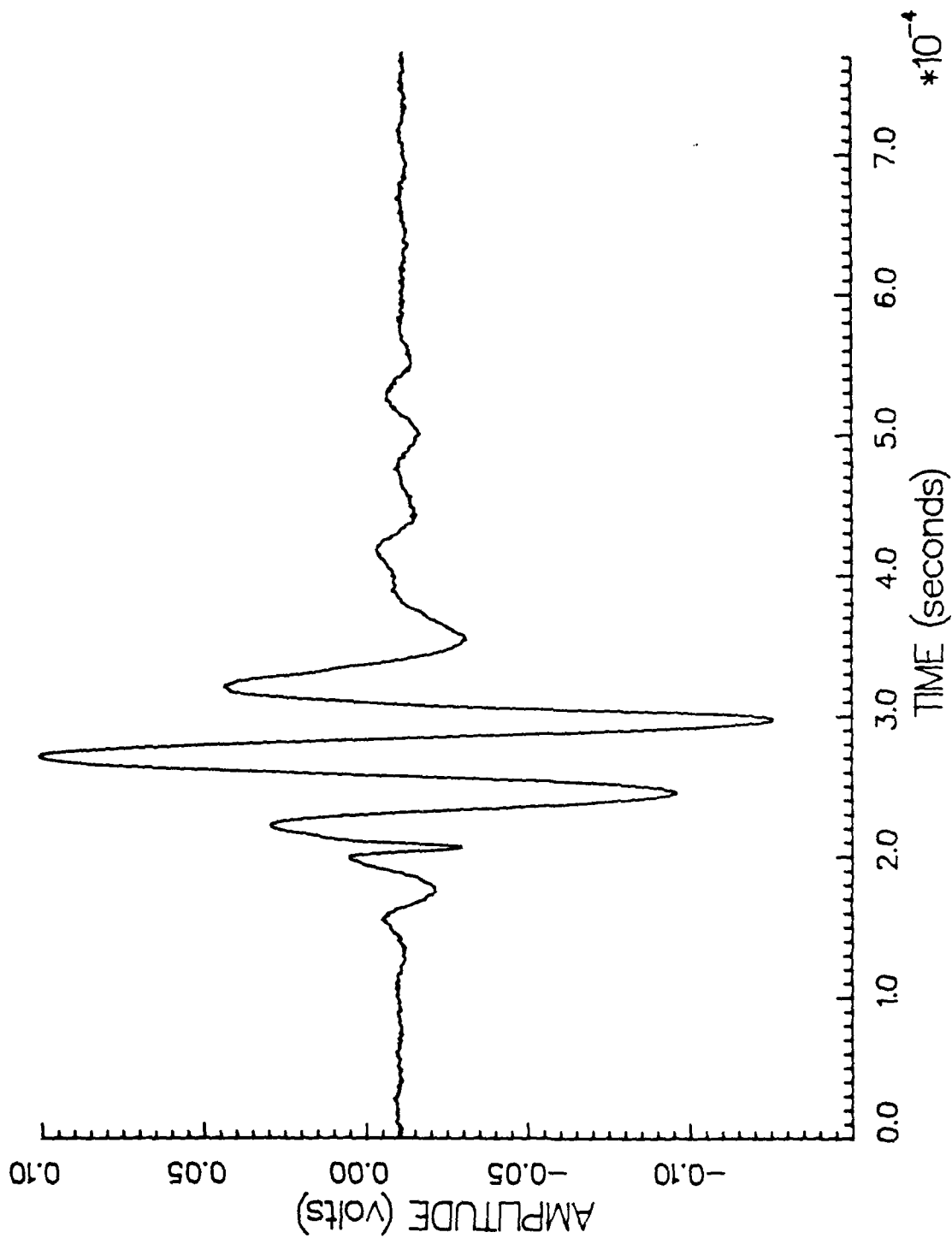


Figure 3-35 Scattered Signal from Thick Finite Shell ( $h/a \approx 9$ ) Coated  
with 0.25 inches of Neoprene for Normal Incidence  
(20 kHz Center Frequency)



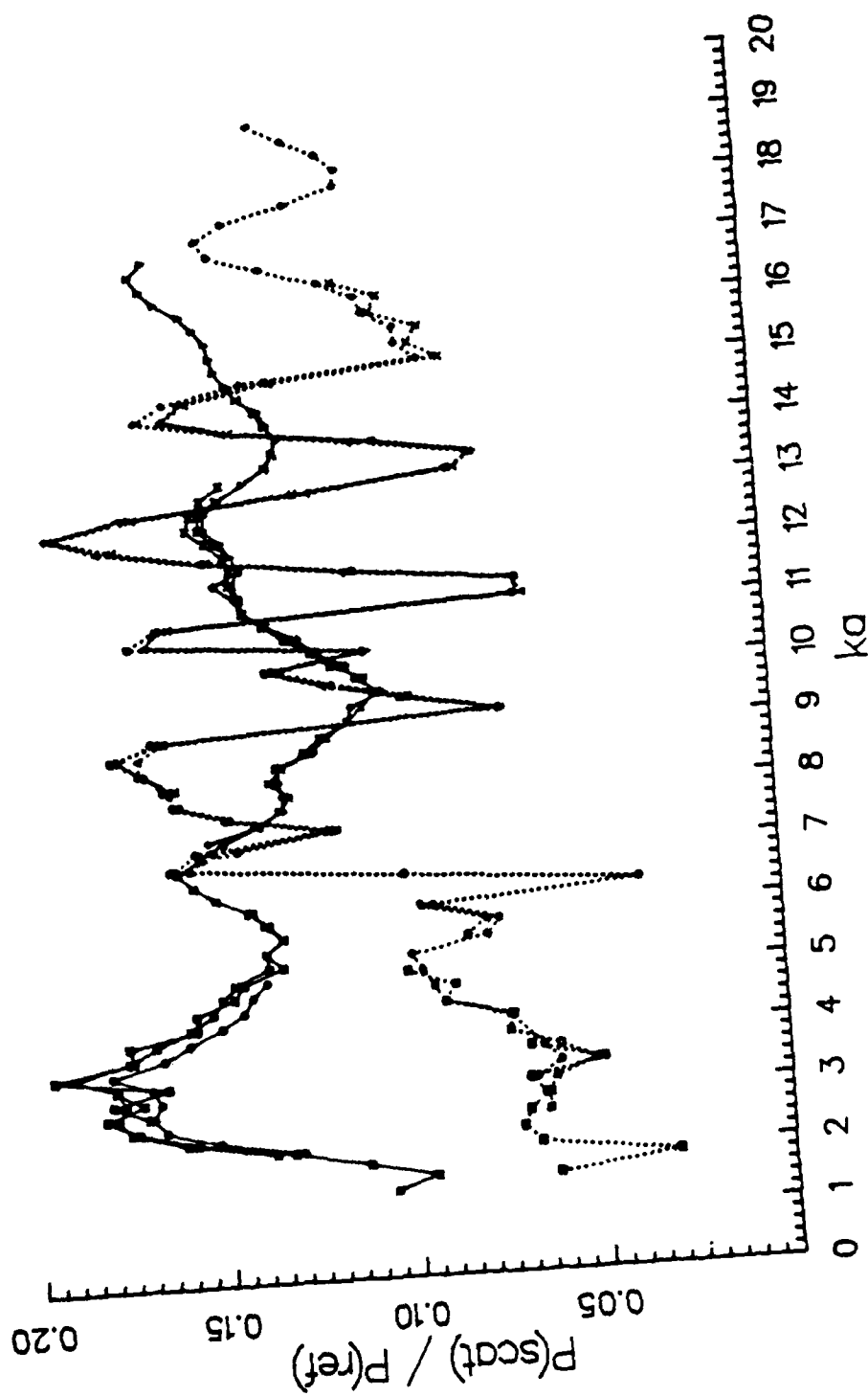


Figure 3-36 Normalized Scattered Pressure Versus  $ka$  for Thick Finite Shell ( $b/a = .9$ ) with Normal Incidence (Solid Line is Shell Coated with 0.25 inches of Neoprene, Dotted Line is Uncoated Shell)

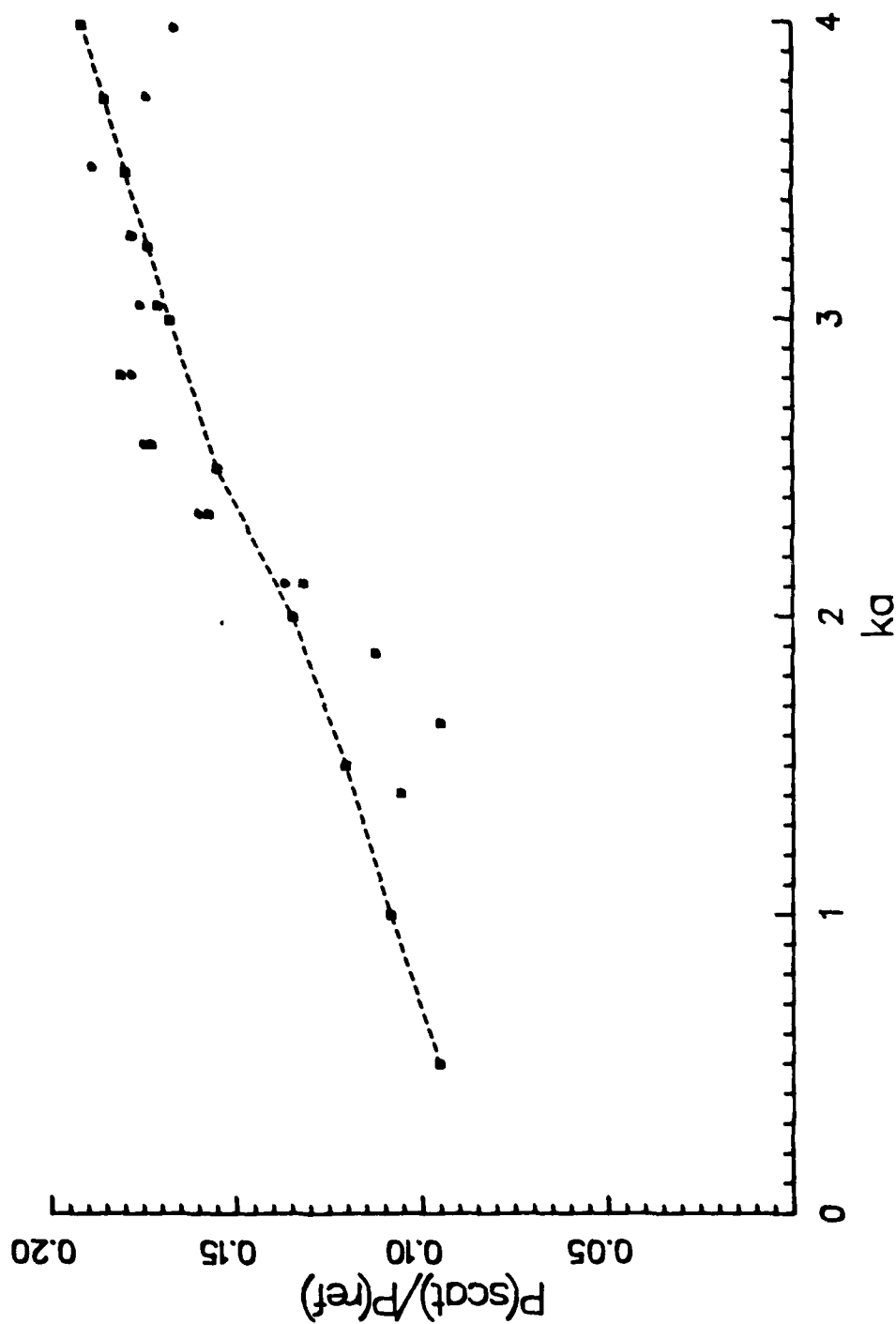


Figure 3-37 Normalized Scattered Pressure Versus  $ka$  for Thick Finite Shell ( $b/a = 9$ ) with Normal Incidence and CHIEF Output for Pressure Release Finite Cylinder (Solid Line is Shell Coated with 0.25 inches of Neoprene, Dashed Line is CHIEF)

normalized scattered pressure for the uncoated shell for  $ka$  values less than 4.0. The larger scattered pressure is partially accounted for by the coated shell being slightly larger, physically than the uncoated shell due to the addition of the .25 inches of neoprene even though the  $ka$  values are adjusted to account for this.

4. For  $ka$  values greater than 6, the normalized scattered pressure of the coated shell shows a significant reduction in structure. It appears that the resonances are averaged to a slowly varying mean value of the uncoated shell's normalized scattered pressure.

5. The experimentally measured normalized scattered pressure for the coated shell is compared with the ideal pressure release scattered pressure calculated by the CHIEF program in figure 3-37 for  $ka$  values less than 4.0. All of the data, with one exception, is within 1 dB of the calculated pressure. The experimental pressure oscillates about the pressure release value indicating the average pressure over the  $ka$  range approximates the pressure release condition. The CHIEF program was run with 480 subdivision and is accurate for a  $ka$  value less than 4. Subdivision schemes necessary for  $ka$  values greater than 4.0 were computer memory and time limited.

## CHAPTER IV

### Conclusions and Recommendations

The primary objective was to determine if a shell, thick or thin, can be made to scatter as a pressure release structure by the application of a viscoelastic coating. In order to achieve this boundary condition, the coating must cause the following effects:

1. The coating must cause the pressure on the surface of the target to be significantly smaller than the incident pressure. The physical results of the significantly smaller surface pressure are that the scattered signal must be inverted relative to the incident signal and the magnitude of the scattered pressure must be equal to the magnitude of the theoretical pressure determined for the pressure release solution.

2. The shell must be acoustically decoupled from the scattering problem, i.e. the resonance effects must be removed and the coating must not exhibit elastic effects of its own.

The secondary objective was to determine how thick the coating must be in order to achieve the primary objective.

In order to determine the thickness of coating required, the viscoelastic constants of the coating materials had to be determined. For the closed cell rubbers the plane wave modulus was determined for the frequency range of 15 kHz to 30 kHz and the Young's modulus for 500 Hz to 3 kHz. The Young's modulus was then extrapolated to higher frequencies in order to estimate the Poisson's ratio and the shear modulus. The Young's modulus extrapolation was not as accurate as had been anticipated based on previous observations for other materials. This inaccuracy resulted in a wide spread for the derived Poisson's ratio, (estimated between 0 and .2), causing a correspondingly wide spread for the complex transverse wave number ( 1.41 to 1.63 times the complex longitudinal wave number). There was no measurable difference in the theoretical form functions determined by the two different values of the transverse wave numbers. This insensitivity of the form function to the variation in the the transverse wave number results from: (1) the phase speed of the closed cell rubber is at least an order of magnitude smaller than the phase speed of either the shell or the surrounding fluid, therefore, the 13% change does not significantly affect the overall speed relationships. (2) the attenuation in the closed cell rubber is very large which results in an almost complete decoupling of the shell. An increase in the attenuation caused by increasing Poisson's ratio from 0 to 0.2 can not decouple the shell further. The experimental and theoretical results are in excellent agreement. The cork-rubber composites were determined to be slightly anisotropic. This anisotropy is small enough not to invalidate the isotropic model. The Poisson's ratio was

estimated to be very small (material properties are dominated by the cork which has a Poisson's ratio of approximately 0). For the corprene, a Poisson's ratio of 0 resulted in excellent agreement of the theory with the experimental results.

For the (infinite) thin shell, the pressure release boundary condition can be achieved by the addition of the .25 inch nitrile coating. The inversion of the specular relative to the incident signal can not be directly attributed to the coating since the shell's form function is in the soft background region for the  $ka$  range of study. For thinner coatings of the nitrile, the pressure release boundary condition can only be achieved at higher  $ka$  values.

The corprene does cause a reduction in the resonance effects, but even at large thicknesses (3.2 cm), the corprene is not as effective as the .635 cm of nitrile. The overall conclusion is that corprene is not a viable pressure release coating for low  $ka$  values.

For the thick (finite) shell, the .25 inch neoprene coating is a fair approximation to the pressure release surface. For both orientations of the target, the neoprene causes the inversion of the specular reflection and a significant suppression of the resonances. The normalized scattered pressure for the axial incidence case is within 2.5 dB of the theoretical pressure release value (mostly greater) as calculated by the SHIP radiation program. For the side incidence case, the normalized scattered pressure is within 1 dB of the pressure release value as calculated by the CHIEF radiation program for  $ka$  valued less than 4.0.

For all the shell measurements performed, the application of the coating significantly increased the amplitude of the scattered pressure relative to the uncoated in the low  $ka$  range. The .25 inches of nitrile added to the thin shell (inner to outer radius ratio of .97) raised the form function 4.5 dB relative to the uncoated shell at a  $ka$  of 2.0. The .25 inch thick neoprene coating increased the normalized scattered pressure of the finite thick (inner to outer radius ratio of .90) shell 8.9 dB relative to the uncoated shell for side incidence at a  $ka$  of 4.0. (There was not a significant change in the magnitude of the normalized scattered pressure of the finite shell for end on incidence indicating that the end caps were scattering as a rigid body.) As the shell becomes thinner, however, the closed cell coatings will actually lower the form function.

All of this data was taken over a frequency range of 15 kHz to 70 kHz. It is not expected that these results would scale well to any other frequency range (typical  $ka$  scaling) because the performance of the coating depends on the size of the air bubbles in the material relative to the acoustic wavelength. The size of the air bubbles in the materials is fixed and therefore, for any other frequency range, the ratio of bubble size to wavelength would change.

The materials in this study are not well suited for deep submergence applications. Corprene has been shown to have an increase in its longitudinal wave speed of 300% due to pressure effects (see Horsely and Thompson<sup>116</sup>). The neoprene closed cell rubber was left under 15 feet of water for several weeks which resulted in an unrecoverable reduction in volume of approximately 50%.

The acoustics community has long considered corprene as the benchmark pressure release material for underwater scattering. This study demonstrates both experimentally and analytically that corprene is, at best, a fair pressure release material and is substantially outperformed by the closed cell rubbers. The tendency of the closed cell rubber to degrade with submergence time (the air leaches out of the rubber) can be prevented by potting the closed cell rubber in a material acoustically matched with the water (i.e rho-c rubber). It is also apparent from this study that the thickness of the shell is an important variable when determining the thickness of the coating required to achieve the pressure release condition (.25 inches of the closed cell rubber decouples the thin shell more efficiently than the thick shell).

The following continuing work is recommended:

1. The development of techniques which would allow the shear modulus to be measured in the frequency range of interest.
2. All theoretical models of the materials which could predict the shear and bulk moduli failed to predict accurate values. A model that allows air concentrations of approximately 80 volume percent is necessary.
3. A numerical computer code that allows the evaluation of the scattering problem for a finite structure that takes into account the elasticity of the viscoelastic coating, the shell and the end caps.



## APPENDIX A

### Derivation of the Scattered Field and Surface Velocity From an Infinite Pressure Release Cylinder for an Incident Plane Wave

In this appendix the scattered pressure from an infinite, pressure release right circular cylinder is determined for a normally incident plane wave. The surface boundary condition (pressure release) defines the acoustic pressure on the surface to be zero; this allows the actual material properties of the cylinder to be neglected. The derivation is general in that the incident plane wave is taken to approach the cylinder at an arbitrary oblique angle,  $\alpha$ , to the center axis of the cylinder (see figure A-1). The solution will be reduced to the special case of interest i.e. normal incidence by setting  $\alpha$  equal to zero.

The governing equation for the region exterior to the cylinder ( $r > a$ ) is the scalar wave equation

$$\nabla^2 P(r, t) = \frac{1}{c^2} \frac{\partial^2 P(r, t)}{\partial t^2} \quad (A-1)$$

A harmonic time dependence,  $\exp(-i\omega t)$ , is assumed which reduces the wave equation to the scalar Helmholtz equation

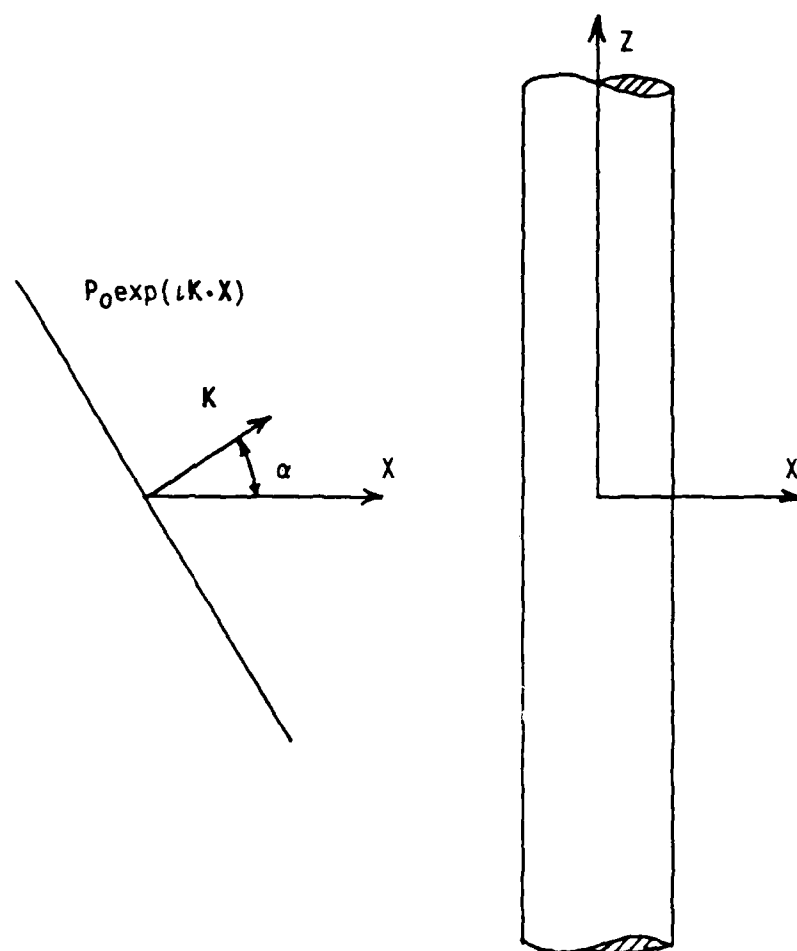


Figure A-1 Geometry for Infinite Pressure Release Cylinder

$$\nabla^2 P(r) + k^2 P(r) = 0 \quad \text{where } k^2 = \frac{\omega^2}{c^2} \quad (\text{A-2})$$

In the previous two equations,  $P(r,t)$  is the total acoustic pressure and consists of the incident pressure,  $P(r,t)_{\text{inc}}$ , and scattered pressure,  $P(r,t)_s$ . The acoustic wave speed of the exterior fluid medium (water) is denoted by  $c$ . In the Helmholtz equation, the time dependence is suppressed. In order to determine the form of the scattered pressure, the Helmholtz equation for the geometry of interest (right circular cylinder) must be investigated. For the infinite right circular cylinder, the Helmholtz equation is separable. The pressure is assumed to be of the form

$$P(r, \theta, z) = R(r) \theta(\theta) Z(z) \quad (\text{A-3})$$

where  $r, \theta$ , and  $z$  are the standard cylindrical coordinates. The Helmholtz equation becomes

$$\frac{1}{Rr} \frac{d}{dr} \left( r \frac{dR}{dr} \right) + \frac{1}{\theta r^2} \frac{d^2 \theta}{d\theta^2} + \frac{1}{Z} \frac{d^2 Z}{dz^2} = 0 \quad (\text{A-4})$$

After applying the separation of variables technique, the following three equations result

$$\frac{1}{r} \frac{d}{dr} \left( r \frac{dR}{dr} \right) + \left( k_r^2 - \frac{m^2}{r^2} \right) R = 0 \quad (\text{A-5a})$$

$$\frac{d^2\theta}{d\theta^2} + m^2\theta = 0 \quad (\text{A-5b})$$

$$\frac{d^2Z}{dz^2} + k_z^2 Z = 0 \quad (\text{A-5c})$$

$$k^2 = \frac{\omega^2}{c^2} = k_r^2 + k_z^2 \quad \text{where} \quad \left[ k_r = \frac{\omega}{c} \cos(\alpha) \text{ and } k_z = \frac{\omega}{c} \sin(\alpha) \right]$$

The general solution for the radial equation,  $R(r)$ , is a combination of Bessel functions of the first and second kind (or Hankel functions of the first and second kind). The solution for  $\theta(\theta)$  is  $\cos(m\theta)$  and  $\sin(m\theta)$ , where  $m$  must be an integer for the solution to be continuous at  $\theta = 0 = 2\pi$ . Due to the symmetry, the  $\theta$  function must be even with respect to the  $\theta = 0$  which eliminates the  $\sin(m\theta)$  form. The general solution for  $Z$  is a combination of  $\exp(-ik_z z)$  and  $\exp(ik_z z)$ . The second solution of  $Z$  is eliminated by requiring the solution to be finite as  $z$  approaches infinity.

For the scattering problem, the incident wave can be written

$$P_{\text{inc}}(r, \theta, z) = P_0 \exp(-ik \cdot r) = P_0 \exp(-ikz) \sum_{m=0}^{\infty} i^m \epsilon_m \cos(m\theta) J_m(k_r r)$$

(A-6)

where  $\epsilon_m$  is the Neuman factor ( $\epsilon_m = 1$  for  $m = 0$  and  $\epsilon_m = 2$  for  $m > 0$ ),  $J_m(k_r r)$  is the cylindrical Bessel function of the first kind, and  $k$  is the wave propagation vector.

The total pressure is the sum of the incident pressure and the scattered pressure. The scattered pressure is assumed to be of the form

$$P_s(r, \theta, z) = P_0 \exp(-ik_z z) \sum_{m=0}^{\infty} i^m \epsilon_m \cos(m\theta) A_m H_m^1(k_r r) \quad (A-7)$$

In order to determine the constant  $A_m$ , the pressure release surface boundary condition is employed.

$$\begin{aligned} P_{\text{total}}(a, \theta, z) &= P_0 \exp(-ik_z z) \sum_{m=0}^{\infty} i^m \epsilon_m \cos(m\theta) (A_m H_m^1(k_r a) + J_m(k_r a)) \\ &= 0 \end{aligned} \quad (A-8)$$

The orthogonality of the cosine function is utilized by multiplying equation (A-8) by  $\cos(n\theta)$  and integrating with respect to  $\theta$  for  $\theta$  between 0 and  $2\pi$ .

$$P_0 \exp(-ik_z z) \sum_{m=0}^{\infty} i^m \epsilon_m \left[ A_m H_m^1(k_r a) + J_m(k_r a) \right] \int_0^{2\pi} \cos(m\theta) \cos(n\theta) d\theta = 0 \quad (A-9)$$

After simplification, the constant  $A_m$  is determined to be

$$A_m = - \frac{J_m(k_r a)}{H_m^1(k_r a)} \quad (A-10)$$

The total pressure is determined by substituting equation (A-10) into equation (A-7).

$$P_{\text{total}}(r, \theta, z) = P_0 \exp(-ik_z z) \sum_{m=0}^{\infty} \epsilon_m \cos(m\theta) \left[ J_m(k_r a) - \frac{J_m(k_r a)}{H_m^1(k_r a)} H_m^1(k_r r) \right] \quad (A-11)$$

The actual quantities of interest are the radial surface velocity and the far-field scattered pressure for the normally incident ( $\alpha = 0$ ) plane wave. The normal incidence condition removes the  $z$  dependence from the solution since  $k_z = 0$  and  $k_r$  becomes equal to  $k = \omega/c$ . The radial component of the velocity follows from Euler's equation

$$\nabla P(r, \theta, t) = \frac{\partial P}{\partial r} \mathbf{e}_r + \frac{\partial P}{\partial \theta} \mathbf{e}_\theta = -\rho \frac{\partial \mathbf{V}}{\partial t} = -\rho(-i\omega) \left[ V_r \mathbf{e}_r + V_\theta \mathbf{e}_\theta \right]$$

$$\text{the radial velocity becomes } V_r = \frac{-i}{\rho k c} \frac{\partial P}{\partial r} \quad (A-12)$$

Substituting equation (A-11) for the total pressure,  $P$ , then  $V_r$  becomes

$$V_r(a, \theta) = \frac{-P_0}{\rho c} \sum_{m=0}^{\infty} \epsilon_m \cos(m\theta) \left[ \frac{d}{d(ka)} J_m(ka) - \frac{J_m(ka)}{H_m^1(ka)} \frac{d}{d(ka)} H_m^1(ka) \right] \quad (A-13)$$

The surface velocity, equation (A-13), is simplified by using the Wronskian formula

$$W(J, H) = H_m^1(ka) \frac{d}{d(ka)} J_m(ka) - J_m(ka) \frac{d}{d(ka)} H_m^1(ka) = -\frac{2}{\pi ka} \quad (A-14)$$

the surface velocity becomes

$$V_r(a, \theta) = \frac{-P_0}{\rho c} \sum_{m=0}^{\infty} \epsilon_m \cos(m\theta) \frac{2}{\pi ka} \frac{1}{H_m^1(ka)} \quad (A-15)$$

The scattered pressure is derived by subtracting the incident pressure from the total pressure yielding

$$P_S(a, \theta) = P_0 \sum_{m=0}^{\infty} \epsilon_m \cos(m\theta) \left( - \frac{J_m(ka)}{H_m^1(ka)} H_m^1(kr) \right) \quad (A-16)$$

The general form for the nondimensional, normalized far field pressure is

$$\frac{P(r, \theta)}{P_0 \sqrt{\frac{a}{2r}} e^{ikr}} = \text{Function}(ka, \theta) \quad (A-17)$$

The far-field scattered pressure is obtained by taking the limit of the Hankel function as the argument asymptotically approaches infinity in equation (A-16). In Arfken<sup>117</sup>, the asymptotic form of the Hankel function of the first kind is shown to be

$$H_m^1(\xi) = \sqrt{\frac{2}{\pi\xi}} e^{i(\xi - (m + \frac{1}{2}) \frac{\pi}{2})} (P_m(\xi) + i Q_m(\xi)) \quad (A-17)$$

for  $-\pi < \arg(\xi) < 2\pi$  (for this particular derivation  $\xi$  is real and  $\arg(\xi)=0$ )

$$\text{where } P_m(\xi) = 1 - \frac{4m^2 - 1}{128\xi^2} + \text{order} \left[ \xi^{-4} \right] \quad (A-18)$$

$$Q_m(\xi) = \frac{4m^2 - 1}{8\xi} - \text{order} \left[ \xi^{-3} \right]$$



In the limit as  $\xi \rightarrow \infty$ ,  $P_m(\xi) \rightarrow 1$  and  $Q_m(\xi) \rightarrow 0$  resulting in

$$H_m^1(\xi) = \left\{ \sqrt{\frac{2}{\pi\xi}} e^{i\xi} \right\} e^{-i(m + \frac{1}{2}) \frac{\pi}{2}} \quad (A-19)$$

The normalized far-field scattered pressure becomes

$$\frac{P_s(r, \theta)}{P_0 \sqrt{\frac{a}{r}} e^{-i k r}} = - \sum_{m=0}^{\infty} i^m \epsilon_m \cos(m\theta) \frac{J_m(ka)}{H_m^1(ka)} \sqrt{\frac{2}{\pi ka}} \exp \left[ -i \left( m + \frac{1}{2} \right) \frac{\pi}{2} \right] \quad (A-20)$$

The far field cylindrical form function is defined to be the square root of 2 times the magnitude of equation (A-20).

$$f_{\infty}(\theta) = \sqrt{\frac{2r}{a}} \left| \frac{P_s(r, \theta)}{P_0} \right| \quad (A-21)$$

The right side of the equation (A-20) is numerically calculated. The Bessel functions are calculated using the recurrence and normalization methods described in Abramowitz and Stegun<sup>118</sup> and Hitchcock<sup>119</sup>. Satisfactory verification of the Bessel functions with published tables for test arguments was obtained. (The method is also valid for Bessel functions of complex arguments which are required

in Appendix C.) The infinite series is terminated when the ratio of the next term in the series to the total sum is less than  $10^{-6}$ .

### Determination of the Low Frequency Limit

Only the first term of the series of equation (A-20) needs to be retained in order to determine the low frequency limit of the normalized scattered pressure.

The normalized backscattered ( $\theta = \pi$ ) pressure is approximated as

$$\frac{P_s(r, \theta)}{P_0 \int \frac{a}{r} e^{i k r}} = \lim_{ka \rightarrow 0} \left\{ \frac{J_0(ka)}{H_0^1(ka)} \sqrt{\frac{2}{\pi ka}} e^{i \frac{\pi}{2}} \right\} \quad (\text{A-22})$$

where the  $\lim_{ka \rightarrow 0} J_0(ka) = 1$  and where the

$$\lim_{ka \rightarrow 0} N_0(ka) = \frac{2}{\pi} \left\{ \ln \left( \frac{ka}{2} \right) + \gamma \right\} \quad (\gamma \text{ is Euler's constant})$$

The far-field backscattered cylindrical form function becomes

$$f_{\infty}(\theta=\pi) = \frac{\sqrt{2}}{1 + \frac{2i}{\pi} \left\{ \ln \left( \frac{ka}{2} \right) + \gamma \right\}} \quad (\text{A-23})$$

### Determination of the High Frequency Limit or Specular Reflection

The following specular reflection derivation for the cylinder parallels the derivation for the sphere in Urick<sup>120</sup>. There are four basic assumptions required for this method:

1. the scatterer is perfect in shape,
2. the magnitude of the reflection coefficient equal to unity,
3. the scatterer is immovable,
4. the radii of curvature of the scatterer is larger compared to the acoustic wavelength ( $ka \gg 1$ ).

The approach of this method is to relate the energy contained in a small acoustic beam which is incident on a small area,  $dS$ , of the curved surface to the spreading of that incident energy upon reflection at a unit distance. For this derivation, the cylinder is considered to be infinite with the center axis normal to the wave propagation vector. The radius of the cylinder is  $a$ .

As shown in Urick, the acoustic center,  $Q$ , is located a distance of  $a/2$  from the geometric center,  $C$ . If the waves were to penetrate the surface, they would be focused at the acoustic center,  $Q$ . Upon reflection from the surface area, the reflected waves appear to originate from a line source located at the acoustic center,  $Q$ . The specular reflection far-field form function reduces to the constant value of 1.0.

$$f_{\infty} = \frac{P_s(r, \theta)}{P_0 \sqrt{\frac{a}{2r}}} = \sqrt{\frac{1}{2}} \cdot \sqrt{2} = 1.0 \quad (\text{A-26})$$

The normalized far-field backscattered form function as a function of  $ka$  is plotted in figure (A-2). Figure (A-2) shows the backscattered pressure rapidly approaches the geometrical limit and is within 5 percent of that limit by a  $ka$  of approximately 6. For the low frequency limit, the backscattered pressure is within 1 percent of the low frequency limit at a  $ka$  of approximately .09.

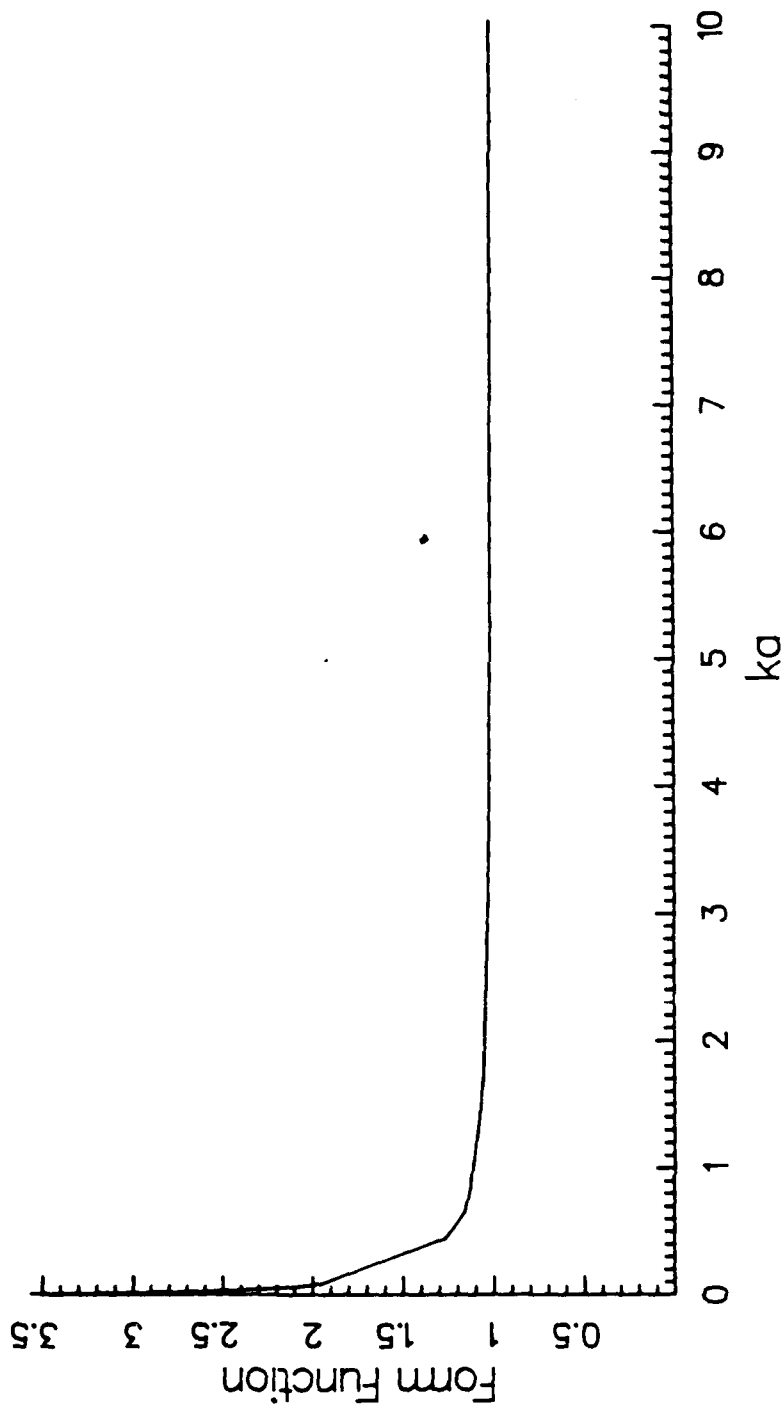


Figure A-2 Pressure Release Infinite Cylinder

## APPENDIX B

### Pressure Release Sphere

The solution for the scattered far-field pressure of the ideal pressure release sphere follows the standard approach of expressing the field pressure as an infinite series of spherical harmonics and solving for the series coefficients. The geometry of the problem is illustrated in figure B-1 where the incoming plane wave is traveling in the +Z direction. Standard spherical coordinates are used. Due to the symmetry of the problem, the solution is independent of  $\phi$ . The  $\exp(-i\omega t)$  time dependence is suppressed.

The spherical harmonic expression for the incident plane wave traveling along the polar axis is

$$p_{inc}(\theta, \phi) = p_0 \sum_{m=0}^{\infty} (2m + 1) i^m P_m(\cos\theta) j_m(kr) \quad (B-1)$$

where  $P_m(\cos\theta)$  is the Legendre polynomial of order  $m$  and  $j_m(kr)$  is the spherical Bessel function of the first kind of order  $m$ .

The total pressure,  $p_{tot}$ , is the sum of the incident pressure,  $p_{inc}$ , and the scattered pressure,  $p_{scat}$ .

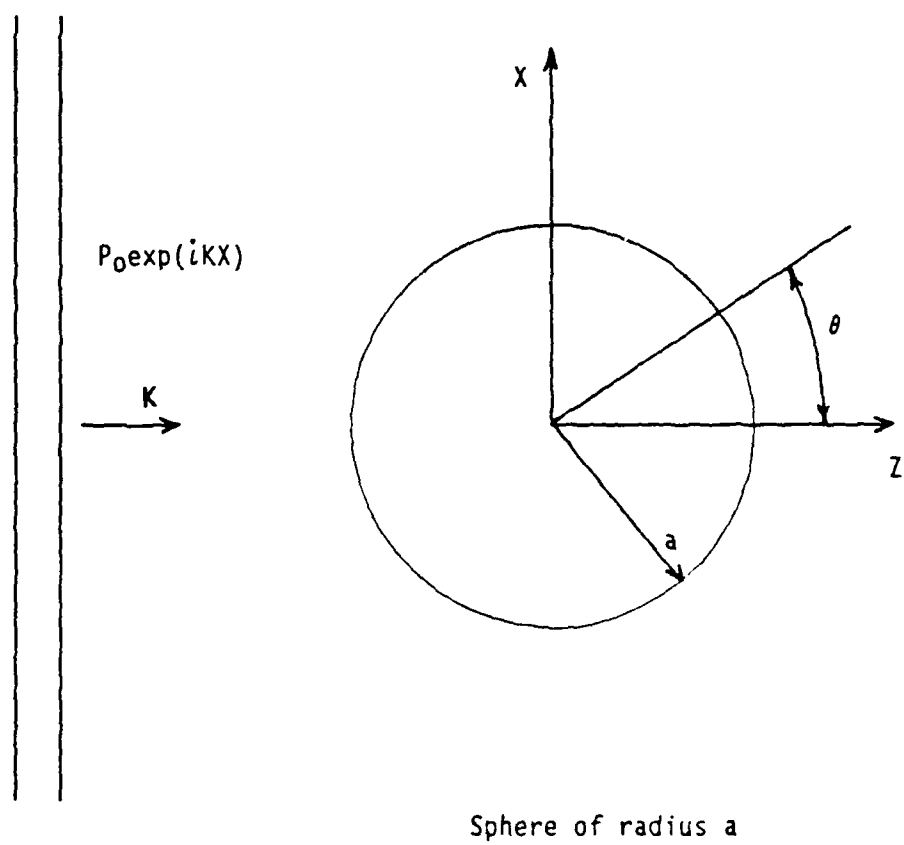


Figure B-1 Geometry for Pressure Release Sphere

$$p_{\text{tot}}(r, \theta, \phi) = p_{\text{inc}}(r, \theta, \phi) + p_{\text{scat}}(r, \theta, \phi) \quad (\text{B-2})$$

The scattered pressure can be expressed as the following general spherical harmonic infinite series

$$p_{\text{scat}}(r, \theta, \phi) = \sum_{m=0}^{\infty} \sum_{n=0}^m Y_{m,n}^{\sigma}(\theta, \phi) q_{m,n}^{\sigma}(kr) \quad \text{where } \sigma \text{ is } +1 \text{ or } -1 \quad (\text{B-3})$$

and  $Y_{m,n}^{\sigma}(\theta, \phi)$  is the spherical harmonic and  $q_{m,n}^{\sigma}(kr)$  is a combination of  $j_m(kr)$  and  $h_m^{\sigma}(kr)$  which are determined from the boundary conditions. Since the problem is independent of  $\phi$ ,  $Y_{m,n}^{\sigma}(\theta, \phi)$  reduces to  $P_m(\cos\theta)$ . The pressure release condition causes the incident wave to be completely reflected resulting in only an outward traveling scattered wave.

$$q_{m,n}^{\sigma}(kr) = h_m^1(kr) \quad (\text{B-4})$$

With simplification, the scattered pressure becomes

$$p_{\text{scat}}(r, \theta) = \sum_{m=0}^{\infty} A_m P_m(\cos\theta) h_m^1(kr) \quad (\text{B-5})$$



The total surface pressure is zero and with the substitution of equations (B-1) and (B-5), equation (B-2) becomes

$$0 = \sum_{m=0}^{\infty} p_0 (2m + 1) \epsilon^m P_m(\cos\theta) j_m(ka) + A_m P_m(\cos\theta) h_m^1(ka) \quad (B-6)$$

In order to determine the constants  $A_m$ , the orthogonality property of the Legendre polynomial is utilized by multiplying equation (B-6) by  $P_n(\cos\theta)$  and integrating with respect to  $d(\cos\theta)$  from -1 to 1.

$$0 = \sum_{m=0}^{\infty} \left[ p_0 (2m + 1) \epsilon^m j_m(ka) + A_m h_m^1(ka) \right] \int_{-1}^1 P_m(\cos\theta) P_n(\cos\theta) d(\cos\theta) \quad (B-7)$$

Simplification yields the series constant

$$A_m = - \frac{p_0 \epsilon^m (2m + 1) j_m(ka)}{h_m^1(ka)} \quad (B-8)$$

Substitution of equation (B-8) into expression for the scattered pressure, equation (B-5), results in

$$p_{\text{scat}}(r, \theta) = \sum_{m=0}^{\infty} \frac{-p_0 \iota^m (2m+1) j_m(ka)}{h_m^1(ka)} P_m(\cos \theta) h_m^1(kr) \quad (\text{B-9})$$

The far-field scattered pressure is obtained by utilizing the asymptotic form of the spherical Hankel function for the argument approaching infinity

$$\lim_{z \rightarrow \infty} h_m^1(z) = (-\iota)^{m+1} \frac{e^{\iota z}}{z} \quad (\text{B-10})$$

In addition, the far-field scattered pressure should be of the standard form

$$p_{\text{ff}}(r, \theta) = p_0 \left( \frac{a}{r} \right) f(ka, \theta) e^{\iota kr} \quad (\text{B-11})$$

where  $f(ka, \theta)$  is the far-field spherical form function. The resulting normalized far-field scattered pressure is

$$\frac{p_{\text{scat}}(r, \theta)}{p_0 \left( \frac{a}{r} \right) \exp(\iota kr)} = \sum_{m=0}^{\infty} \iota \frac{(2m+1) j_m(ka)}{ka h_m^1(ka)} P_m(\cos \theta). \quad (\text{B-12})$$

## APPENDIX C

### Modification of the Naval Ocean Systems Center (NOSC) CHIEF Program

With NOSC Technical Document 970<sup>74</sup>, Benthein and Barach released a modern fortran program to compute the acoustic radiation from an arbitrary-shaped body using the CHIEF method developed by Schenck<sup>71</sup>. The radiation program computes both the near-field and far-field pressures of a closed surface,  $S$ , provided the normal surface velocity distribution is known. In particular, the program first calculates the unknown surface pressure by solving the surface Helmholtz integral equation

$$2\pi P(x) = \iint_S P(\sigma) \frac{\partial}{\partial n_\sigma} \left[ \frac{e^{-ikr(x,\sigma)}}{r(x,\sigma)} \right] + i\omega\rho V(\sigma) \frac{e^{ikr(x,\sigma)}}{r(x,\sigma)} dS(\sigma) \quad (C-1)$$

The integral is solved numerically by subdividing the surface into  $N_s$  subregions and assuming that the surface pressures and normal velocities are constant in each subregion. The result of this approximation is a system of linear algebraic equations. The algebraic equations are generated from the following

$$\begin{aligned}
 2\pi P_m(x) - \sum_{n=1}^{N_S} P_n \iint_{S_n} \frac{\partial}{\partial n_\sigma} \left( \frac{\exp(-\iota k r(\xi_m, \sigma))}{r(\xi_m, \sigma)} \right) dS(\sigma) = \\
 \iota \omega \rho \sum_{n=1}^{N_S} V_n \iint_{S_n} \left( \frac{\exp(-\iota k r(\xi_m, \sigma))}{r(\xi_m, \sigma)} \right) dS(\sigma) \quad (C-2)
 \end{aligned}$$

$m = 1, \dots, N_n$

where  $\xi_m$  is some reference point on  $S_m$ . In matrix notation the previous equation can be written as

$$A p = B v \quad (C-3)$$

where

$$\begin{aligned}
 A_{mn} &= 2\pi \delta_{mn} - \iint_S \frac{\partial}{\partial n_\sigma} \left( \frac{e^{-\iota k r(\xi_m, \sigma)}}{r(\xi_m, \sigma)} \right) dS(\sigma) \\
 B_{mn} &= \iota \omega \rho \iint_{S_n} \left( \frac{e^{-\iota k r(\xi_m, \sigma)}}{r(\xi_m, \sigma)} \right) dS(\sigma) \quad (C-4)
 \end{aligned}$$

and  $p = (P_m)$  and  $v = (V_m)$  are vector of the surface pressure and surface velocities respectively. The surface integrals in A and B are solved by Gaussian

quadrature. Matrix equation (C-3) does not yield a unique solution at certain characteristic frequencies. The CHIEF method overcomes this uniqueness problem by forcing additional constraints on the surface pressure. In particular, the interior Helmholtz equation must also be satisfied by the surface pressures and velocities for interior locations at all frequencies. This program allows interior points of  $S$  to be input which are related by

$$\iint_S p(\sigma) \frac{\partial}{\partial n_\sigma} \left( \frac{e^{-\iota k r(x, \sigma)}}{r(x, \sigma)} \right) + \iota \omega \rho v(\sigma) \frac{e^{\iota k r(x, \sigma)}}{r(x, \sigma)} dS(\sigma) \quad (C-5)$$

$m = N_s + 1, \dots, N_s + N_i$  where  $N_i$  is the number of interior points.

Equation (C-3) is still valid but with the coefficients modified to

$$A_{mn} = \begin{cases} 2\pi\delta_{mn} - \iint_S \frac{\partial}{\partial n_\sigma} \left( \frac{e^{-\iota k r(\xi_m, \sigma)}}{r(\xi_m, \sigma)} \right) dS(\sigma) & m = 1 \text{ to } N_s \\ \iint_S \frac{\partial}{\partial n_\sigma} \left( \frac{e^{-\iota k r(x_m, \sigma)}}{r(x_m, \sigma)} \right) dS(\sigma) & m = N_s + 1 \text{ to } N_s + N_i \end{cases}$$

$$B_{mn} = \begin{cases} \iota \omega \rho \iint_{S_n} \left( \frac{e^{-\iota k r(\xi_m, \sigma)}}{r(\xi_m, \sigma)} \right) dS(\sigma) & m = 1 \text{ to } N_s \\ \iota \omega \rho \iint_{S_n} \left( \frac{e^{-\iota k r(x_m, \sigma)}}{r(x_m, \sigma)} \right) dS(\sigma) & m = N_s + 1 \text{ to } N_s + N_i \end{cases} \quad (C-6)$$

The matrix equation is now overdetermined and solved by the Householder reduction technique. Once the surface pressure is determined, the exterior Helmholtz equation is used to determine the field pressure.

$$\begin{aligned}
 P(x) = & \frac{1}{4\pi} \sum_{n=1}^{N_n} P_n \iint_{S_n} \frac{\partial}{\partial n_\sigma} \left( \frac{\exp(-ikr(x,\sigma))}{r(x,\sigma)} \right) dS(\sigma) \\
 & + \frac{i\omega\rho}{4\pi} \sum_{n=1}^{N_n} V_n \iint_{S_n} \left( \frac{\exp(-ikr(x,\sigma))}{r(x,\sigma)} \right) dS(\sigma) \quad (C-7)
 \end{aligned}$$

The previous discussion is a summary of the methodology used in the program developed by Benthein and Barach with considerable more detail contained in NOSC TD 970<sup>74</sup>.

The objective of the appendix is to modify this program to determine the scattered pressure field from a plane wave incident ( $P_{inc}$ ) on a pressure release surface. Unlike the radiation program, the surface pressure is initially defined to be zero with the normal surface velocity to be determined.

The scattering version of the Helmholtz integral is still applicable.

$$4\pi P(x) = \iint_S P(\sigma) \frac{\partial}{\partial n_\sigma} \left( \frac{e^{-ikr(x,\sigma)}}{r(x,\sigma)} \right) + i\omega\rho V(\sigma) \frac{e^{ikr(x,\sigma)}}{r(x,\sigma)} dS + 4\pi P_{inc}(x) \quad (C-8)$$

Since  $P(x)$  is defined to be zero on the surface, the equation (C-8) reduces to

$$P_{inc}(x) = -\frac{1}{4\pi} \iint_S i\omega\rho V(\sigma) \frac{e^{ikr(x,\sigma)}}{r(x,\sigma)} dS(\sigma) \quad (C-9)$$

The surface geometry and surface subdivision sections of the the CHIEF program are utilized to define the surface. The incident pressure is calculated at the center of each subdivision by  $\exp(-ikX_3)$  assuming the plane wave is traveling in the  $+X_3$  direction (this program assumes an  $\exp(i\omega t)$  time dependence). Matrix equation (C-3) reduces to

$$B v = - P_{inc} \quad (C-10)$$

from which the normal surface velocities are determined by a standard equation solver subroutine. The difficulty of characteristic frequencies still exists but matrix equation (C-10) may be overdetermined in a similar manner to the radiation problem. Once the normal surface velocities are known, the field pressure portions of the CHIEF program are utilized, with the surface pressures set to zero, to compute the scattered field. The scattered far field pressure is computed from

$$P_{ff}(x) = \frac{\frac{P(x)}{4\pi R}}{\frac{\exp(\pm kR)}{4\pi R}} = \sum_{n=1}^{N_s} V_n B_{ff}(x, n) \quad (C-11)$$

where  $B_{ff}$  is the far-field version of  $B$ .

Verification of the program modification is only expeditiously possible for two closed pressure release surfaces, i.e. the sphere and the finite cylinder. An exact analytical solution is available for scattering from the pressure release sphere and is contained in Appendix B. The finite pressure release cylinder with an axially incident plane wave can be compared to the proven solution generated by SHIP<sup>82</sup>.

The scattering geometry for the pressure release sphere is illustrated in figure (C-1). The surface is divided into a total of 144 subdivisions with 12 equiangular divisions in both the theta and phi coordinates. If the usual rule-of-thumb of 10 subdivisions per wavelength is used, this subdivision scheme is anticipated to be accurate up to a  $ka$  of 2.5. Due to symmetry, the field is only dependent on the  $r$  and theta coordinates. The analytical solution for the far-field pressure is

$$\frac{\frac{P(r, \theta)}{P_0}}{\frac{\exp(-\pm kR)}{4\pi R}} = \sum_{m=0}^{N_s} \frac{-\pm(2m+1) j_m(ka)}{h_m^1(ka)} P_m(\cos(\theta)) \quad (C-12)$$

where  $P_m(\cos(\theta))$  is the Legendre polynomial of order  $m$ .



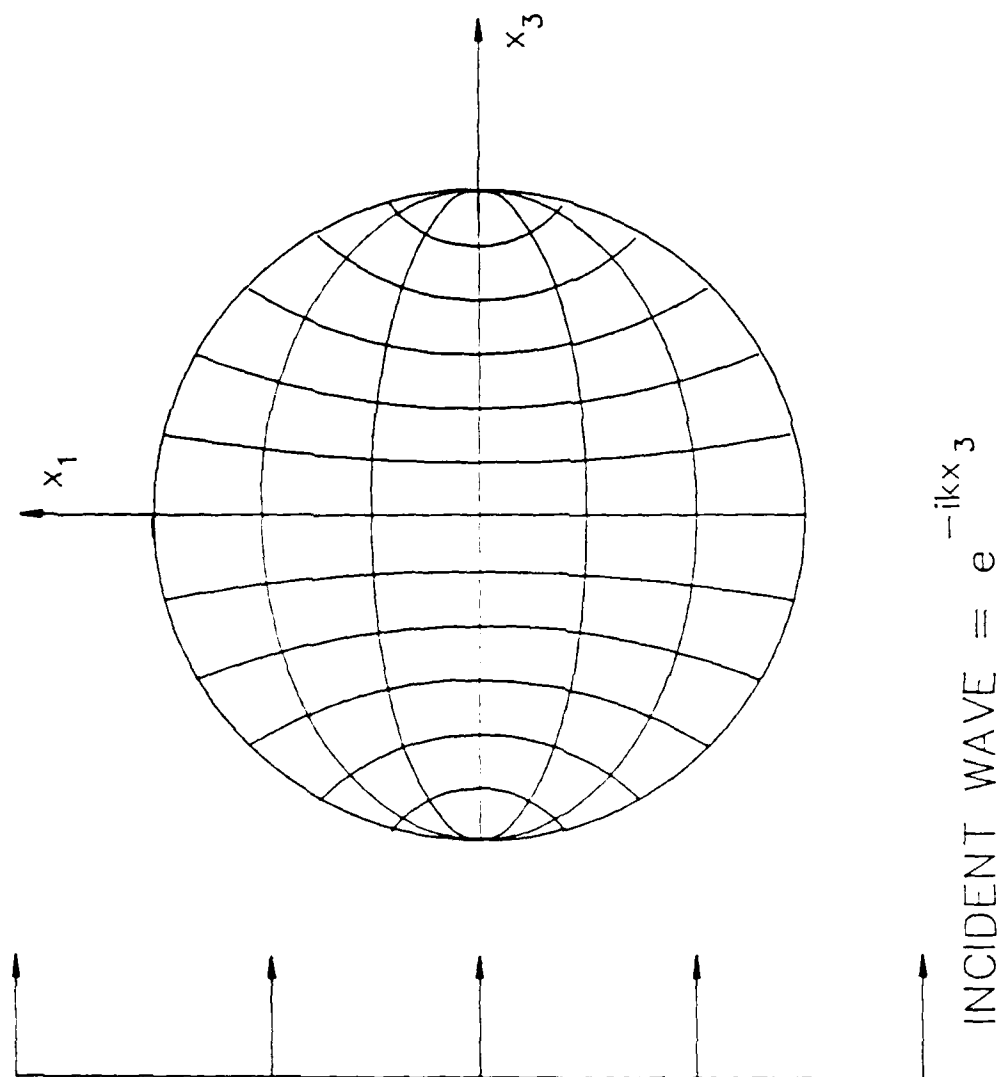


Figure C-1 Scattering Geometry and Subdivision Scheme for Pressure Release Sphere

A comparison between the program and analytical solutions of the normalized far-field pressures for  $ka$  between 1.0 and 4.0 is tabulated below.

Table C-1

## Comparison of CHIEF Results for Pressure Release Sphere

$ka$	<u>Program Solution</u>		<u>Analytical Solution</u>	
	<u>Real</u>	<u>Imaginary</u>	<u>Real</u>	<u>Imaginary</u>
1.0	-.547	-8.69E-2	-.544	-8.72E-2
1.5	-.205	-.535	-.204	-.533
2.0	.333	-.424	.332	-.422
2.5	.533	6.93E-2	.528	6.95E-2
3.0	.220	.478	.216	.475
3.5	-.295	.428	-.291	.429
4.0	-.523	-4.56E-2	-.515	-1.69E-2
4.5	-.247	-.534	-.256	-.443

$ka$	<u>Program Magnitude</u>	<u>Analytical Solution Magnitude</u>	<u>Error(%)</u>
1.0	.581	.580	0.20
1.5	.573	.571	0.35
2.0	.539	.537	0.37
2.5	.537	.533	0.75
3.0	.527	.522	0.96
3.5	.520	.518	0.39
4.0	.525	.514	2.14
4.5	.589	.512	15.04

The pressure release program is accurate to within 1 percent over the  $ka$  range of 1.0 to 4.0. The results are somewhat surprising in that accurate results are obtained up to a  $ka$  value of 4.0 (less than 10% error) which results in approximately six subdivision per wavelength. There are no indications that the two solutions would not match at larger  $ka$  values provided the number of subdivisions was appropriately increased.

The cylinder verification is for the plane wave traveling in the  $-Z$  direction and incident on the flat ends of the cylinder. The subdivision scheme was to divide the top into three circumferential rings of equal radial dimension. Each ring was also divided into six equiangular sections in the  $\theta$  direction. The bottom end was partitioned in a similar manner. The side of the cylinder was divided into six equal sections in the axial direction and six equiangular sections in the  $\theta$  direction for a total 72 side subdivisions (see figure (C-2)). For the SHIP solution, the top and bottom ends of the cylinder were divided into 3 circumferential rings of equal radial dimension. The side of the cylinder was divided into six equal circumferential rings in the axial direction. Due to the symmetry of the problem, the subdivision schemes are equivalent. As with the pressure release sphere, the anticipated accuracy is up to a  $ka$  of 2.5. The results are tabulated for normalized surface velocity in each of the rings for  $ka = 0.5, 1.0$  and  $2.0$ .

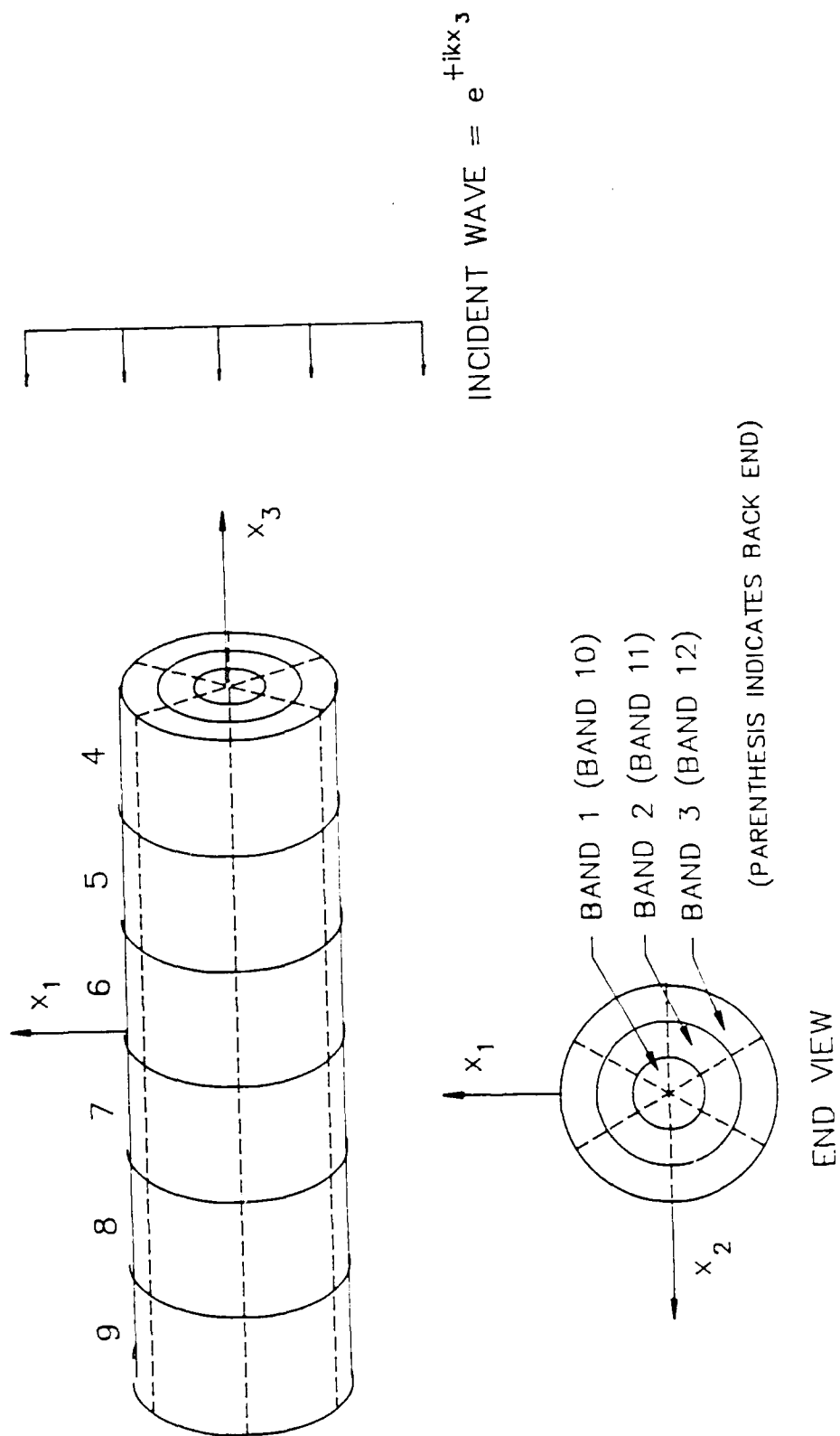


Figure C-2 Scattering Geometry and Subdivision Scheme for Pressure Release Finite Cylinder

Table C-2

Comparison of CHIEF Program With SHIP Program

<u>ka = 0.</u>	<u>Pressure Release Program</u>	<u>SHIP</u>
<u>Band</u>	<u>Real Velocity (x10<sup>-6</sup>)</u>	<u>Real Velocity (x10<sup>-6</sup>)</u>
1	-1.207	-1.203
2	-1.254	-1.256
3	-1.806	-1.808
4	-2.226	-2.219
5	-0.9588	-0.9593
6	-0.6741	-0.6740
7	-0.4270	-0.4269
8	-0.1997	-0.1994
9	0.2568	0.2554
10	0.5964	0.5968
11	0.5193	0.5197
12	0.5199	0.5178
<u>Band</u>	<u>Imaginary Velocity (x10<sup>-6</sup>)</u>	<u>Imaginary Velocity (x10<sup>-6</sup>)</u>
1	0.4213	0.4207
2	0.4854	0.4869
3	0.9919	0.9953
4	1.995	1.991
5	1.279	1.280
6	1.248	1.249
7	1.253	1.254
8	1.296	1.296
9	2.049	2.046
10	1.046	1.050
11	0.5266	0.5281
12	0.4618	0.4610

ka = 1.Pressure Release ProgramSHIP

<u>Band</u>	<u>Real Velocity (x10-6)Real</u>	<u>Velocity (x10-6)</u>
1	-1.033	-1.030
2	-1.081	-1.082
3	-1.595	-1.597
4	-2.040	-2.034
5	-0.8935	-0.8941
6	-0.6263	-0.6263
7	-0.3906	-0.3905
8	-0.1750	-0.1758
9	0.2171	0.2159
10	0.4387	0.4392
11	0.3467	0.3472
12	0.3350	0.3338

<u>Band</u>	<u>Imaginary Velocity (x10-6)</u>	<u>Imaginary Velocity (x10-6)</u>
1	-0.2564	-0.2545
2	-0.2099	-0.2092
3	0.0132	0.0151
4	0.7538	0.7537
5	0.6674	0.6676
6	0.7140	0.7141
7	0.7416	0.7516
8	0.7523	0.7525
9	1.036	1.035
10	0.3033	0.3049
11	0.0171	0.0176
12	-0.0303	-0.0297

ka = 2.0Pressure Release ProgramSHIP

<u>Band</u>	<u>Real Velocity (x10-7)</u>	<u>Real Velocity (x10-7)</u>
1	-5.538	-5.529
2	-6.100	-6.115
3	-10.606	-10.633
4	-16.442	-16.402
5	-7.709	-7.714
6	-5.215	-5.216
7	-2.777	-2.779
8	-0.534	-0.535
9	3.075	3.063
10	2.126	2.131
11	0.318	0.319
12	-0.178	-0.175

<u>Band</u>	<u>Imaginary Velocity (x10-7)</u>	<u>Imaginary Velocity (x10-7)</u>
1	-9.867	-9.823
2	-9.346	-9.348
3	-9.135	-9.127
4	-2.315	-2.285
5	2.853	2.851
6	4.439	4.439
7	5.213	5.212
8	5.230	5.229
9	5.587	5.583
10	-0.1290	-0.1216
11	-1.395	-1.398
12	-1.544	-1.541

## APPENDIX D

### Scattering From the Coated Infinite Cylinder

In this appendix, the solution for the far-field scattered pressure from an infinite, hollow elastic cylinder coated with a viscoelastic solid is derived. The elastic cylinder is considered lossless whereas the losses in the viscoelastic solid will be accounted for by employing a complex wave number. The method of approach is to formulate the displacement potentials for the hollow, infinite elastic cylinder for an arbitrary incident plane wave and reduce this solution for the normal incidence case. This result will then be extended to the layer problem. This solution is applicable to all layer and wall thicknesses since no shell approximations are utilized.

### Scattering From an Infinite Elastic Cylinder With Arbitrary Incidence

The geometry for the elastic cylinder is shown in figure D-1 where  $\gamma$  is the angle of incidence referenced to the Z axis. In the elastic solid, the displacement equation of motion for no body forces is



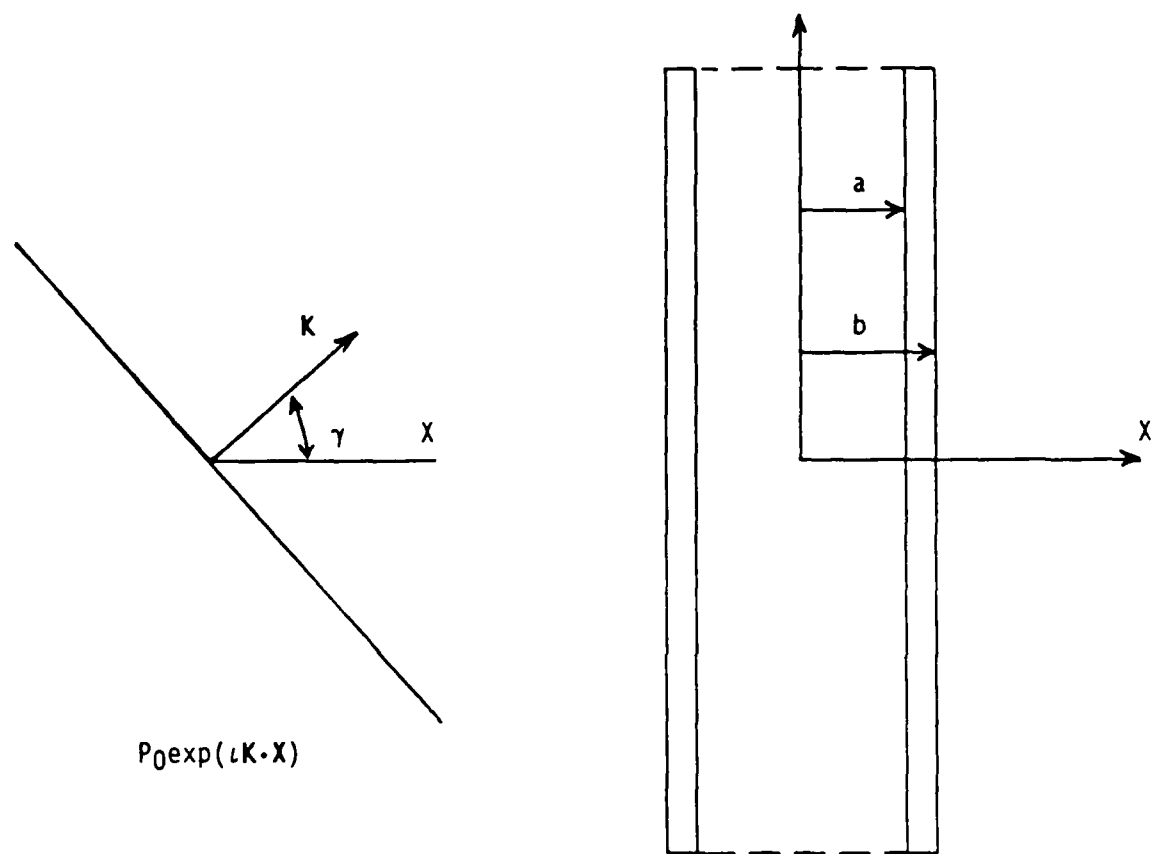


Figure D-1 Scattering Geometry for Infinite Cylindrical Shell

$$\mu \nabla^2 \mathbf{U} + (\lambda + 2\mu) \nabla(\nabla \cdot \mathbf{U}) = \rho \frac{\partial^2 \mathbf{U}}{\partial t^2} \quad (\text{D-1})$$

where  $\mathbf{U}$  is the displacement,  $t$  is time,  $\rho$  is the material density, and  $\mu$  and  $\lambda$  are Lamé constants ( $\mu$  is the shear modulus and  $\lambda + 2\mu$  is the plane wave or longitudinal modulus). Utilizing Helmholtz's theorem, the displacement is written as the gradient of a scalar potential function and the curl of a vector potential function.

$$\mathbf{U}(r, \theta, z) = u\mathbf{e}_r + v\mathbf{e}_\theta + w\mathbf{e}_z = \nabla\phi + \nabla \times \boldsymbol{\psi} \quad (\text{D-2})$$

Associated with this expression for the displacement, the gauge invariance of the transformation of equation (D-2) allows the divergence of the vector potential to be an arbitrary function (see Armenakas<sup>121</sup>).

$$\nabla \cdot \boldsymbol{\psi} = F(r, t) \quad (\text{D-3})$$

Substitution of equation (D-2) into equation (D-1) yields

$$\mu \nabla^2 (\nabla\phi + \nabla \times \boldsymbol{\psi}) + (\lambda + 2\mu) \nabla \nabla \cdot (\nabla\phi + \nabla \times \boldsymbol{\psi}) = \rho \frac{\partial^2}{\partial t^2} (\nabla\phi + \nabla \times \boldsymbol{\psi})$$

This equation is simplified by using the following vector identities

$$\nabla \cdot \nabla\phi = \nabla^2\phi \quad \text{and} \quad \nabla \cdot \nabla \times \boldsymbol{\psi} = 0$$

The equation of motion is then reduced to

$$\nabla \left[ (\lambda + 2\mu) \nabla^2\phi - \rho \frac{\partial^2}{\partial t^2} \phi \right] + \nabla \times \left[ \mu \nabla^2 \boldsymbol{\psi} - \rho \frac{\partial^2}{\partial t^2} \boldsymbol{\psi} \right] = 0 \quad (\text{D-4})$$

From equation (D-4) it can be seen that the potential expression for the displacement, (D-3), satisfies the equation of motion if the scalar potential,  $\phi$ , satisfies the scalar wave equation and the vector potential,  $\Psi$ , satisfies the vector wave equation.

$$\nabla^2 \phi = \frac{1}{C_d^2} \frac{\partial^2 \phi}{\partial t^2} \quad \text{where } C_d^2 = \frac{\lambda + 2\mu}{\rho} \quad (D-5)$$

$$\nabla^2 \Psi = \frac{1}{C_s^2} \frac{\partial^2 \Psi}{\partial t^2} \quad \text{where } C_s^2 = \frac{\mu}{\rho} \quad (D-6)$$

In equation (D-5),  $C_d$  is the dilatation or longitudinal wave speed and  $C_s$  is the transverse or shear wave speed. Each wave equation will be solved using the standard separation of variables technique.

The scalar wave equation, (D-5), in cylindrical coordinates is

$$\left[ \frac{\partial^2}{\partial r^2} + \frac{1}{r} \frac{\partial}{\partial r} + \frac{1}{r^2} \frac{\partial^2}{\partial \theta^2} + \frac{\partial^2}{\partial z^2} - \frac{1}{C_d^2} \frac{\partial^2}{\partial t^2} \right] \phi \quad (D-7)$$

where  $\phi(r, \theta, z, t) = R(r)\theta(\theta)Z(z)e^{-i\omega t}$  (a harmonic time dependence is assumed). The functional form of  $\phi$  is substituted into equation (D-7) and after simplification, the equation can be written as

$$\frac{R''}{R} + \frac{R'}{rR} + \frac{1}{r^2} \frac{\theta''}{\theta} + \frac{\omega^2}{C_d^2} = \frac{-Z''}{Z} = \xi^2 \quad (D-8)$$

The  $Z(z)$  dependence is separated out with  $\xi^2$  being the separation constant yielding

$$Z'' + \xi^2 Z = 0 \text{ which results in } Z(z) = Ae^{i\omega z} + Be^{-i\omega z}. \quad (D-9)$$

Equation (D-8) is modified with the second separation constant,  $\eta$ , to

$$\frac{r^2}{R} \left[ R'' + \frac{1}{r} R' \right] + \left[ \frac{\omega^2}{c_d^2} - \xi^2 \right] r^2 = -\frac{\theta''}{\theta} = \eta^2 \quad (D-10)$$

$$\text{The theta equation separates out to } \theta'' + \eta^2 \theta = 0 \quad (D-11)$$

where  $\theta(\theta) = D \cos(\theta\eta) + E \sin(\theta\eta)$ . Since  $\theta(\theta)$  must be single valued,

$\eta$  must be an integer,  $n$ , equal to 1,2,3,...

The radial equation can be written as

$$R'' + \frac{1}{r} R' + \left[ \frac{\omega^2}{c_d^2} - \xi^2 - \frac{n^2}{r^2} \right] R = 0 \quad (D-12)$$

which is Bessel's equation of order  $n$  and argument  $\alpha$  where

$$\alpha = \sqrt{\frac{\omega^2}{c^2} - \xi^2}. \quad (D-13)$$

The most general solution is:

$$R(r) = G_n J_n(\alpha r) + H_n Y_n(\alpha r) .$$

The general form for  $\phi(r, \theta, z, t)$  is

$$\sum_{n=0}^{\infty} (A_n \exp(-\iota \xi z) + B_n \exp(-\iota \xi z) (D_n \cos(n\theta) + E_n \sin(n\theta)) (G_n J_n(\alpha r) + H_n Y_n(\alpha r)))$$

$$\cdot \exp(-\iota \omega t) = 0 \quad (D-14)$$

The incident pressure wave for an angle of incidence of  $\gamma$  is

$$P_{inc}(r, \theta, z, t) = P_0 e^{\iota(K \cdot R - \omega t)}$$

$$= \sum_{n=0}^{\infty} \iota^n \epsilon_n \cos(n\theta) J_n\left(\frac{\omega}{C} \cos(\gamma r)\right) \exp(-\iota \omega t) \quad (D-15)$$

(C is the propagation speed in the fluid)

For this derivation,  $\phi$  represents the dilatation wave which results from the incident wave and, should have a form similar to its exciting force. In particular, the Z dependence should be the same as the incident wave, i.e. a traveling wave in the Z direction, which requires  $B_n = 0$ . The potential  $\phi$  must be symmetric with respect to  $\theta = 0$  (even function in  $\theta$ ) requiring  $E_n = 0$ . The result is

$$\phi(r, \theta, z, t) = \exp(i(\xi z - \omega t)) \sum_{n=0}^{\infty} \cos(n\theta) (G_n J_n(ar) + H_n Y_n(ar)) \quad (D-16)$$

The vector wave equation in component form with an  $e^{-i\omega t}$  time dependence is

$$\begin{aligned} \left( \nabla^2 \psi - \frac{\psi_r}{r} - \frac{2}{r^2} \frac{\psi_\theta}{\partial \theta} \right) e_r + \left( \nabla^2 \psi_\theta - \frac{\psi_\theta}{r} + \frac{2}{r^2} \frac{\psi_r}{\partial \theta} \right) e_\theta \\ + \nabla^2 \psi_z e_z = -\frac{\omega^2}{c_s^2} \left( \psi_r e_r + \psi_\theta e_\theta + \psi_z e_z \right) \end{aligned} \quad (D-17)$$

The following solutions are assumed:

$$\psi_r(r, \theta, z) = h_r(r) \sin(n\theta) e^{i\xi z} \quad (D-18)$$

$$\psi_\theta(r, \theta, z) = h_\theta(r) \cos(n\theta) e^{i\xi z} \quad (D-19)$$

$$\psi_z(r, \theta, z) = h_z(r) \sin(n\theta) e^{i\xi z} \quad (D-20)$$

The  $\theta$  functions must be single valued which requires  $n$  to be an integer. The selection of the sine and cosine term in  $\psi_r$ ,  $\psi_\theta$  and  $\psi_z$  results from the required nature of the  $\theta$  dependence for the longitudinal, torsional, and flexural modes (see Graff<sup>122</sup> p.466). The form of coupling between  $\psi_r$  and  $\psi_\theta$  in the  $e_r$  and  $e_\theta$  components indicates that a sine dependence for  $\psi_r$  is consistent with a cosine dependence for  $\psi_\theta$ . Additional justification for the trigonometric selection for  $\psi_z$  will

be presented later. The Z vector component results in the scalar wave equation for  $\psi_z$

$$\nabla^2 \psi_z = \frac{-\omega^2}{c_s^2} \psi_z \quad (D-21)$$

The solution to equation (D-21) is similar to that for  $\phi(r, \theta, z)$  and is

$$\psi_z(r, \theta, z) = e^{i(\xi z)} \sin(n\theta) (C_1 J_n(\beta r) + C_2 Y_n(\beta r)) \quad (D-22)$$

$$\text{where } \beta = \frac{\omega^2}{c_s^2} - \xi^2 \quad (D-23)$$

The two coupled equations for the  $h_r(r)$  and  $h_\theta(r)$  dependences are

$$\frac{d^2 h_r}{dr^2} + \frac{1}{r} \frac{dh_r}{dr} + \frac{1}{r^2} \left( -n^2 h_r + 2nh_\theta - h_r \right) - \xi^2 h_r + \frac{\omega^2}{c_s^2} h_r = 0 \quad (D-24)$$

$$\frac{d^2 h_\theta}{dr^2} + \frac{1}{r} \frac{dh_\theta}{dr} + \frac{1}{r^2} \left( -n^2 h_\theta + 2nh_r - h_\theta \right) - \xi^2 h_\theta + \frac{\omega^2}{c_s^2} h_\theta = 0 \quad (D-25)$$

Equations (D-24) and (D-25) are then solved simultaneously for

$h_r$  and  $h_\theta$  resulting in two coupled Bessel's equations. Subtracting

(D-25) from (D-24) yields

$$\left[ \frac{d^2}{dr^2} + \frac{1}{r} \frac{d}{dr} + \beta^2 - \frac{(n+1)^2}{r^2} \right] (h_r - h_\theta) = 0 \quad (D-26)$$

This Bessel's equation solution is

$$h_r - h_\theta = 2C_3 J_{n+1}(\beta r) + 2C_4 Y_{n+1}(\beta r) \quad (D-27)$$

Adding equations (D-24) and (D-25) yields

$$\left[ \frac{d^2}{dr^2} + \frac{1}{r} \frac{d}{dr} + \beta^2 - \frac{(n-1)^2}{r^2} \right] (h_r + h_\theta) = 0 \quad (D-28)$$

The solution to this Bessel's equation is

$$h_r + h_\theta = 2C_5 J_{n-1}(\beta r) + 2C_6 Y_{n-1}(\beta r) \quad (D-29)$$

adding and subtracting equations (D-28) and (D-29) gives  $h_r$  and  $h_\theta$ .

$$h_r = C_3 J_{n+1}(\beta r) + C_4 Y_{n+1}(\beta r) + C_5 J_{n-1}(\beta r) + C_6 Y_{n-1}(\beta r) \quad (D-30a)$$

$$h_\theta = C_3 J_{n+1}(\beta r) + C_4 Y_{n+1}(\beta r) - C_5 J_{n-1}(\beta r) - C_6 Y_{n-1}(\beta r) \quad (D-30b)$$

As shown by Armenakas, et al.<sup>121</sup>, the gauge invariance yields  $\nabla \cdot \Psi = F(r)$

where  $F(r)$  is arbitrary. Meeker and Metzler<sup>123</sup> demonstrate that  $F(r)$  can be adjusted so as to eliminate one potential function (since there are eight constants and six boundary conditions); this is equivalent to setting  $C_5$  and  $C_6$  equal to zero.

The result is



$$h_r = -h_\theta \quad \text{where} \quad h_r = C_3 J_{n+1}(\beta r) + C_4 Y_{n+1}(\beta r). \quad (D-24)$$

The displacement components of equation (D-2) can now be written as

$$u = \left[ R' + \frac{n}{r} h_z + \xi h_r \right] \cos(n\theta) e^{i(\xi z - \omega t)} \quad (D-25a)$$

$$v = \left[ -\frac{n}{r} R + \xi h_r - h_z' \right] \sin(n\theta) e^{i(\xi z - \omega t)} \quad (D-25b)$$

$$w = \left[ -\xi R - h_r' - \frac{(n+1)}{r} h_r \right] \cos(n\theta) e^{i(\xi z - \omega t)} \quad (D-25c)$$

For normal incidence,  $w = 0$  ( $\xi = \sin \gamma = 0$ ) or  $h_r' + \frac{n+1}{r} h_r = 0$

Substitution of equation (D-24) into the above expression yields

$$C_3 \left[ J_{n+1}'(\beta r) + \frac{n+1}{r} J_{n+1}(\beta r) \right] + C_4 \left[ Y_{n+1}'(\beta r) + \frac{n+1}{r} Y_{n+1}(\beta r) \right] = 0$$

This expression must be valid for all values of  $n$  and  $\beta r$ . If  $n = -1$  the above expression reduces to

$$C_3 J_1(\beta r) = -C_4 Y_1(\beta r)$$

In the limit as  $\beta r \rightarrow 0$ ,  $C_4$  must equal 0, and in the limit as  $\beta r \rightarrow \infty$ ,  $C_3$  must equal 0.

This is only possible if both  $C_3$  and  $C_4$  are zero; therefore,  $h_r$  and  $h_\theta$  must also be zero for the normal incidence case. This result is also intuitive since the only contribution to the  $Z$  displacement component, which is zero, is from the curl of  $h_r$  and  $h_\theta$ . The gauge invariance allows one potential to be set to zero, therefore the

other must also be zero or constant.

For the normal incidence case,  $\psi_z$  represents the shear wave in the cylinder which must vanish at  $\theta$  equal to  $\pi$  and 0, and be a maximum at  $\theta$  equal to  $\pi/2$  and  $3\pi/2$ . Since the shear wave is antisymmetric with respect to  $\theta$  equal to 0, the sine trigonometric function is the proper selection for the  $\theta$  function for  $\psi_z$ .

#### Scattering From the Two Layer Cylinder With Normal Incidence

The normal incidence layer problem is similar to the elastic cylinder (normal incidence) derived previously in that two potential functions can fully represent the wave behavior in layers. The outer layer is assumed to be viscoelastic with the loss factor being represented by a complex wave number. The inner layer is assumed to be perfectly elastic which is valid for most metals below the megahertz frequency region. The method of solution is to represent the stresses and displacements in the four regions and solve the boundary value problem. The geometry is represented in figure D-2. For notation purposes,  $k_i$  is the wave number in the region  $i$  ( $i=1,2,3,4$ ). In regions 2 and 3, the  $s$  and  $d$  subscripts indicated the wave number is for the shear (transverse) and longitudinal (dilatation) waves respectively.

In region 1 (exterior fluid), the total pressure,  $P_1(r,\theta)$ , is the sum of the incident plane wave and scattered pressure

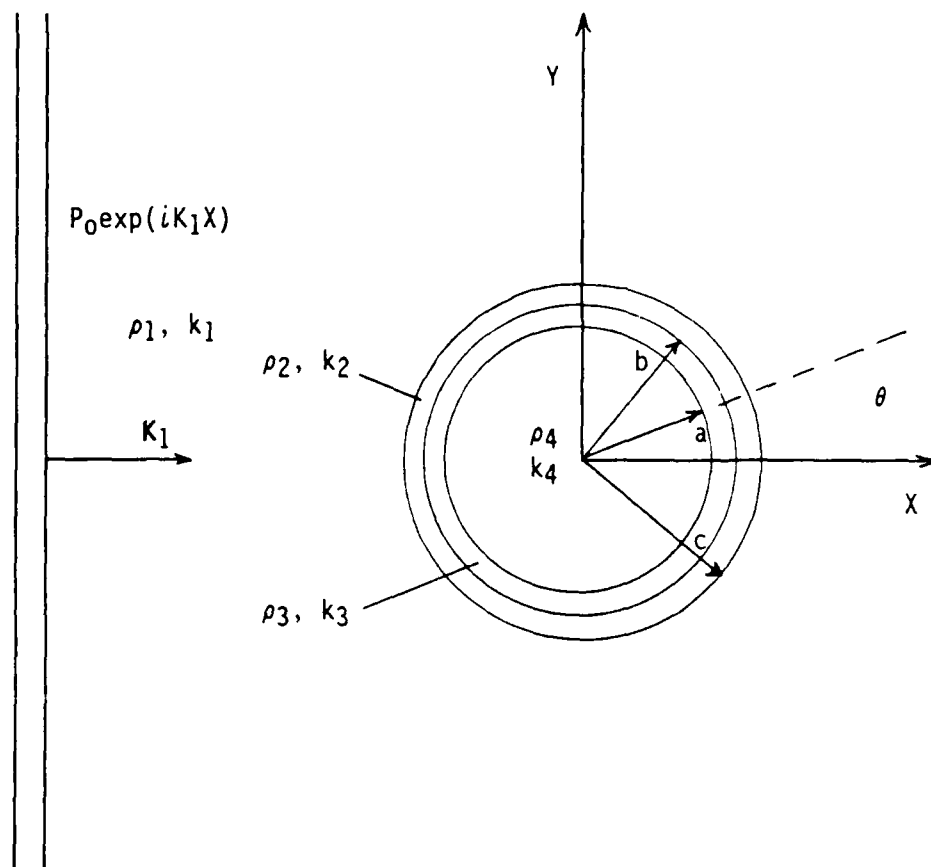


Figure D-2 Scattering Geometry for the Layered Cylindrical Shell

$$P_1(r, \theta) = P_0 \sum_{n=0}^{\infty} \epsilon_n \cos(n\theta) (b_n H_n^1(k_1 r) + J_n(k_1 r)). \quad (D-26)$$

In the viscoelastic layer, region 2, the potentials are

$$\phi_2(r, \theta) = P_0 \sum_{n=0}^{\infty} \epsilon_n \cos(n\theta) (c_n J_n(k_d 2r) + d_n Y_n(k_d 2r)) \quad (D-27)$$

$$\psi_2(r, \theta) = P_0 \sum_{n=0}^{\infty} \epsilon_n \sin(n\theta) (e_n J_n(k_s 2r) + f_n Y_n(k_s 2r)). \quad (D-28)$$

In the elastic layer, region 3, the potential functions are

$$\phi_3(r, \theta) = P_0 \sum_{n=0}^{\infty} \epsilon_n \cos(n\theta) (g_n J_n(k_d 3r) + h_n Y_n(k_d 3r)) \quad (D-29)$$

$$\psi_3(r, \theta) = P_0 \sum_{n=0}^{\infty} \epsilon_n \sin(n\theta) (l_n J_n(k_s 3r) + m_n Y_n(k_s 3r)). \quad (D-30)$$

In the interior fluid, region 4, the pressure is written as

$$P_4(r, \theta) = P_0 \sum_{n=0}^{\infty} \epsilon_n \cos(n\theta) (N_n J_n(k_4 r)). \quad (D-31)$$

The displacements in terms of the potential functions are

$$u = u(r, \theta) = \frac{\partial \phi}{\partial r} + \frac{1}{r} \frac{\partial \psi}{\partial \theta} \quad (D-32)$$

$$v = v(r, \theta) = \frac{1}{r} \frac{\partial \phi}{\partial \theta} - \frac{\partial \psi}{\partial r} \quad (D-33)$$

The stresses in terms of the potential functions are

$$\tau_{rr} = -\lambda k_d^2 \phi + 2\mu \left[ \frac{\partial^2 \phi}{\partial r^2} - \frac{1}{r^2} \frac{\partial \psi}{\partial \theta} + \frac{1}{r} \frac{\partial^2 \psi}{\partial \theta \partial r} \right] \quad (D-34)$$

$$\tau_{r\theta} = \mu \left[ \frac{-2}{r^2} \frac{\partial \phi}{\partial \theta} + \frac{2}{r} \frac{\partial^2 \phi}{\partial \theta \partial r} - \frac{\partial^2 \psi}{\partial r^2} + \frac{1}{r} \frac{\partial \psi}{\partial r} + \frac{1}{r^2} \frac{\partial^2 \psi}{\partial \theta^2} \right] \quad (D-35)$$

The radial displacement in regions 1 and 4 may be written in terms of the pressure using Euler's equation

$$u = \frac{1}{\rho \omega^2} \frac{\partial P}{\partial r} \quad (D-36)$$

The radial stress is the negative of the pressure in these regions.

The boundary conditions are the requirement of continuity of stress and displacement across the three interfaces. They are as follows:

(i) at  $r=c$ ,

$$\tau_{rr}^1 = -p_1, \quad u^1 = u^2, \quad \tau_{r\theta}^2 = 0$$

(ii) at  $r=b$ ,

$$\tau_{rr}^2 = \tau_{rr}^3, \quad u^1 = u^2, \quad v^2 = v^3, \quad \tau_{r\theta}^2 = \tau_{r\theta}^3$$

(iii) at  $r=a$ ,

$$\tau_{rr}^3 = -p_4, \quad u^3 = u^4, \quad \tau_{r\theta}^3 = 0 \quad (D-37)$$

A set of ten equations in ten unknown coefficients results as follows:

$$D \mathbf{x}_n = \mathbf{A}_n \quad (D-38)$$

where  $\mathbf{x}_n$  is a column vector of the unknown coefficients,  $\mathbf{A}_n$  is a column vector of the nonvanishing elements  $A_1$  and  $A_2$ , and  $D$  is a  $10 \times 10$  matrix with 60 nonzero elements which results from application of the boundary conditions. The  $D$  matrix nonzero coefficients are:

$$D_{1,1} = \frac{\rho_1 \omega^2}{\mu_2} H_n^1(k_1 c) \quad (D-39)$$

$$D_{1,2} = (2n^2 - k_{s2}^2 c^2) J_n(k_{d2} c) - 2k_{d2} c J_n'(k_{d2} c)$$

$$D_{1,3} = (2n^2 - k_{s2}^2 c^2) Y_n(k_{d2} c) - 2k_{d2} c Y_n'(k_{d2} c)$$

$$D_{1,4} = 2n(k_{s2} c J_n'(k_{s2} c) - J_n(k_{s2} c))$$

$$D_{1,5} = 2n(k_{s2} c Y_n'(k_{s2} c) - Y_n(k_{s2} c))$$

$$D_{2,1} = -k_1 c H_n^1(k_1 c)$$

$$D_{2,2} = k_{d2} c J_n'(k_{d2} c)$$

$$D_{2,3} = k_{d2} c Y_n'(k_{d2} c)$$

$$D_{2,4} = n J_n(k_{s2} c)$$

$$D_{2,5} = n Y_n(k_{s2} c)$$

$$D_{3,2} = 2n(J_n(k_{d2} c) - k_{d2} c J_n'(k_{d2} c))$$

$$D_{3,3} = 2n(Y_n(k_{d2} c) - k_{d2} c Y_n'(k_{d2} c))$$

$$D_{3,4} = 2k_{s2} c J_n'(k_{s2} c) + (k_{s2}^2 c^2 - 2n^2) J_n(k_{s2} c)$$

$$D_{3,5} = 2k_{s2} c Y'_n(k_{s2} c) + (k_{s2}^2 c^2 - 2n^2) Y_n(k_{s2} c)$$

$$D_{4,2} = k_{d2} b J'_n(k_{d2} b)$$

$$D_{4,3} = k_{d2} b Y'_n(k_{d2} b)$$

$$D_{4,4} = n J_n(k_{s2} b)$$

$$D_{4,5} = n Y_n(k_{s2} b)$$

$$D_{4,6} = -k_{d3} b J'_n(k_{d3} b)$$

$$D_{4,7} = -k_{d3} b Y'_n(k_{d3} b)$$

$$D_{4,8} = -n J_n(k_{s3} b)$$

$$D_{4,9} = -n Y_n(k_{s3} b)$$

$$D_{5,2} = -n J_n(k_{d2} b)$$

$$D_{5,3} = -n Y_n(k_{d2} b)$$

$$D_{5,4} = -k_{s2} b J'_n(k_{s2} b)$$

$$D_{5,5} = -k_{s2} b Y'_n(k_{s2} b)$$

$$D_{5,6} = n J_n(k_{d3} b)$$



$$D_{5,7} = nY_n(k_{d3}b)$$

$$D_{5,8} = k_{s3}bJ'_n(k_{s3}b)$$

$$D_{5,9} = k_{s3}bY'_n(k_{s3}b)$$

$$D_{6,2} = \frac{\mu_2}{\mu_3} ((2n^2 - k_{s2}^2b^2)J_n(k_{d2}b) - 2k_{d2}bJ'_n(k_{d2}b))$$

$$D_{6,3} = \frac{\mu_2}{\mu_3} ((2n^2 - k_{s2}^2b^2)Y_n(k_{d2}b) - 2k_{d2}bY'_n(k_{d2}b))$$

$$D_{6,4} = \frac{\mu_2}{\mu_3} 2n(k_{s2}bJ'_n(k_{s2}b) - J_n(k_{s2}b))$$

$$D_{6,5} = \frac{\mu_2}{\mu_3} 2n(k_{s2}bY'_n(k_{s2}b) - Y_n(k_{s2}b))$$

$$D_{6,6} = 2k_{s3}bJ'_n(k_{d3}b) - (2n^2 - k_{s3}^2b^2)J_n(k_{d3}b)$$

$$D_{6,7} = 2k_{s3}bY'_n(k_{d3}b) - (2n^2 - k_{s3}^2b^2)Y_n(k_{d3}b)$$

$$D_{6,8} = 2n(J_n(k_{s3}b) - k_{s3}bJ'_n(k_{s3}b))$$

$$D_{6,9} = 2n(Y_n(k_{s3}b) - k_{s3}bY'_n(k_{s3}b))$$

$$D_{7,2} = 2n(J_n(k_{d2}b) - k_{d2}bJ'_n(k_{d2}b))$$

$$D_{7,3} = 2n(Y_n(k_{d2}b) - k_{d2}bY'_n(k_{d2}b))$$

$$D_{7,4} = 2k_{s2}bJ'_n(k_{s2}b) + (k_{s2}^2b^2 - 2n^2)J_n(k_{s2}b)$$

$$D_{7,5} = 2k_{s2}bY'_n(k_{s2}b) + (k_{s2}^2b^2 - 2n^2)Y_n(k_{s2}b)$$

$$D_{7,6} = \frac{\mu_3}{\mu_2} 2n(k_{d3}bJ'_n(k_{d3}b) - J_n(k_{d3}b))$$

$$D_{7,7} = \frac{\mu_3}{\mu_2} 2n(k_{d3}bY'_n(k_{d3}b) - Y_n(k_{d3}b))$$

$$D_{7,8} = -\frac{\mu_3}{\mu_2} (2k_{s3}bJ'_n(k_{s3}b) + (k_{s3}^2b^2 - 2n^2)J_n(k_{s3}b))$$

$$D_{7,9} = -\frac{\mu_3}{\mu_2} (2k_{s3}bY'_n(k_{s3}b) + (k_{s3}^2b^2 - 2n^2)Y_n(k_{s3}b))$$

$$D_{8,6} = (2n^2 - k_{s3}^2a^2)J_n(k_{d3}a) - 2k_{d3}aJ'_n(k_{d3}a)$$

$$D_{8,7} = (2n^2 - k_{s3}^2a^2)Y_n(k_{d3}a) - 2k_{d3}aY'_n(k_{d3}a)$$

$$D_{8,8} = 2n(k_{s3}aJ'_n(k_{s3}a) - J_n(k_{s3}a))$$

$$D_{8,9} = 2n(k_{s3}aY'_n(k_{s3}a) - Y_n(k_{s3}a))$$

$$D_{8,10} = \frac{\rho_4}{\rho_3} k_{s3}^2a^2J_n(k_4a)$$

$$D_{9,6} = k_{d3} a J'_n(k_{d3} a)$$

$$D_{9,7} = k_{d3} a Y'_n(k_{d3} a)$$

$$D_{9,8} = n J_n(k_{s3} a)$$

$$D_{9,9} = n Y_n(k_{s3} a)$$

$$D_{9,10} = -k_4 a J'_n(k_4 a)$$

$$D_{10,6} = 2n(J_n(k_{d3} a) - k_{d3} a J'_n(k_{d3} a))$$

$$D_{10,7} = 2n(Y_n(k_{d3} a) - k_{d3} a Y'_n(k_{d3} a))$$

$$D_{10,8} = 2k_{s3} a J'_n(k_{s3} a) + (k_{s3}^2 a^2 - 2n^2) J_n(k_{s3} a)$$

$$D_{10,9} = 2k_{s3} a Y'_n(k_{s3} a) + (k_{s3}^2 a^2 - 2n^2) Y_n(k_{s3} a)$$

The A vector has two nonzero elements which are

$$A_1 = -\frac{c^2}{\mu_2} J_n(k_1 c) \quad \text{and} \quad A_2 = \frac{k_1 c}{\rho_1 \omega^2} J'_n(k_1 c) . \quad (D-40)$$

The D matrix has been adjusted by multiplying column 1 by  $\rho_1 \omega^2$  and column 10 by  $\rho_4 \omega^2$  as suggested by Gaunaud<sup>59</sup>. (The above coefficients were originally derived by Guanaud<sup>59</sup> but were rederived for verification. Verification of the coefficients derived by Flax and Neubauer<sup>58</sup> could not be obtained.) Additional scaling has

been done on the sixth and seventh columns to prevent computational problems.

For the  $n=0$  case, the  $\psi_2$  and  $\psi_3$  potential functions are 0 due to the sine term. This results in  $\tau_{r\theta}$  always being zero regardless of the constants, which causes these three boundary conditions to be meaningless. In addition, the continuity of  $v$  displacement is also meaningless. The overall result is to reduce the  $D$  matrix from a  $10 \times 10$  matrix to a  $6 \times 6$  matrix by eliminating rows 3,5,7 and 10 and columns 4,5,8 and 9.

### Elastic Shell Derivation

The solution for the scattered pressure from the purely elastic shell is obtained from the preceding discussion by eliminating the viscoelastic layer (layer 2) and applying the outer fluid boundary conditions to the elastic layer. The total pressure in fluid 1 is expressed by equation (D-26). The vector and scalar potentials for the elastic solid are expressed by equations (D-29) and (D-30). The total pressure in the interior fluid (fluid 4) is expressed by equation (D-31). The boundary conditions are:

(i) at  $r=b$ ,

$$\tau_{rr}^3 = -p_1, \quad u^1 = u^3, \quad \tau_{r\theta}^3 = 0$$

(iii) at  $r=a$ ,

$$\tau_{rr}^3 = -P_4, \quad u^3 = u^4, \quad \tau_{r\theta}^3 = 0 \quad (D-41)$$

A set of six equations in six unknown coefficients results as follows:

$$D \mathbf{x}_n = \mathbf{A}_n \quad (D-42)$$

where  $\mathbf{x}_n$  is a column vector of the unknown coefficients,  $\mathbf{A}_n$  is a column vector of the nonvanishing elements  $A_1$  and  $A_2$ , and  $D$  is a  $6 \times 6$  matrix with 28 nonzero elements which results from application of the boundary conditions. The  $D$  matrix nonzero coefficients are:

$$D_{1,1} = \frac{\rho_1 \omega^2}{\mu_3} H_n^1(k_1 c) \quad (D-43)$$

$$D_{1,2} = (2n^2 - k_{s3}^2 b^2) J_n(k_{d3} b) - 2k_{d3} b J_n'(k_{d3} b)$$

$$D_{1,3} = (2n^2 - k_{s3}^2 b^2) Y_n(k_{d3} b) - 2k_{d3} b Y_n'(k_{d3} b)$$

$$D_{1,4} = 2n(k_{s3} b J_n'(k_{s3} b) - J_n(k_{s3} b))$$

$$D_{1,5} = 2n(k_{s3} b Y_n'(k_{s3} b) - Y_n(k_{s3} b))$$

$$D_{2,1} = -k_1 b H_n^1(k_1 b)$$

$$D_{2,2} = k_{d3} b J_n'(k_{d3} b)$$

$$D_{2,3} = k_{d3} b Y'_n(k_{d3} b)$$

$$D_{2,4} = n J_n(k_{s3} b)$$

$$D_{2,5} = n Y_n(k_{s3} b)$$

$$D_{3,2} = 2n(J_n(k_{d3} b) - k_{d3} b J'_n(k_{d3} b))$$

$$D_{3,3} = 2n(Y_n(k_{d3} b) - k_{d3} b Y'_n(k_{d3} b))$$

$$D_{3,4} = 2k_{s3} b J'_n(k_{s3} b) + (k_{s3}^2 b^2 - 2n^2) J_n(k_{s3} b)$$

$$D_{3,5} = 2k_{s3} b Y'_n(k_{s3} b) + (k_{s3}^2 b^2 - 2n^2) Y_n(k_{s3} b)$$

$$D_{4,2} = (2n^2 - k_{s3}^2 a^2) J_n(k_{d3} a) - 2k_{d3} a J'_n(k_{d3} a)$$

$$D_{4,3} = (2n^2 - k_{s3}^2 a^2) Y_n(k_{d3} a) - 2k_{d3} a Y'_n(k_{d3} a)$$

$$D_{4,4} = 2n(k_{s3} a J'_n(k_{s3} a) - J_n(k_{s3} a))$$

$$D_{4,5} = 2n(k_{s3} a Y'_n(k_{s3} a) - Y_n(k_{s3} a))$$

$$D_{4,6} = \frac{\rho_4}{\rho_3} k_{s3}^2 a^2 J_n(k_4 a)$$

$$D_{5,2} = -2n(k_{d3} a J'_n(k_{d3} a) - J_n(k_{d3} a))$$

$$D_{5,3} = -2n(k_{d3} a Y'_n(k_{d3} a) - Y_n(k_{d3} a))$$

$$D_{5,4} = 2k_{s3} a J'_n(k_{s3} a) + (k_{s3}^2 a^2 - 2n^2) J_n(k_{s3} a)$$

$$D_{5,5} = 2k_{s3} a Y'_n(k_{s3} a) + (k_{s3}^2 a^2 - 2n^2) Y_n(k_{s3} a)$$

$$D_{6,2} = k_{d3} a J'_n(k_{d3} a)$$

$$D_{6,3} = k_{d3} a Y'_n(k_{d3} a)$$

$$D_{6,4} = n J_n(k_{s3} a)$$

$$D_{6,5} = n Y_n(k_{s3} a)$$

$$D_{6,6} = -k_4 a J'_n(k_4 a)$$

The A vector has two nonzero elements which are

$$A_1 = -\frac{b^2}{\mu_3} J_n(k_1 b) \quad \text{and} \quad A_2 = \frac{k_1 b}{\rho_1 \omega^2} J'_n(k_1 b) . \quad (D-44)$$

As with the layer solution, the D matrix is reduced for the  $n=0$  case (D matrix reduces to a 4x4 matrix).

The elastic shell code is verified by comparing the theoretical results with the experimentally obtained form function for the simulated infinite cylindrical shell. In addition, the theoretical computer results were qualitatively compared with the theoretical form functions illustrated by Flax and Neubauer<sup>58</sup>. The viscoelastic

layer program was verified by: (1) recovering the experimental shell form function when the viscoelastic layer parameters simulated a lossless water layer, and (2) the pressure release form function generated in Appendix A was recovered when the viscoelastic parameters were set to simulate a low loss air layer.

The Bessel functions are generated by the methods indicated in Appendix A. The accuracy of the Bessel functions were checked against published tables and other library routines. In addition, the Wronskian values calculated using the Bessel functions and their derivatives were continually compared against the exact values for a estimate of solution accuracy. The matrix equations are solved by a standard IMSL routine (LEQ2C) which utilizes a lower-upper decomposition method with iterative improvement. All computations were performed using double precision on a Vax-750 or Micro-Vax computers.



## APPENDIX E

### The Treatment of Multiple Reflections in the Panel for Plane Wave Modulus Experiment

Due to the large difference in the specific acoustic impedances of the water and the materials used in the plane wave modulus experiment, significant reflection will occur at all interfaces. The purpose of the experiment is to determine the transmission of sound through the material. The reflections of importance are the internal reflections that occur in the material which eventually add to the directly transmitted pulse but with delayed phase and reduced amplitude. To fully assess the transmission through the panel, these multiple reflections must be taken into account. For the closed cell rubber materials, the attenuation in the material is so large that the multiple reflections are significantly reduced and hence have little or no effect on the direct transmission. The corprene and cork-nitrile composites, however, do not have a large enough attenuation to permit neglect of multiple reflections.

As illustrated in figure E-1, an incident wave contacts the surface (2) and a portion of the wave is transmitted. At the next interface between the two materials a portion of the first transmitted wave is transmitted into the medium. The portion transmitted from the water into the material is related by the transmission

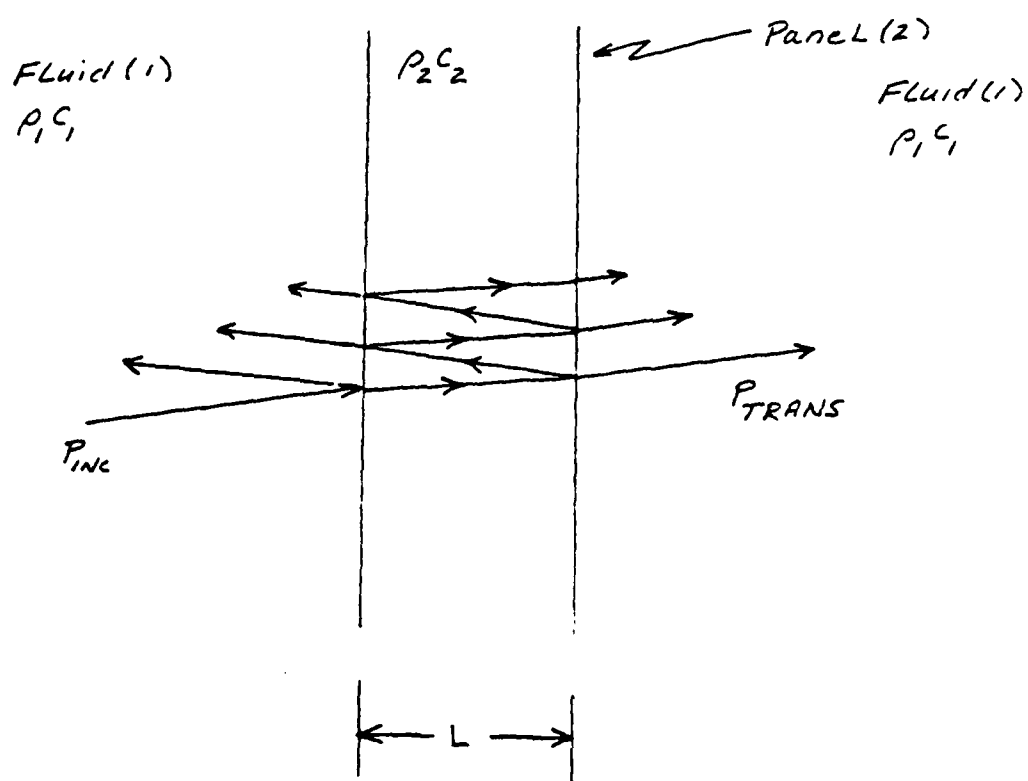


Figure E-1 Multiple Internal Reflection in a One-Dimensional Panel

coefficient  $T_{1,2}$  and the portion transmitted from the material into the water is related to  $T_{2,1}$  where

$$T_{1,2} = \frac{2r_2}{r_1 + r_2} \quad T_{2,1} = \frac{2r_1}{r_1 + r_2} \quad (E-1)$$

and,  $r_1$  is the specific acoustic impedance of the water and  $r_2$  is the specific acoustic impedance of the panel material. There is also reflection of the sound wave occurring at the material-water interface with the amount of reflection determined by the reflection coefficient,  $R$ , where

$$R = \frac{r_1 - r_2}{r_1 + r_2} \quad (E-2)$$

The incident wave,  $P_0$ , is related to the transmitted wave,  $P_t$ , by

$$P_t = P_0 \left\{ T_{1,2}T_{2,1} e^{-\alpha L} e^{i\omega L/c} + T_{1,2}T_{2,1}R^2 e^{-3\alpha L} e^{i3\omega/c} \right. \\ \left. T_{1,2}T_{2,1}R^2 e^{-\alpha 4L} e^{i5\omega L/c} + \dots \right\} \quad (E-3)$$

The direct transmission can be factored out resulting in

$$P_t = P_0 T_{1,2} T_{2,1} e^{-\alpha L} e^{i\omega L/c} \left\{ 1 + R^2 e^{-2\alpha L} e^{i\omega 2L/c} + R^4 e^{-4\alpha L} e^{i\omega 4L/c} + \dots \right\} \quad (E-4)$$

Let  $T = T_{1,2} T_{2,1} e^{-\alpha L} e^{i\omega L/c}$  and  $x = R^2 e^{-2\alpha L} e^{i\omega 2L/c}$ , then

equation (E-3) can be written as

$$\frac{P_t}{P_0} = T (1 + x + x^2 + \dots) \quad (E-5)$$

Since  $x < 1$ , the series sums to  $\frac{1}{1-x}$ . Equation (E-5) becomes

$$\frac{P_t}{P_0} = \frac{T}{1-x} \quad (E-6)$$

From the experimental setup, the ratio of transmitted pressure

to incident pressure is

$$\frac{P_t}{P_0} = \frac{P_c \exp(i\phi_c)}{P_w \exp(i\phi_w)} \exp \left( \frac{i\omega L}{c_w} \right)$$

where  $\phi_w$  is the unwrapped phase for the water only,  $\phi_c$  is the un-

wrapped phase with the panel in place,  $c_w$  is the propagation speed of

the water and  $c$  is the phase speed of the sample. The ratio of amplitudes,  $A$ , and phase,  $\phi$ , is determined directly from the FFT data with

$$A = \frac{P_C}{P_W} \quad \phi = \phi_C - \phi_W + \frac{\omega L}{c_W} \quad (E-7)$$

The  $\frac{\omega L}{c_W}$  term is due to a thickness of water,  $L$ , being displaced by the panel.

#### Iteration Process

The equation to be iterated is

$$T = A \exp(i\phi) (1-x) \quad (E-8)$$

1. No internal reflections is assumed, i.e.  $x = 0$ .

$$\text{the initial phase speed is } c = \frac{\omega L}{\phi} \quad (E-9)$$

From the initial phase speed,  $T_{1,2}$  and  $T_{2,1}$  are calculated

and the initial attenuation,  $\alpha$ , is determined from

$$A = T_{1,2} T_{2,1} \exp(-\alpha L). \quad (E-10)$$

2. From the initial values of  $c$  and  $\alpha$ , the phase and amplitude corrections for the multiple internal reflections are calculated.

$$A_m = |1 - x| \quad \phi_m = \text{phase of } (1 - x)$$

The phase speed is now

$$c = \frac{\omega L}{\phi + \phi_m}.$$

This new phase speed is used to calculate  $T_{1,2}$  and  $T_{2,1}$ .

The new attenuation,  $\alpha$ , is determined from

$$A A_m = T_{1,2} T_{2,1} \exp(-\alpha L). \quad (E-)$$

Additional iteration are performed by repeated performance of step  
Convergence is usually rapid however, the pulses do not always occur for  
frequencies less than 15kHz. The nonconvergence is suspected to result from dif-  
fraction effects or some unaccounted motion of the panel causing the one dimen-  
sional transmission line analysis to be invalid.

## BIBLIOGRAPHY

1. J. J. Bowman, T. B. A. Senior, and P. L. Ualenghi ed., Electromagnetic and Acoustic Scattering By Simple Shapes (North-Holland Publishing Company, Amsterdam, 1969).
2. H. Uberall, "Surface Waves in Acoustics," in Physical Acoustics, edited by W. P. Mason and R. N. Thurston, (Academic, New York, 1973), Vol. X.
3. H. Uberall and H. Huang, "Acoustical Response of Submerged Elastic Structures Obtained Through Integral Transforms," in Physical Acoustics, edited by W. P. Mason and R. N. Thurston, (Academic, New York, 1976), Vol. XII.
4. U. K. Nigul editor, "Echo Signals from Elastic Objects," (Academy of Sciences Estonian SSR, Cybernetics Institute, 1974) translation the Russian by the Joint Publications Research Service, Arlington, Va. 22201, Document No. 63937, 22 January 1975.
5. W. G. Neubauer, "Procedure for Evaluating a Reflection-Reduction Coating," J. Acoust. Soc. Am. **62**, pp. 1024-1027, (1977).
6. I.B. Andreeva and V. G. Samovol'kin, "Sound Scattering by Elastic Cylinders of Finite Length," Sov. Phys. Acoust. **22**, pp.361-364, (1976).
7. Lord Rayleigh, Theory of Sound (MacMillan, London, 1929), 2nd edition.
8. P. M. Morse, Vibration and Sound, (McGraw-Hill, New York, 1936).
9. J. J. Faran, Jr., "Sound Scattering by Solid Cylinders and Spheres," J. Acoust. Soc. Am. **23**, pp. 405-418, (1951).
10. A. E. H. Love, A Treatise on the Mathematical Theory of Elasticity, (Dover, New York, 1944), 4th edition.
11. R. Hickling, "Analysis of Echoes from a Solid Elastic Sphere in Water," J. Acoust. Soc. Am. **34**, pp. 1582-1592 (1962).

12. R. Hickling, "Analysis of Echoes from a Hollow Metallic Sphere in Water," J. Acoust. Soc. Am. **36**, pp. 1124-1137 (1964).
13. L. D. Hampton and C. M. McKinney, "Experimental Study of the Scattering of Acoustic Energy from solid Metal Spheres in Water," J. Acoust. Soc. Am. **33**, pp. 664-673 (1961).
14. K. J. Diercks and R. Hickling, "Echoes from Hollow Aluminum Spheres in Water," J. Acoust. Soc. Am. **41**, pp. 380-393 (1967).
15. W. G. Neubauer, R. H. Vogt, and L. R. Dragonette, "Acoustic Reflection from Elastic Spheres. 1. Steady State Signals," J. Acoust. Soc. Am. **55**, pp. 1123-1129 (1974).
16. L. R. Dragonette, R. H. Vogt, L. Flax, and W. G. Neubauer, "Acoustic Reflection from Elastic Spheres and Rigid Spheres and Spheroids. 11. Transient Analysis," J. Acoust. Soc. Am. **55**, pp. 1130-1137 (1974).
17. H. D. Dardy, J. A. Bucaro, L. S. Scheutz, and L. R. Dragonette, "Dynamic Wide-Bandwidth Acoustic Form Function Determination," J. Acoust. Soc. Am. **62**, pp. 1373-1376 (1977).
18. G. R. Barnard and C. M. McKinney, "Scattering of Sound by Solid and Air-Filled Cylinders in Water," J. Acoust. Soc. Am. **33**, pp. 226-238 (1961).
19. K. J. Diercks, T. G. Goldsberry, and C. W. Horton, "Circumferential Waves in Thin-Walled Air-Filled Cylinders in Water," J. Acoust. Soc. Am. **35**, pp. 59-64, (1963).
20. T. G. Goldsberry, "Reflection of Circumferential Waves from a Slit in a Thin-Walled Cylinder," J. Acoust. Soc. Am. **42**, pp. 1298-1303, (1967).
21. C. W. Horton and M. V. Mechler, "Circumferential Waves in a Thin-Walled Air-Filled Cylinder in a Water Medium," J. Acoust. Soc. Am. **51**, pp. 295-303, (1972).
22. W. Franz, Z. Naturforsch **9a**, pp. 705-716, (1954).
23. W. G. Neubauer, Acoustic Reflection from Surfaces and Shapes (Naval Research Laboratory, Washington, 1986) Chapters 3 and 4.
24. W. G. Neubauer, "Experimental Measurements of "Creeping" Waves in Solid Aluminum Cylinders in Water Using Pulses," J. Acoust. Soc. Am. **44**, pp. 298-299 (1968).



25. M. L. Hartbolt and B. N. Steinberg, "Direct Experimental Verification of Creeping Waves," J. Acoust. Soc. Am. **45**, pp. 592-603 (1969).
26. O. D. Grace and R. R. Goodman, "Circumferential Waves on a Solid Cylinder," J. Acoust. Soc. Am. **39**, pp. 173-174, (1976).
27. R. E. Bunney, R. R. Goodman and S. W. Marshall, "Rayleigh and Lamb Waves on Cylinders," J. Acoust. Soc. Am. **46**, pp. 1223-1233, (1969).
28. W. G. Neubauer, "Pulsed Circumferential Waves on Aluminum Cylinders in Water," J. Acoust. Soc. Am. **45**, pp. 1134-1144, (1969).
29. H. Uberall, L. R. Dragonette and L. Flax, "Relation Between Creeping Waves and Normal Modes of Vibration of a Curved Body," J. Acoust. Soc. Am. **61**, pp. 711-715, (1977).
30. H. Uberall, R. D. Doolittle and J. V. McNicholas, "Use of Sound Pulses for a Study of Circumferential Waves," J. Acoust. Soc. Am. **39**, pp. 564-578, (1965).
31. P. Ugincius and H. Uberall, "Creeping-Wave Analysis of Acoustic Scattering by Elastic Cylindrical Shells," J. Acoust. Soc. Am. **43**, pp. 1025-1035, (1968).
32. R. D. Doolittle and H. Uberall, "Sound Scattering by Elastic Cylindrical Shells," J. Acoust. Soc. Am. **39**, pp. 272-275, (1966).
33. Lord Rayleigh, "Proc. London Math. Soc.," [1], **17**, (1885).
34. A. E. H. Love, "Some Problems of Geodynamics," Cambridge University Press, London 1911.
35. R. Stoneley, Proc. Roy. Soc., Ser. A, **106**, 416, 1924.
36. I. A. Viktorov, Rayleigh and Lamb Waves, (Plenum Press, New York, 1967).
37. G. V. Frisk and H. Uberall, "Creeping Waves and Lateral Waves in Acoustic Scattering by Large Elastic Cylinders," J. Acoust. Soc. Am., **59**, pp. 46-54, (1976).
38. A. J. Rudgers, "Acoustic Sound Pulses Scattered by a Rigid Sphere Immersed in a Fluid," J. Acoust. Soc. Am. **45**, pp. 900-910, (1968).

39. W. G. Neubauer and L. R. Dragonette, "Observation of Waves Radiated from Circular Cylinders Caused by an Incident Pulse," J. Acoust. Soc. Am. 48, pp. 1135-1149, (1970).
40. D. Brill and H. Uberall, "Acoustic Waves Transmitted through Solid Elastic Cylinders," J. Acoust. Soc. Am. 50, pp. 921-939, (1971).
41. C. W. Horton, W. R. King, and K. J. Diercks, "Theoretical Analysis of the Scattering of Short Acoustic Pulses by a Thin-Walled Metallic Cylinder in Water," J. Acoust. Soc. Am. 34, pp. 1929-1932, (1962).
42. G. Herrmann and I. Mirsky, "Three-Dimensional and Shell-Theory Analysis of Axially Symmetric Motions of Cylinders," J. Applied Mechanics, pp.563-568, (1956).
43. T. N. Grigsby and E. J. Tajchman, IRE Trans. UE-8, pp. 26-33 (1961).
44. R. K. Luneberg, Mathematical Theory of Optics, (Univ. of California Press, Berkley, 1966).
45. J. B. Keller, R. M. Lewis and B. D. Seckler, Commun. Pure Appl. Math. 9, pp. 207, (1956).
46. J. George and H. Uberall, "Approximate Methods to Describe the Reflection From Cylinders and Spheres With Complex Impedance," J. Acoust. Soc. Am. 65, pp. 15-24, (1979).
47. L. S. Schuetz and W. G. Neubauer, "Acoustic Reflection From Cylinders -- Nonabsorbing and Absorbing," J. Acoust. Soc. Am. 62, pp. 513-517, (1977).
48. C. Buddruss and P. Wille, "Experimental Studies Concerning the Scattering of Water-Borne Sound From Cylinders with Sound Absorbing Coatings," Acustica 18, pp. 159-168, (1967).
49. M. M. Machevariani, V. V. Tyutekin, and A. P. Shkvarnikow, "Impedance Method of Calculating Scattering of Layered-Inhomogeneous Elastic Media," Soviet Phys. --- Acoust. 17, pp. 77-81, (1971).
50. K. A. Velizhanina, N. N. Voronina, and E. S. Kodyskaya, "Impedance Investigation of Sound-Absorbing Systems in Oblique Sound Incidence," Soviet Phys. --- Acoust. 17, pp. 193-197, (1971).

51. V. M. Merkulova, "Reflection of Sound Waves From the Boundary Between a Layer and a Solid Absorbing Medium," *Soviet Phys. — Acoust.* **15**, pp. 404-405, (1970).
52. R. K. Cook and P. Chrzanowski, "Absorption and Scattering by Sound Absorbent Cylinders," *J. Acoust. Soc. Am.* **17**, pp. 315-325, (1946).
53. D. H. Hageman and V. L. Glass, *J. Appl. Phys.* **44**, pp. 3907-3913, (1973).
54. M. Lax and H. Feshback, "Absorption and Scattering from Impedance Boundary Conditions on Spheres and Circular Cylinders," *J. Acoust. Soc. Am.* **20**, pp. 108-124, (1948).
55. F. Mechel and P. Wille, "Ein Ähnlichkeitsgesetz Bei Der Streuung Ebener Wellen an Zylindern Komplexer Wandimpedanz," *Acoustica* **16**, pp. 101, (1965).
56. D. L. Brumgart, "Acoustic Scattering from a Sphere with Non-uniform Surface Impedance," Technical Report No. AD-783 805, NTIS, U. S. Dept. of Commerce (1974).
57. G. C. Gaunaurd, "Sonar Cross Section of a Hollow Cylinder in Water," *J. Acoust. Soc. Am.* **61**, pp. 360-368, (1977).
58. L. Flax and W. G. Neubauer, "Acoustic Reflection from Layered Elastic Absorptive Cylinders," *J. Acoust. Soc. Am.* **61**, pp. 307-312, (1977).
59. G. C. Gaunaurd, "High-Frequency Acoustic Scattering from Submerged Cylindrical Shells Coated with Viscoelastic Absorbing Layers," *J. Acoust. Soc. Am.* **62**, pp. 503-512, (1977).
60. G. Chertock, "General Reciprocity Relation," *J. Acoust. Soc. Am.* **34**, 989(A) (1962).
61. P. M. Morse and H. Feshback, Methods of Theoretical Physics (McGraw-Hill Book Co., New York, 1953), Parts I and II.
62. O. D. Kellogg, Foundations of Potential Theory (Dover Publications, Inc., New York, 1953).
63. Chen and Scheikert, "Sound Radiation From an Arbitrary Body," *J. Acoust. Soc. Am.* (1963), **35**(10), pp. 1626-1632.

64. M. L. Baron, H. H. Bleich and A. T. Matthews, "Forced Vibrations of an Elastic Circular Cylindrical Body of Finite Length Submerged in an Acoustic Fluid," *International Journal of Solids and Structures*, Vol.I, Jan. 1965. pp. 3-22.
65. B. B. Baker and E. T. Copson, The Mathematical Theory of Huygens' Principle (Oxford U. P., London, 1950).
66. G. Chertock, "Sound Radiation from Vibrating Surfaces," *J. Acoust. Soc. Am.* (1964), **36**(7), pp. 1305-1313.
67. P. M. Morse, Sound and Vibration (McGraw-Hill Book Co. Inc., New York, 1948), p. 320.
68. V. D. Kupradze, "Fundamental Problems in the Mathematical Theory of Diffraction," translated by C. D. Benster (NBS Rept. No. 2008, Oct. 1952).
69. R. P. Banaugh and W. Goldsmith, "Diffraction of Steady Acoustic Waves by Surfaces of Arbitrary Shape," *J. Acoust. Soc. Am.* (1963), **35**, pp. 1590-1601.
70. L. G. Copley, "Integral Equation Method for Radiation from Vibrating Bodies," *J. Acoust. Soc. Am.* (1966), **41**(4), pp. 807-816.
71. H. A. Schenck, "Improved Integral Formulation for Acoustic Radiation Problems," *J. Acoust. Soc. Am.* (1967), **44**(1), pp.41-58.
72. W. L. Meyer, W. A. Bell, B. T. Zinn, and M. P. Stallybrass, "Boundary Integral Solutions of the Three Dimensional Acoustic Radiation Problem," *J. of Sound and Vibration* (1978), **59**(2), pp.245-262.
73. P. H. Rogers, "Formal solution of the surface Helmholtz integral equation at a nondegenerate characteristic frequency," *J. Acoust. Soc. Am.* **54**, pp. 1662-1666, (1973).
74. G. Benthien and D. Barach, "CHIEF\* Users Manual," Naval Oceans Systems Center technical Report 970.
75. R. P. Shaw, "Boundary Integral Equation Method Applied to Wave Problems," in Developments in Boundary Element Method I, edited by P. K. Banerjee and R. Butterfield (Appl. Sci., London, 1979), Chap. 6.

76. F. Ursell, Proceedings of the Cambridge Philosophical Society, **74**, pp. 117-125.  
On the exterior Problems of acoustics.
77. A. J. Burton 1973 NPL Report NAC 30, National Physcial Laboratory, Teddington, Middlesex. The solution of Helmholtz's equation in exterior domains using integral equations.
78. A. J. Burton and G. F. Miller, Proceedings of the Royal Society of London Ser. A **323**, 201 (1971).
79. T. Terai, J. Sound and Vibration **69**, pp. 71-100, (1980).
80. Z. Ruet, Shiva Mathematics Series 4, pp.105-112, (1982).
81. W. Tobocman, J. Acoust. Soc. Am. **80**, 1828 (1986).
82. P. H. Rogers, "SHIP-A Fast Computer Program for Calculating the Acoustic Radiation and Radiation Impedance for Free-Flooded-Ring and Finite-Circular-Cylinder Sources," NRL Report 7240, June 1972.
83. Ian C. Mathews, "Numerical Techniques for the Three-Dimensional Steady-State Fluid-Structure Interaction," J. Acoust. Soc. Am. **79**, 1317-1325 (1986).
84. G. T. Schuster and L. C. Smith, "A Comparison Among Four Direct Boundary Integral Methods," J. Acoust. Soc. Am. **77**, 850-864 (1985).
85. A. F. Seybert, B. Soenark, F. J. Rizzo, and D. J. Shippy, "An Advanced Computational Method for Radiation and Scattering of Acoustic Waves in Three Dimensions," J. Acoust. Soc. Am. **77**, 362-368 (1985).
86. P. C. Waterman, "New Formulation of Acoustic Scattering," J. Acoust. Soc. Am. **45**, 1417-1429 (1969).
87. W. Tobocman, "Comparison of the T-Matrix Method and the Helmholtz Integral Equation Method for Wave Scattering Calculations," J. Acoust. Soc. Am. **77**, 369-374 (1985).
88. S. K. Numrich, V. V. Varadan, and V. J. Varadan, "Scattering of Acoustic Waves by a Finite Elastic Cylinder," J. Acoust. Soc. Am. **70**, pp. 1407-1411, (1981).

89. V. K. Varadan and V. V. Varadan editors, Acoustic, Electromagnetic and Elastic Wave Scattering -- Focus on the T-Matrix Method (Pergamon, New York, 1979).
90. X. -F. Wu, A. D. Pierce, and J. H. Ginsberg, "Variational Method for Computing Surface Acoustic Pressure on Vibrating Bodies, Applied to Transversely Oscillating Disks," IEEE J. Oceanic Engr., Vol. OE-12, No.2, Apr. 1987.
91. A. D. Pierce, "Stationary Variational Expressions for Radiated and Scattered Acoustic Power and Related Quantities," IEEE J. Oceanic Engr., Vol. OE-12, No. 2, Apr. 1987.
92. R. N. Capps, "Influence of Carbon Black Fillers on Acoustic Properties of Polychloroprene (Neoprene) Elastomers," J. Acoust. Soc. Am. 78, pp. 406-413, (1985).
93. W. Lethersich, Brit. J. Appl. Phys., 1, p. 294, (1950).
94. H. Kolsky, Stress Waves in Solids, (Dover, New York, 1963).
95. B. E. Read and G. D. Dean, The Determination of Dynamic Properties of Polymers and Composites (Wiley, New York, 1978).
96. J. M. Ide, "Some Dynamic Methods of Determination of Young's Modulus," Review of Scientific Instruments, Vol. 6, No. 10, pp. 296-298 (1935).
97. S. Spinner and W. E. Tefft, "A Method for Determining Mechanical Resonance Frequencies and for Calculating Elastic Moduli from These Frequencies," Proceeding of the Sixty-fourth Annual Meeting, Am. Soc. Testing Mats. (1961).
98. W. E. Teft and S. Spinner, "Torsional Resonance Vibrations of Uniform Bars of Square Cross Section," J. Research NBS, 65A, pp. 167-171 (1961).
99. S. L. Quimby, "On the Experimental Determination of the Viscosity of Vibrating Solids," Phys. Rev. 25, pp. 558-573 (1925).
100. J. W. Ballou and S. Silverman, "Young's Modulus of Elasticity of Films and Fibers by Sound Velocity Measurements," J. Acoust. Soc. Am. 16, pp. 113-119 (1944).

101. D. M. Norris, Jr. and W. C. Young, "Longitudinal Vibration of Viscoelastic Bars with End Masses," Project No. 1V025001A130, Report to U. S. Army Cold Regions Research and Engineering Laboratory, Hanover, N.H. (1967).
102. D. M. Norris, Jr. and W. C. Young, "Complex-modulus Measurement by Longitudinal Vibration Testing," *Exp. Mech.* **10**, pp. 93-93 (1970).
103. W. M. Madigosky and G. F. Lee, "Improved Resonance Technique for Materials Characterization," *J. Acoust. Soc. Am.* **73**, pp. 1374-1377, (1983).
104. T. M. Lee, "Method of Determining Dynamic Properties of Viscoelastic Solids Employing Forced Vibrations," *J. App. Phys.* **34**, pp. 1524-1529, (1963).
105. R. N. Capps, "Dynamic Young's Moduli of Some Commercially Available Polyurethanes," *J. Acoust. Soc. Am.* **73**, pp. 2000-2005, (1983).
106. Personally communication with W. M. Madigosky, Naval Surface Weapons Center, December 1986.
107. Personal communication with R. N. Capps, Underwater Sound Reference Detachment, Naval Research Laboratory, December 1986.
108. W. S. Cramer, "Propagation of Stress Waves in Rubber Rods," *J. Polym. Sci.*, **XXVI**, pp. 57-65, (1957).
109. A. W. Nolle, *J. Appl. Phys.*, **19**, p. 940 (1948).
110. J. D. Ferry, Viscoelastic Properties of Polymers (Wiley, New York, 1970), 2nd ed., Chap. 11.
111. G. R. Barnard, J. L. Bardin and J. W. Whiteley, "Acoustic Reflection and Transmission Characteristics for Thin Plates," *J. Acoust. Soc. Am.* **57**, pp. 577-584, (1975).
112. L. M. Brekhovskikh, Waves in Layered Media, (Academic, New York, 1960).
113. D. L. Folds and C. D. Loggins, "Transmission and Reflection of Ultrasonic Waves in a Layered Media," *J. Acoust. Soc. Am.* **62**, pp. 1102-1109, (1977).

114. M. J. Gregory, "Measurement of Rubber Properties for Design," *Polymer Testing* **4**, pp. 211-223, (1984).
115. M O'Donnell, E. T. Jaynes, and J. G. Miller, "Kramers-Kronig relationship between ultrasonic attenuation and phase velocity," *J. Acoust. Soc. Am.* (1981), **69**(3), pp. 696-701.
116. L. E. Horsely and C. M. Thompson, "The Aging of Cork-Rubber Decoupling Materials," Naval Research Laboratory Report No. 8458, (1981).
117. G. Arfken, Mathematical Methods for Physicists, (Academic Press, Orlando, 1985).
118. I. A. Stegun and M. Abramowitz, "Generation of Bessel Functions on High Speed Computers", Mathematical Tables and Other Aids to Computations, Vol. II pp. 255-257, 1957.
119. A. J. M. Hitchcock, "Polynomial Approximations to Bessel Functions of Order Zero and One and to Related Functions", Mathematical Tables and Other Aids to Computations, Vol. II pp. 86-88, 1957.
120. Robert J. Urick, Principles of Under Water Sound, (McGraw-Hill, New York, 1983).
121. A. E. Armenakias, D. C. Gazis, G. Herrmann, Free Vibration of circular Cylindrical Shells, (Pergamon Press, Oxford, 1969).
122. K. F. Graff, Wave Motion in Elastic Solids, (Ohio State University Press, Columbus, 1975).
123. T. R. Meeker and A. H. Meitzler, "Guided Wave Propagation in Elongated Cylinders and Plates", in Physical Acoustics, ed. by W. P. Mason, (Academic Press, New York, 1964).
124. IMSL, Inc., copyright 1982, Houston, Tx.



## VITA

Gary William Caille was born on November 7, 1955 in Passaic, New Jersey. He spent most of his formative years in Lake Hopatcong, New Jersey. In 1973, he graduated from Montclair Academy. The following fall he attended Lafayette College. After two years, he transferred to Cornell University and was awarded a Navy ROTC Scholarship. In June 1977, he obtained a Bachelor of Science Degree in Mechanical Engineering and was commissioned an Ensign in the United States Navy.

Following training at the Navy Nuclear Power School in Orlando, Florida, Navy Prototype Training Unit in Windsor Locks, Connecticut, and Navy Submarine School in Groton, Connecticut, he reported for duty aboard the USS Sturgeon (SSN 637) in November 1978. While onboard the USS Sturgeon, he served as Reactor Controls Officer, Sonar Officer and Weapons Department Head. After qualification in Submarines and as Engineer Officer, he reported to the Navy Nuclear Power School in August 1982. There, he served as the Division Director for the Officer Chemistry, Materials and Radiological Fundamentals Division. Upon completion of his tour of duty in September 1984, he commenced doctoral studies at the Georgia Institute of Technology.

He has a Master of Science Degree from the University of Central Florida and is a registered Professional Engineer in the states of Florida and New Jersey. In January 1987, he was promoted to the rank of Lieutenant Commander.

He is married to the former Susan Cox of Orlando, Florida and they have two children, Stephanie and Kevin.